Analysis of Krypton Conversion Electron Lines of the Gaseous Krypton-Tritium Source of KATRIN

Master Thesis

Submitted by

Matthias Böttcher

December 2020

First examiner: *Prof. Dr. Christian Weinheimer*

Second examiner: *Prof. Dr. Anton Andronic*

Westfälische Wilhelms-Universität Münster
Fachbereich Physik
Institut für Kernphysik

Contents

1 Introduction

Neutrinos are among the most abundant known elementary particles in nature. They played an important role in the formation of the Universe, and their properties point to physics beyond the Standard Model of elementary particles. Neutrinos are thus a very important area of research in particle physics. While the discovery of neutrinos lies more than sixty years in the past, the neutrino mass still remains unknown, since it is more than five orders of magnitude smaller than the electron mass. The Karlsruher Tritium Neutrino Experiment (KATRIN) has the aim to measure the mass of the electron neutrino with a sensitivity of $0.2\,\mathrm{eV/c^2}$, exceeding the previous Mainz [Kra+05] and Troitsk [Kra+12] experiments by a factor of 10. In 2019, KATRIN published a first improved upper limit of $m_{\bar{\nu}_e} < 1.1\,\mathrm{eV/c^2}$ (90 % C.L.) [Ake+19]. The experiment measures the energy spectrum of tritium β^- decay electrons. The shape of the β spectrum is influenced by the mass of the electron antineutrino, and can be used to access the neutrino mass in a model-independent kinematic approach. KATRIN uses the MAC-E filter principle to measure the electron energy spectrum in an integrating way. Hereby, an electron has to pass a retarding voltage to be counted in a detector. The retarding voltage is defined as the difference of the spectrometer potential and the tritium source potential, which both have to be known to high precision. To investigate the potential distribution, $^{83\mathrm{m}}$Kr can be injected into the source. This metastable krypton isotope is a nuclear standard featuring sharp and well-known conversion electron lines. A shift or broadening of these lines indicates a systematic effect that would also influence the β spectrum used for neutrino mass measurements. An important systematic is the potential distribution of a low density plasma in the tritium source.

In this thesis, measurement data of $^{83\mathrm{m}}$Kr are analysed, which were recorded in 2020 during the third neutrino mass measurement campaign (KNM3). The analysis focuses on two Kr conversion electron lines, the $\mathrm{L_3}$ line and the $\mathrm{N_{23}}$ doublet. The $\mathrm{L_3}$ features a high intensity and is well suited to investigate energy shifts. Yet, its comparatively large natural line width reduces the sensitivity on broadenings and requires detailed understanding of systematic effects, such as the energy dependent background. The $\mathrm{N_{23}}$ doublet has much lower intensity, while its vanishing natural width allows for high precision broadening investigations. Results and conlusions from the analysis presented in this thesis motivated more dedicated investigations of the $\mathrm{N_{23}}$ lines and were used as input for the KNM2

neutrino mass analysis.
The thesis outline is as follows. Section 2 gives an overview of neutrino physics, describing the history of the neutrino discovery, neutrinos in the Standard Model of particle physics, neutrino oscillations, mass mechanisms, and experimental search for the neutrino mass. In section 3, the experimental setup of KATRIN is described, along with the application and properties of ^{83m}Kr conversion electrons. Section 4 presents the analysis performed for this thesis. First, a description of the fit model used in the analysis is given. Then the various studies of the L_3 and N_{23} lines are presented.

2 Neutrino Physics

In this chapter, a summary of the basic properties, theoretical concepts and experimental research of neutrinos is given. Section 2.1 contains a brief recapitulation of the history of the discovery of the neutrino. In section 2.2 a summary of the Standard Model of particle physics is given, with a focus on weak interactions and the role of neutrinos. In section 2.3 the phenomenon of neutrino oscillation is elucidated, which established that neutrinos have mass. Section 2.4 briefly presents neutrino mass mechanisms. Section 2.5 gives an overview of the current observational constraints on the neutrino mass, with an emphasis on direct kinematic measurement of β decays, as applied in KATRIN.

2.1 Discovery of the Neutrino

In the year 1914, James Chadwick showed that the energy spectrum of electrons emitted in β decays is continuous, which is in contrast to α and γ decays [Cha14]. Assuming the β decay to be a two-body process involving the emission of electrons and nuclear recoil, a continuous spectrum would require a violation of energy conservation. In the 1930s, Wolfgang Pauli proposed the existence of a new particle to explain the continuous β spectrum. This electrically neutral and extremely light particle, later called "neutrino", should be emitted along the electron during β decay, producing the continuous spectrum [Pau30]. Shortly afterwards, Enrico Fermi formulated his theory of β decay, which explained the creation of electron and neutrino as quantum processes [Fer34].

However, being very weakly interacting, it was only later in the 1950s when the neutrino was finally detected directly in the Cowan-Reines experiment. It used the inverse β decay,

$$\bar{\nu}_\mathrm{e} + \mathrm{p} \longrightarrow \mathrm{e}^+ + \mathrm{n}, \tag{2.1}$$

to detect neutrinos produced in nuclear reactors [Cow+56]. These neutrinos are called electron (anti-)neutrinos, since they appear in reactions alongside electrons.

Later on, two additional flavours of neutrinos were discovered, the muon neutrino ν_μ and tau neutrino ν_τ, corresponding to the respective charged leptons. Using the decay width of the Z^0 boson, it was shown at the electron-positron collider LEP that there are three neutrino flavours which interact with Z^0 and have mass $m_\nu < m_\mathrm{Z}/2 \approx 45\,\mathrm{GeV}$ [Dec+90]. Today, ν_e, ν_μ, and ν_τ are part of the Standard Model of particle physics, as described in the following section.

2.2 Neutrinos in the Standard Model

The Standard Model of particle physics (cf. fig. 2.1) describes the elementary constituents of matter and its fundamental interactions within the framework of quantum field theory, in which particles appear as quantised excitations of fields.

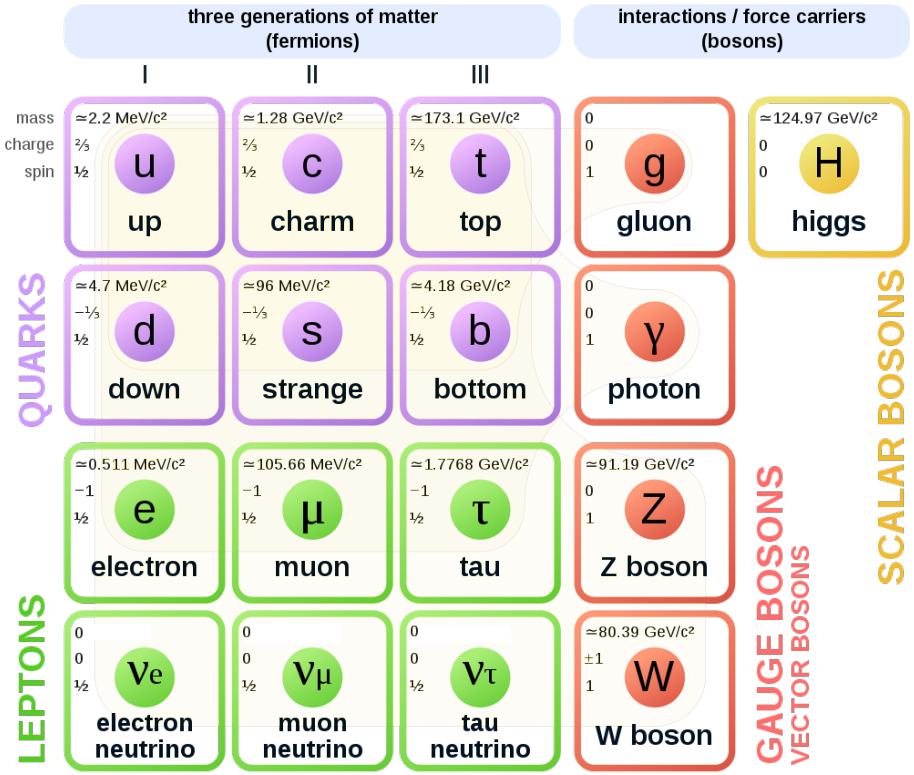

Figure 2.1: The Standard Model of particle physics contains the known elementary particles and fundamental interactions in nature. This figure shows the masses, electric charges and spins of the particles. In case of the neutrinos, the masses were assumed zero, but are today known to be finite and being probed by the KATRIN experiment. Figure adapted from [Mis20].

The Standard Model contains two different types of particles: Fermions, which have a spin of half of an uneven number, make up the matter, while bosons with integer spin mediate the fundamental forces of nature. Within the fermions, there are three generations of similar particles. The first generation contains the particles that constitute the matter which the atomic world is made of: Up and down quarks, and the leptons electron and electron neutrino. The other

two generations resemble the first one, but with overall higher masses, while the masses of the neutrinos are yet unknown. For every charged particle there is a corresponding antiparticle with opposite charge. Whether neutrinos are their own antiparticles (called Majorana fermions as opposed to Dirac fermions), is also not known.

There are four kinds of bosons. The photon γ carries the electromagnetic force, $\mathrm{W}^{\pm}$ and Z^0 bosons mediate the weak force and gluons g the strong interaction. The Higgs field H produces the masses of the elementary particles as described by the Higgs mechanism. Neutrinos however were thought to be massless for a long time. The observation of neutrino oscillation changed this view, as explained in section 2.3.

Within the theory of Glashow, Weinberg, and Salam [GG61; Wei67; SW64], the electroweak interaction is governed by a SU(2)×U(1) gauge symmetry of weak isospin I and weak hypercharge $Y = 2(\frac{Q}{e} - I_3)$, where Q is the electric charge, e the elementary charge, and I_3 the third component of the weak isospin vector. The observed particles γ, Z^0 and $\mathrm{W}^{\pm}$ appear as superpositions of the gauge bosons B and $\mathrm{W}_{1,2,3}$,

$$\begin{pmatrix} \gamma \\ \mathrm{Z}^0 \end{pmatrix} = \begin{pmatrix} \cos\theta_W & \sin\theta_W \\ -\sin\theta_W & \cos\theta_W \end{pmatrix} \begin{pmatrix} \mathrm{B} \\ \mathrm{W}_3 \end{pmatrix}, \tag{2.2}$$

$$\mathrm{W}^{\pm} = \frac{1}{\sqrt{2}}(\mathrm{W}_1 \mp i\mathrm{W}_2), \tag{2.3}$$

with the Weinberg angle θ_W. The charged and neutral leptons with left-handed chirality form weak isospin doublets $(\nu_\mathrm{e}, \mathrm{e}^-)$, (ν_μ, μ^-), (ν_τ, τ^-). The $\mathrm{W}^{\pm}$ couple to I and act as ladder operators in weak isospin space, mediating transitions between quarks, as well as between charged leptons and neutrinos. In this picture, the β^- decay

$$\mathrm{n} \longrightarrow \mathrm{p} + \mathrm{e}^- + \bar{\nu}_\mathrm{e} \tag{2.4}$$

is described by exchange of a W^- boson. See section 2.5.1 for further discussion of the β decay.

The hypercharge photon B couples to Y, while its γ component couples only to Q, and the Z^0 to both Q and I_3. Since neutrinos carry no electric nor color charge, they couple to neither photons nor gluons, making them only interacting via the weak force. Thus, neutrinos have very small cross sections for interaction with matter. Furthermore, only left-handed particles and right-handed antiparticles

carry weak isospin and will interact in weak charged current. This effect of parity violation has been established by the Wu and Goldhaber experiments [Wu+57; GGS58]. The neutral weak current does also not affect right-handed particles or left-handed antiparticles, if they are electrically neutral, making neutrinos with such chirality sterile to Standard Model interactions. If neutrinos are their own antiparticles, the Majorana neutrino field would then be a sum of left- and right-handed components. The possible Majorana nature of neutrinos is being investigated by searching for neutrinoless double beta decay.

2.3 Neutrino Oscillations

Within the Standard Model, neutrinos are massless particles. The observation of neutrino oscillations changed this view and points to beyond Standard Model (BSM) physics.

2.3.1 Experimental Evidence

In 1970 the Homestake experiment used the reaction

$$\nu_{\mathrm{e}} + {}^{37}\mathrm{Cl} \longrightarrow \mathrm{e}^{-} + {}^{37}\mathrm{Ar} \tag{2.5}$$

to measure the neutrino flux originating from nuclear processes inside the Sun. The amount of produced ^{37}Ar showed that the solar neutrino flux was only one third of the expectation value from the standard solar model [Cle+98]. This discrepancy is called the solar neutrino problem.

Later, the Kamiokande experiment confirmed the solar neutrino deficit by detecting Cherenkov light from elastic neutrino – electron scattering in water [Hir+91]. Additional confirmation came from the radiochemical experiments GALLEX, SAGE and GNO [Ham+99; Abd+02; Alt+05].

In 1958, even before evidence for the solar neutrino deficit was found, Pontecorvo proposed oscillations of neutrino flavours, similar to oscillations observed in neutral kaons. Therefore, possibly only a fraction of the electron neutrinos produced in the Sun would reach Earth as electron neutrinos, while the remainder oscillated to the ν_μ and ν_τ states, to which the aforementioned experiments were not sensitive. This process violates lepton family number conservation, while the total lepton number is conserved [Pon68].

The first experiment to find conclusive evidence for neutrino oscillations was Super-Kamiokande, which used muon neutrinos produced in the atmosphere. The amount of detected muon neutrinos was found to depend on their path length to the detector, suggesting oscillation into different flavours [Fuk+98].

In 2001, the Sudbury Neutrino Observatory (SNO) showed that neutrino oscillations are indeed the solution to the solar neutrino problem. SNO was sensitive to both the charged and neutral current reactions of solar neutrinos with deuterium. In the former, only electron neutrinos take part, while in the latter all neutrino flavours do. The detection of Cherenkov light in heavy water showed that the total neutrino flux agrees with the standard solar model, while the electron neutrino flux amounts to only one third [Ahm+02].

2.3.2 Theoretical Description

Neutrino oscillations can be understood when considering that the flavour states $|\nu_\alpha\rangle$ ($\alpha = \nu, \mu, \tau$), which are eigenstates to the weak interaction, are superpositions of the mass states $|\nu_\mathrm{j}\rangle$ ($\mathrm{j} = 1, 2, 3$), which are eigenstates of the free Hamiltonian. Their relation is expressed by an unitary mixing matrix U, called PMNS matrix (named after Pontecorvo, Maki, Nakagawa and Sakata):

$$|\nu_\alpha\rangle = \sum_\mathrm{j} U^*_{\alpha\mathrm{j}} \, |\nu_\mathrm{j}\rangle \,, \quad |\nu_\mathrm{j}\rangle = \sum_\alpha U_{\mathrm{j}\alpha} \, |\nu_\alpha\rangle \,. \tag{2.6}$$

The evolution of an initial mass eigenstate $|\nu_\mathrm{j}(x, t = 0)\rangle$ according to the Schrödinger equation is given by

$$|\nu_\mathrm{j}(x, t)\rangle = e^{-iE\mathrm{j}t} \, |\nu_\mathrm{j}(x, 0)\rangle \,. \tag{2.7}$$

In relativistic approximation $p_\mathrm{j} \approx E_\mathrm{j} \approx E$ and natural units, the energy is given by

$$E_\mathrm{j} = \sqrt{p_\mathrm{j}^2 + m_\mathrm{j}^2} \approx E + \frac{m_\mathrm{j}^2}{2E}. \tag{2.8}$$

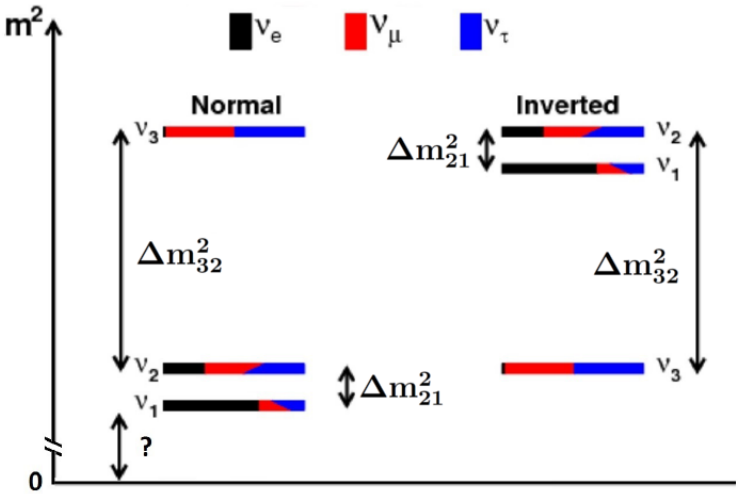

Figure 2.2: The spectrum of squared neutrino masses. Oscillation experiments only probe the splitting of squared masses, not the exact ordering or absolute mass scale. Two different orderings are possible, normal and inverted. The colors denote the flavour composition of the mass eigenstates. Figure adapted from [QV15] and [Kuc16].

It can then be shown that the probability of a neutrino, that was created as flavour α at $t = 0$, to be measured with flavour β at time $t = L$ is given by

$$P(\alpha \to \beta)(L) = \sum_{\mathrm{j}} |U_{\alpha\mathrm{j}} U^*_{\beta\mathrm{j}}|^2 + 2\mathrm{Re} \sum_{\mathrm{k<j}} U_{\alpha\mathrm{j}} U^*_{\alpha\mathrm{k}} U^*_{\beta\mathrm{j}} U_{\beta\mathrm{k}} \exp\left(-\frac{\Delta m^2_{\mathrm{jk}}}{2} \frac{L}{E}\right). \quad (2.9)$$

Therefore, the observation of neutrino oscillations shows that there must be a difference of squared mass states $\Delta m^2_{\mathrm{jk}} = m^2_{\mathrm{j}} - m^2_{\mathrm{k}}$, showing that at least two of the three masses are non-zero. Yet, it contains no information on the absolute mass scale, nor the exact ordering of the masses.

Observations allow for two possible orderings of the mass eigenstates, called normal (NO, $m_1 < m_2 < m_3$) and inverted (IO, $m_3 < m_1 < m_2$) [Zub12]. This is displayed in fig. 2.2. A global analysis of neutrino oscillation experiments gives [Zyl+20]

$$\Delta m^2_{21} = 7.55^{+0.20}_{-0.16} \cdot 10^{-5}\ \mathrm{eV}^2/\mathrm{c}^4 \qquad \text{(NO, IO)}, \quad (2.10)$$

$$\Delta m^2_{32} = (2.424 \pm 0.03) \cdot 10^{-3}\ \mathrm{eV}^2/\mathrm{c}^4 \qquad \text{(NO)}, \quad (2.11)$$

$$\Delta m^2_{32} = -2.50^{+0.04}_{-0.03} \cdot 10^{-3}\ \mathrm{eV}^2/\mathrm{c}^4 \qquad \text{(IO)}. \quad (2.12)$$

It is noteworthy that when neutrinos pass matter, their oscillation behaviour is changed. This phenomenon is called MSW effect (named after Mikheyev, Smirnov, and Wolfenstein) [MS86; Wol78]. The reason lies in charged current interactions of the electron neutrino state with electrons in matter (coherent forward scattering). In the next section, a brief overview of neutrino mass mechanisms is given.

2.4 Neutrino Mass Mechanisms

As stated in the previous section, neutrino oscillations give only information on the splitting of squared mass eigenstates. The absolute scale or ordering of the masses remains unknown.
There are two classes of scenarios. The masses could be hierarchical,

$$m_i \ll m_j \ll m_k, \tag{2.13}$$

and thus resemble the pattern of the generations of particles in the SM. On the other hand, the mass differences could be small compared to the absolute mass scale, which gives a degenerate pattern

$$m_1 \approx m_2 \approx m_3. \tag{2.14}$$

In order to distinguish between hierarchical and degenerate scenarios, knowledge of the absolute mass scale in the sub-eV regime is required [KATa].

Within the Standard Model, introducing mass terms to the Lagrangian would break gauge symmetry. Instead, the masses of the elementary particles are generated by the Higgs mechanism using the concept of spontaneous symmetry breaking. The coupling with the Higgs field ϕ in effect gives mass to particles. For lepton fields, this coupling is expressed by Yukawa terms of the form

$$\mathcal{L}_{\text{Yuk}} = -c_{\text{e}} \left(\bar{\text{e}}_{\text{R}} \phi^{\dagger} \begin{pmatrix} \nu_{\text{e}} \\ \text{e} \end{pmatrix}_{\text{L}} + (\bar{\nu}_{\text{e}}, \bar{\text{e}})_{\text{L}} \phi \text{e}_{\text{R}} \right), \tag{2.15}$$

where c_{e} is the Yukawa coupling constant, and L, R denote left-handed doublets and right-handed singlets of weak isospin, respectively.

Using the vacuum Higgs field $\phi_0 = \begin{pmatrix} 0 \\ \frac{v}{\sqrt{2}} \end{pmatrix}$ with expectation value v, an electron mass term $-c_\mathrm{e}\frac{v}{\sqrt{2}}\bar{\mathrm{e}}\mathrm{e}$ with $\mathrm{e} = \mathrm{e_L} + \mathrm{e_R}$ is obtained. Generating neutrino mass terms using this procedure would require right-handed neutrino singlets, which are sterile and thus not part of the Standard Model. Moreover, to explain the low mass of neutrinos, the neutrino Yukawa coupling would need to be more than five orders of magnitude smaller than the electron's, which is considered unnatural by many [Hig64].
If the neutrino is of Majorana nature, $\nu = \nu_\mathrm{L} + \nu_\mathrm{R} = \nu_\mathrm{L} + \nu_\mathrm{L}^C = \nu^C$, where C denotes charge conjugation, additional mass terms can be constructed, expressed by a mass matrix M. Diagonalisation of M gives two eigenvalues

$$m_{1,2} = \frac{m_\mathrm{R}}{2} \pm \sqrt{\frac{m_\mathrm{R}^2}{4} + m_\mathrm{D}^2} \overset{m_\mathrm{R} \gg m_\mathrm{D}}{\approx} \begin{cases} m_\mathrm{R} \\ \frac{m_\mathrm{D}^2}{m_\mathrm{R}} = m_\nu, \end{cases} \tag{2.16}$$

where m_D is the Dirac mass and m_R the right-handed Majorana mass component.

The magnitude of m_ν is suppressed by a large m_R, which would explain the smallness of the observed neutrino masses. This so-called Seesaw type 1 mechanism prefers a hierarchical neutrino mass pattern. There are other models, such as Seesaw type 2, which predicts a Higgs triplet coupling directly to the light neutrinos, and suggests degenerate or quasi-degenerate neutrino mass scenarios. Therefore, investigation of the absolute neutrino mass scale allows to distinguish between these various mass mechanisms [KATa].

2.5 Observational Limits on the Neutrino Mass

Observational constraints on the neutrino mass come from various sources.

- **Cosmology:** Despite their low mass, neutrinos play a significant role in early structure formation, since second to photons they are the most abundand known particle in the cosmos. In the early Universe, structures smaller than the neutrinos' free-streaming length got washed out. The free-streaming length depends strongly on the neutrino mass. The observable of cosmological measurements is the sum of the mass eigenstates $\sum_\mathrm{i} m_\mathrm{i}$. The current upper limit depends on the assumed cosmological model and combination of datasets, and is in the most stringent case $\sum_\mathrm{i} m_\mathrm{i} < 0.11\,\mathrm{eV/c^2}$ [Zyl+20].

- **Neutrinoless double β decay:** Some nuclei can undergo two β decays at the same time. If neutrinos are Majorana particles, it is conceivable that the antineutrino produced in one decay can be absorbed as a neutrino in the other one, so that no neutrino appears in the final state. The absorption process couples only to the left-handed component of the (anti-)neutrino, which is called the wrong helicity and depends on the neutrino mass. Such $0\nu\beta\beta$ processes have not been observed yet. Under some model dependent assumptions, this constrains the effective Majorana mass, which is a coherent sum of the mass eigenstates of the electron neutrino, wheighted with the PMNS matrix elements, to $\langle m_{\beta\beta}\rangle = |\sum_i U_{\mathrm{ei}}^2 m_{\mathrm{i}}| < 61 - 165\ \mathrm{meV/c^2}$ [Gan+16; Ago+18; Ada+19; Ant+19].

- **Time of flight of supernova neutrinos:** In supernovae, a large amount of neutrinos of different flavours is produced. Due to kinematics, the time of flight difference of the flavours depends on their effective mass $m_{\nu_\alpha}^2 = \sum_{\mathrm{i}} |U_{\alpha\mathrm{i}}^2| m_{\mathrm{i}}^2$. Experimental limits depend strongly on the supernova model and are on the order of $m_{\nu_{\mathrm{e}}} < 5.7\,\mathrm{eV/c^2}$ [LL02].

Another class of experiments, such as KATRIN, measures the kinematics of β decays. In section 2.5.1, the underlying physics is discussed.

2.5.1 Kinematic Neutrino Mass Measurements Using β Decays

In β decays of nuclei, the atomic number Z changes by ± 1, while a proton becomes a neutron or vice versa. The mass number A remains constant. There are two kinds of β decays:

$$\beta^- : \mathrm{n} \longrightarrow \mathrm{p} + e^- + \bar{\nu}_{\mathrm{e}} \tag{2.17}$$

$$\beta^+ : \mathrm{p} \longrightarrow \mathrm{n} + e^+ + \nu_{\mathrm{e}}. \tag{2.18}$$

A related process is the electron capture, in which an electron from the atomic shell is absorbed by a proton:

$$\mathrm{e}^- + \mathrm{p} \longrightarrow \mathrm{n} + \nu_{\mathrm{e}}. \tag{2.19}$$

On quark level, these processes are mediated via exchange of a W boson, which transforms down into up quarks or vice versa. Figure 2.3 illustrates this process.

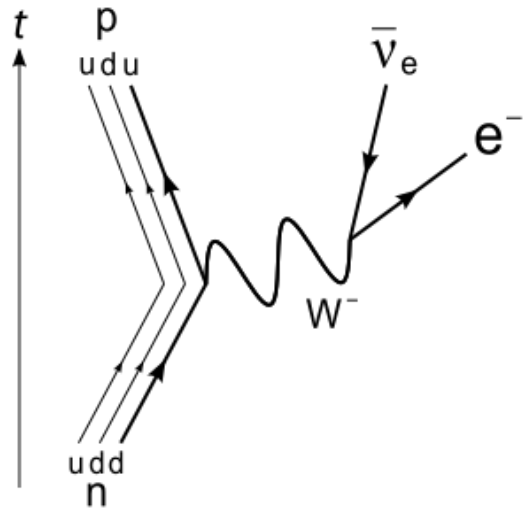

Figure 2.3: The leading-order Feynman diagram of the β^- decay. A down quark transites into an up quark via emission of a W^-, which then decays into an electron and electron antineutrino. Figure from [Hol17].

Since KATRIN uses the β^- decay of tritium, the further discussion will focus on β^-. Using Z and A, the reaction can be written as

$$(Z, A) \longrightarrow (Z + 1, A) + \mathrm{e} + \bar{\nu}_\mathrm{e} + Q. \tag{2.20}$$

Being a three-body process, energy, momentum and angular momentum conservation allows the decay energy Q to be shared continuously between daughter nucleus, electron, and antineutrino, while the daughter nucleus will only get little recoil energy due to its dominating mass.
Because of their tiny cross section for interaction with matter, direct measurement of the neutrino energy spectrum is unpracticable. However, the neutrino mass can be extracted from the electron energy distribution (β spectrum). Being a measurement that relies purely on kinematics, such an approach is called model independent.

The differential β spectrum can be derived using Fermi's golden rule and is given by [KATa; Dre+13]

$$\begin{aligned}\frac{\mathrm{d}^2N}{\mathrm{d}t\mathrm{d}E} =& \frac{G_\mathrm{F}^2\cos^2(\theta_C)}{2\pi^3}|M_\mathrm{if}|^2F(Z+1,E)p(E-m_\mathrm{e}) \\ &\cdot(E_0-E)\sqrt{(E_0-E)^2-m_{\bar{\nu}_\mathrm{e}}^2}\Theta(E_0-E-m_{\bar{\nu}_\mathrm{e}}),\end{aligned} \tag{2.21}$$

with

- G_F: Fermi constant
- θ_C: Cabibbo quark mixing angle
- M_if: Nuclear matrix element, describing the nuclear part of the transition from initial to final state
- F: Fermi function, accounting for the interaction of the electron with the daughter nucleus' Coulomb field
- Θ: Heaviside function, ensures energy conservation
- E_0: The endpoint energy of the spectrum, i.e. the total kinetic energy that is distributed to electron and neutrino. It is given by the decay energy Q minus nuclear recoil, electronic excitation in the final state, atomic and molecular binding energies.

The neutrino mass is entering as an incoherent sum of the mass eigenstates that constitute the electron antineutrino:

$$m_{\bar{\nu}_\mathrm{e}}^2 = \sum_\mathrm{i}|U_\mathrm{ei}^2|m_\mathrm{i}^2. \tag{2.22}$$

Actually, the electron energy distribution is a superposition of three spectra with different decay and thus endpoint energies, splitted by the differences of the mass eigenstates. This effect however is too small to be measured in an experiment like KATRIN, so that an effective mass like in eq. (2.22) is observed [FS03]. Throughout this thesis, this quantity is meant when referring to the neutrino mass measured by KATRIN.

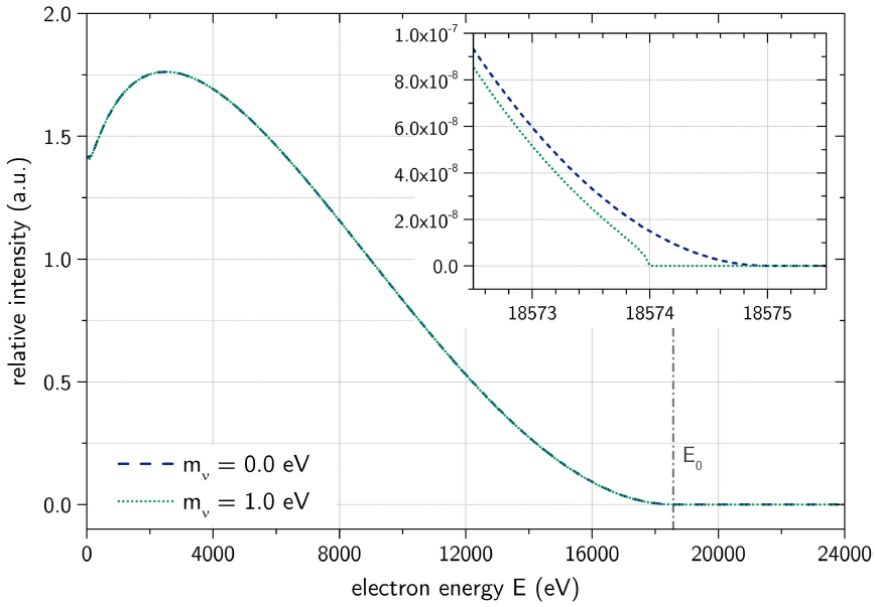

Figure 2.4: The differential β spectrum of tritium, for cases $m_{\bar{\nu}_e} = 0$ and $m_{\bar{\nu}_e} = 1\,\mathrm{eV}$. The impact of a non-vanishing neutrino mass is most pronounced near the endpoint $E_0 \lesssim 18\,575\,\mathrm{eV}$, where only a small fraction of decays contribute. Figure from [Kle14].

The neutrino mass enters eq. (2.21) in the term $\sqrt{(E_0 - E)^2 - m_{\bar{\nu}_e}}$. Therefore, its impact is strongest near the endpoint, as shown in fig. 2.4. Thus, it is preferred to use a β isotope whose endpoint is rather low, since there a larger fraction of electrons is close to the endpoint energy. Tritium ^{3}H used in the KATRIN experiment has a very low endpoint on the order of 18.6 keV. Additionally, it features a low half-live of 12.3 years and a simple electronic shell structure. Being a super-allowed decay, the nuclear matrix element is energy independent. Furthermore, the low electric charge of mother and daughter nucleus means only little interaction with the emitted electron, and reduces the inelastic scattering cross section of the electrons with the source material [Kuc16].

The current upper limit on the neutrino mass from direct kinematic measurements comes from KATRIN and is [Ake+19]

$$m_{\bar{\nu}_e} < 1.1\,\mathrm{eV/c^2} \quad (90\,\%\ \ \mathrm{C.L.}). \tag{2.23}$$

In the next chapter, the experimental setup of KATRIN is presented.

3 The KATRIN Experiment

The Karlsruher Tritium Neutrino experiment KATRIN is located at the Karlsruher Institut für Technologie (KIT). The nearby Tritiumlabor Karlsruhe (TLK) provides the experience and infrastructure to handle a sufficent amount of tritium for the experiment. The goal of KATRIN is to measure the effective mass of the electron antineutrino within three years of measurement time. The discovery potential is $5\,\sigma$ for $m_{\bar{\nu}_e} = 0.35\,\mathrm{eV/c^2}$. In case of a negative signal, KATRIN will set an upper limit of $m_{\bar{\nu}_e} < 0.2\,\mathrm{eV/c^2}$ (90 % C.L.). Hereby, it probes the cosmologically relevant mass range and quasi-degenerate scenarios [KATa].

KATRIN uses the MAC-E-filter principle to measure the integrated β spectrum of tritium in its endpoint region. Tritium decays into $^3\mathrm{He}^+$,

$$^3\mathrm{H} \longrightarrow {}^3\mathrm{He}^+ + e^- + \bar{\nu}_e. \tag{3.1}$$

The properties that make the β spectrum of tritium suitable for measuring the neutrino mass have already been discussed in section 2.5.1. The following section 3.1 describes the experimental setup of KATRIN. Section 3.2 elucidates the MAC-E filter principle.

3.1 Experimental Setup

KATRIN has a 70 m long beamline, which is devided into three main parts: The rear section, the source and transport section (STS), and the spectrometer and detector section (SDS), containing multiple subsystems, as illustrated in fig. 3.1.

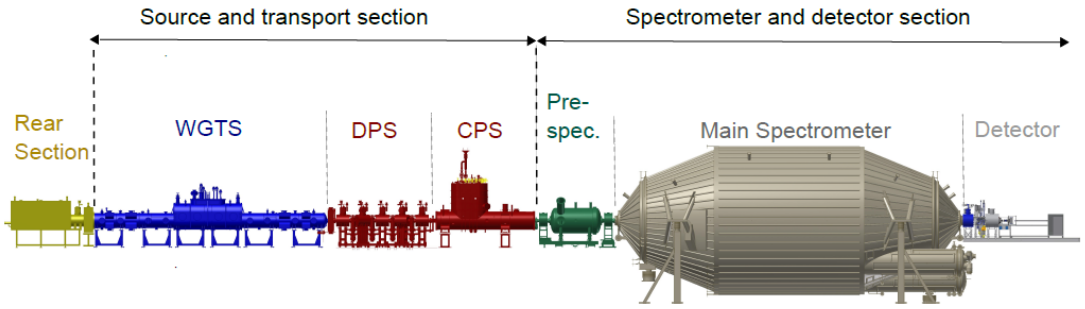

Figure 3.1: The KATRIN setup, containing the rear section, windowless gaseous tritium source (WGTS), differential pumping section (DPS), cryogenic pumping section (CPS), pre-spectrometer, main spectrometer, and focal plane detector. The monitor spectrometer is not shown, since it is separated from the beamline. Figure from [Kuc16].

3.1.1 Rear Section

The rear section is monitoring important parameters of the windowless gaseous tritium source (WGTS), such as source activity and column density (amount of gas per WGTS beam tube area). Various monitoring systems are in use. The source activity is measured with the forward beam monitor in forward direction and with beta-induced X-ray spectroscopy (BIXS) in backward direction. The column density, directly connected to the activity, can also be monitored by scattering of mono-energetic photoelectrons, emitted by the so-called e-gun. The rear section is separated from the WGTS via the gold-plated rear wall (RW), which can be put on electric potential.

3.1.2 Source and Transport Section

The STS contains the WGTS, and guides the β electrons to the SDS, while preventing tritium from reaching the spectrometers, which would increase the background rate.

The **windowless gaseous tritium source** contains a cylindrical tube of 10 m length and 90 mm diameter. It holds molecular tritium at a temperature of typically 30 K or more, depending on the type of measurement. The source activity is on the order of 10^{11} decay electrons per second, half of which are guided by magnetic fields towards the detector section. As shown in fig. 3.2, the tritium gets injected in the center and is removed at both ends by differential pumps DPS1-R and DPS1-F. On the left side, the WGTS is connected to the rear section by the rear wall. On the right side, the electrons are guided adiabatically by magnetic fields to the transport section. The nominal design column density is $\rho d_0 = 5 \cdot 10^{17}$ molecules per cm^2. It is a compromise between high activity and moderate amount of scattering at tritium. By scattering the β electrons lose energy and thus change the shape of the β spectrum. Further, they produce secondary electrons, generating a low density plasma of secondary electrons and ionised tritium molecules inside the WGTS. This plasma is topic of ongoing investigations. It has an electric potential distribution, presumably is influenced by factors like accumulation of space charges, the rear wall potential and work function, as well as the beam tube walls. The plasma potential directly influences the retarding voltage that a β electron has to overcome to reach the detector. Knowledge of these plasma related effects is therefore important to characterise systematic uncertainties in the integrated β spectrum. A further discussion is

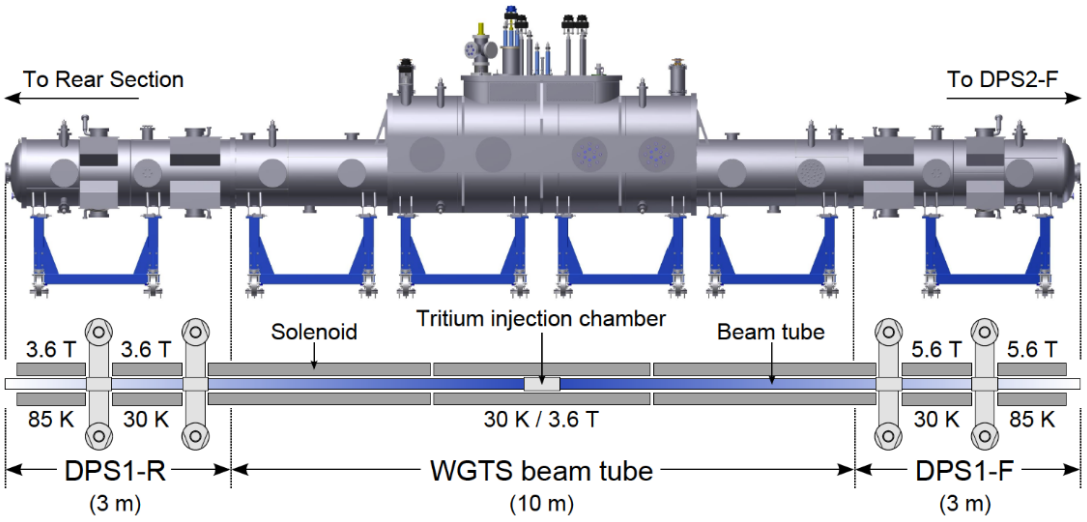

Figure 3.2: The windowless gaseous tritium source. Tritium is being injected in the center of the beam tube and removed by differential pumps on both ends. Magnetic fields guide the β electrons to the transport section (to the right). On the left side, the WGTS is separated from the rear section by the rear wall. Figure from [Har15].

given in section 3.3. It is possible to inject gaseous ^{83m}Kr into the WGTS, alongside as well as without tritium. This metastable krypton isotope produces sharp conversion electron lines which allow investigation of systematic energy shifts and broadenings, for instance related to plasma effects. In the krypton mode the temperature is increased to 80 K or more to prevent freezing of the krypton [Alt+20]. In section 3.4, a description of the ^{83m}Kr energy spectrum is given.

The windowless design of the tritium source avoids additional energy loss of β electrons while leaving the source. Thus, a reliable pumping system is needed to keep tritium from contaminating the SDS.

Within the **transport section** another array of differential pumps removes remaining gas that has not been pumped out yet. Moreover, there are chicanes in the beamline to prevent a direct line of sight between the WGTS and the spectrometer section. Neutral particles will hit the tilted walls and get pumped out, while the β electrons are guided by magnetic fields towards the SDS. Positive ions are filtered out by electric dipole electrodes.

Finally, the **cryogenic pumping section** (CPS), which also features tilted segments to prevent line of sight to the SDS, traps remaining tritium via cryo-

sorption processes on its 3 K gold-plated inner surface. After around 60 days, the surface is saturated with tritium. By increasing the temperature to 100 K, the tritium evaporates and gets pumped out. There is a condensed krypton source installed at the CPS, which can be used for calibration and characterisation of the SDS [Are+18; Ful]. Overall, the flow rate of tritium into the SDS is reduced by more than 14 orders of magnitude compared to the source [Res19; KATa; Ake+19].

3.1.3 Spectrometer and Detector Section

Within the spectrometer and detector section, three MAC-E filter type spectrometers are installed: The pre-, main and monitor spectrometer. The MAC-E filter principle is described in detail in section 3.2 on the expample of the main spectrometer.
The **pre-spectrometer** served as a prototype for the main spectrometer and is mainly used to filter out low-energetic electrons in order to decrease background.

The **main spectrometer** shown in fig. 3.3 is used for the actual measurement of the integrated energy spectrum of the electrons. It has a length of 23 m and a diameter of 10 m. The vessel is being operated in ultra-high vacuum conditions on the order of 10^{-11} mbar. A surrounding air coil system compensates the Earth's magnetic field and shapes the inner B field. It can also be used to reduce background of charged particles that are trapped in the electric and magnetic fields, employing a magnetic pulse method [Are+18]. The inner surface of the vessel is covered with a system of electrically isolated wire electrodes (IE), which fine-tune the shape of the retarding potential.

A source of background is the emission of electrons when cosmic muons hit the spectrometer walls. Most of these electrons are however confined to a region outside of the signal electron flux tube due to the magnetic field configuration (magnetic shielding). Additionally, the wire electrodes are on more negative potential than the vessel walls, in order to reflect these electrons.

Another background source is radioactive decay of isotopes like ^{220}Rn and ^{219}Rn, which are present in the materials of the vessel and pumps. A single decay can produce mupltiple secondary electrons by scattering on resiudal gas, thus increasing the background significantly.
The total background is on the order of 300 mcps [Ake+19].

Figure 3.3: The main spectrometer. The left image shows the vessel viewed along the beam axis from the perspective of the detector end. It is surrounded by the air coil system. The right image shows the inside of the vessel, with the wire electrodes covering the inner surface. Figure from [KATb].

The retarding voltage, defining the potential that electrons have to overcome to reach the detector, is demanded to have a very high stability of 3 ppm over a two month period, for values of up to −35 kV. For this task, two ultra precise high voltage dividers K35 and K65 are used, which measure the potential directly. In addition, the monitor spectrometer is used.

The **monitor spectrometer** is the former spectrometer of the Mainz neutrino mass experiment. It is not part of the KATRIN beamline but a standalone system. Yet, it is on the same electric potential as the main spectrometer, so that it can be used to monitor the stability of the high-voltage system via ^{83m}Kr conversion electron lines from an implanted Kr source.

At the end of the KATRIN beamline, the **focal plane detector** (FPD), as shown in fig. 3.4, detects the electrons that were guided towards it by the magnetic fields inside the main spectrometer. While the MAC-E filter principle would allow to use a simple counting of electrons to measure the integrated energy spectrum, the FPD provides energy resolution on the order of 1.4 keV, which allows for background reduction by region-of-interest cuts. It also has spatial information of the incident electrons. For this task, the FPD silicon PIN diode wafer, which has a diameter of 90 mm, is segmented into 148 pixels of equal area $A = 44\,\mathrm{mm}^2$. They are arranged in 12 rings consisting of 12 pixels, plus the bullseye containing four pixels. This allows to investigate spatial inhomogeneities across the flux tube. Additionally, the FPD has a time resolution on the 100 ns level. To improve the

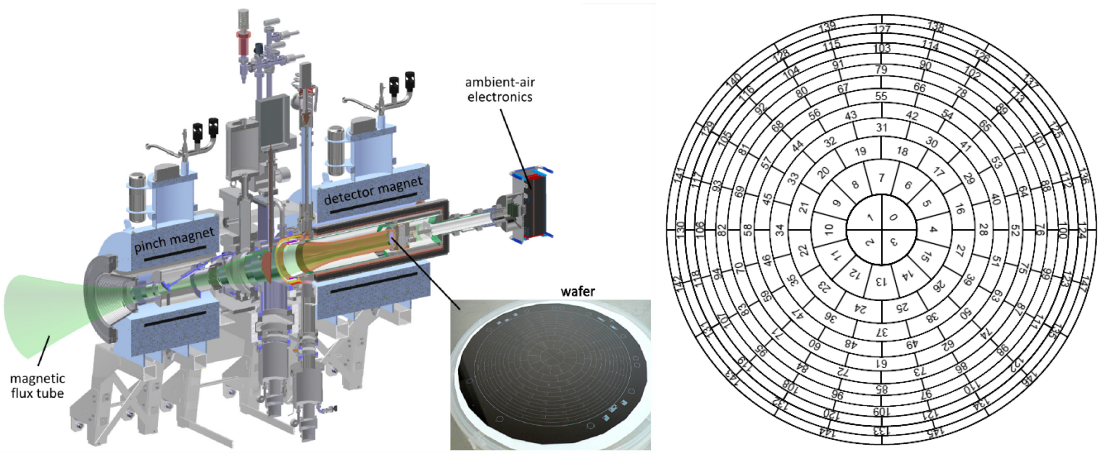

Figure 3.4: Left: The focal plane detector. Being installed at the end of the main spectrometer, the FPD measures the electrons that are mapped by the magnetic fields onto the detector wafer pixels, allowing for spatial resolution. The pinch magnet and detector magnet define the B fields in the FPD. Right: Scheme of the 148 FPD wafer pixels of equal area. Figures adapted from [Gro15].

signal-to-noise ratio, the electrons are accelerated by up to 10 keV via a post-acceleration electrode before reaching the detector wafer [Res19; Beh16; KATa].

3.2 MAC-E Filter Principle of the Main Spectrometer

The aspired sensitivity of KATRIN requires a spectrometer featuring high energy resolution on the order of $< 1\,\mathrm{eV}$, high luminosity, and low background. For this, a MAC-E filter is an ideal choice.

A MAC-E filter, which is an acronym for magnetic adiabatic collimation with electrostatic filtering, uses a combination of electric and magnetic fields to scan through the energy spectrum of, in this case, electrons. It is an integrating spectrometer: Electrons with kinetic energy E have to surpass a maximal retarding potential $qU < E$ in order to be counted in a detector. If they do not have enough energy they are reflected. Thus, the count rate at a given qU consists of all electrons with surplus energy $\mathcal{E} = E - qU > 0$. By varying the retarding potential, the energy spectrum is measured in an integrating way. In the KATRIN main spectrometer, sketched in fig. 3.5, the retarding potential is maximal in the so-called analysing plane in the middle.

The electrons entering the spectrometer have some angular distribution. Therefore, it would follow that not all electrons could use their full kinetic energy to surpass the retarding potential, but only the energy $E_\perp$ corresponding to the mo-

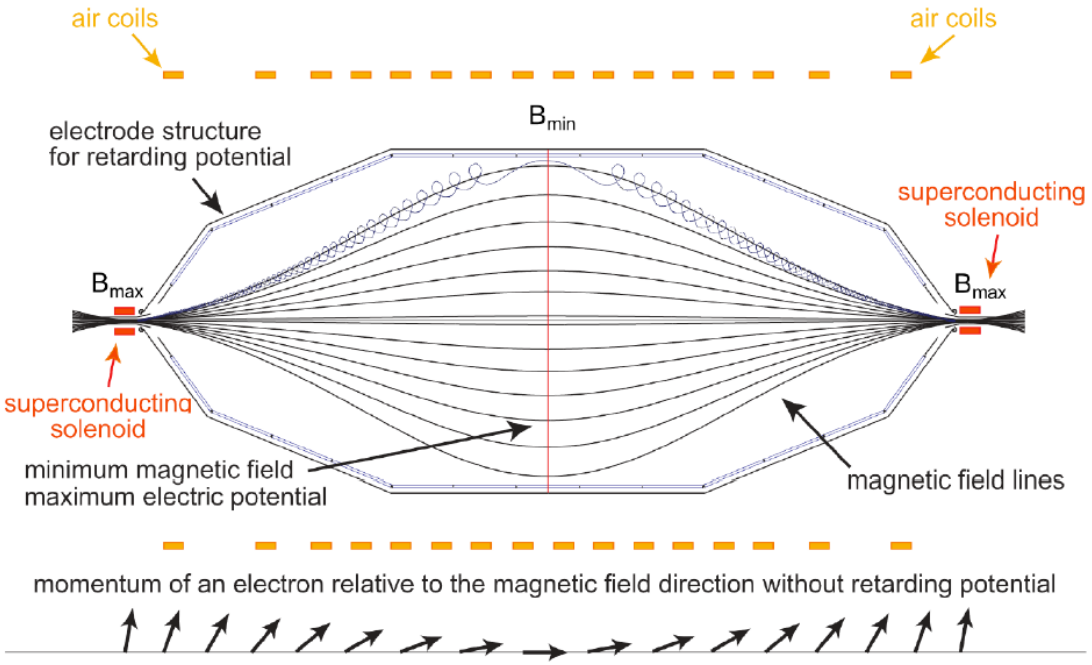

Figure 3.5: The MAC-E filter principle of the KATRIN main spectrometer. An electron, undergoing cyclotron motion around the magnetic field lines, has to overcome the maximum electric potential qU in the analysing plane (red vertical line). The B-field has local maxima at both ends of the spectrometer, and is mimimal in the analysing plane. The momentum vector follows the magnetic gradient, being collimated into longitudinal direction in the analysing plane, allowing the electron to use all its kinetic energy. The air coil system shapes the magnetic field. Figure adapted from [Bok14].

mentum component orthogonal to the analysing plane. For this reason, magnetic fields are used to collimate the electrons' momentum vector into the direction perpendicular to the analysing plane. On both ends of the spectrometer vessel, a strong magnetic field B is created by superconducting solenoids. The magnetic flux density decreases in longitudinal direction towards the center, being minimal in the analysing plane. Electrons are guided by the field lines on a cyclotron motion with gyro-radius

$$r = \frac{\sqrt{2m_e E_\perp}}{eB}. \tag{3.2}$$

The total kinetic energy of an electron following a magnetic field line can be split at any point into components corresponding to the momentum parallel and orthogonal to the field:

$$E = E_\parallel + E_\perp = E \cdot (\cos^2\theta + \sin^2\theta). \tag{3.3}$$

Here, the pitch angle θ is the angle between momentum vector and field line. The change in magnetic field over one cyclotron period should be small, in which case the motion of the electron is called adiabatic. From the adiabaticity follows that the magnetic moment

$$\mu = \frac{e}{2m_\mathrm{e}}|\vec{l}| = \frac{E_\perp}{B} \tag{3.4}$$

($\vec{l}$ being the angular momentum of the cyclotron motion) is constant along the electron's path [Jac99]. Therefore, as B decreases towards the analysing plane, $E_\perp$ has to decrease as well, so that the electron's momentum vector gets tilted parallel to the field line and the electron can use almost its entire energy to overcome the retarding potential. The ratio of the entrance and analysing plane magnetic fields defines the magnitude of the collimation:

$$\frac{E_\perp^\mathrm{source}}{B_\mathrm{source}} = \frac{E_\perp^\mathrm{ana}}{B_\mathrm{ana}} = \frac{E_\perp^\mathrm{pinch}}{B_\mathrm{pinch}}. \tag{3.5}$$

The nominal source magnetic field of the KATRIN main spectrometer is $B_\mathrm{source} = 3.6\,\mathrm{T}$. The analysing plane magnetic field B_ana is much smaller, on the order of 10^{-4} T, depending on the measurement. B reaches its global maximum at the pinch magnet on the end of the spectrometer (right side in fig. 3.5), with a design value $B_\mathrm{pinch} = 6\,\mathrm{T}$. In practice however, B_source and B_pinch are typically operated at 70 %, giving 2.52 T and 4.2 T, respectively.

The MAC-E filter is a high-pass filter, since electrons with sufficient starting energy E have a transmission probability $\mathcal{T} = 1$, while electrons with $E < qU$ have $\mathcal{T} = 0$. Since not the total starting energy E is collimated into longitudinal direction, some electrons with $E > qU$ will not be able to pass if their initial pitch angle θ_0 is too high. For an electron source with a single starting pitch angle, the transmission condition $\mathcal{T}(E, qU)$ is given by the step function

$$\mathcal{T}(E, qU, \theta) = \begin{cases} 1 & \text{if } \; E\left(1 - \sin^2\theta \frac{B_\mathrm{ana}}{B_\mathrm{source}} \frac{\gamma+1}{2}\right) > qU \\ 0 & \text{else.} \end{cases} \tag{3.6}$$

However, this simple shape is modified by the angular distribution of the electrons.

The maximum pitch angle for a given energy $E > qU$ is

$$\theta_0 \leq \theta_{\max} = \begin{cases} \arcsin \sqrt{\frac{E-qU}{E} \frac{B_{\text{source}}}{B_{\text{ana}}} \frac{2}{\gamma+1}} & \text{if } E < qU + \Delta E \\ \frac{\pi}{2} & \text{else.} \end{cases} \tag{3.7}$$

Here, γ is the Lorentz factor and $\Delta E = E \cdot \frac{B\text{ana}}{B\text{source}} \frac{\gamma+1}{2}$ is the energy resolution, which defines the width of the transmission function (eq. (3.8)). For the nominal KATRIN settings with $B_{\text{ana}} = 3\,\text{G} = 0.3\,\text{mT}$ and an electron energy close to the tritium endpoint 18.6 keV, this filter width is $\Delta E = 1.55\,\text{eV}$.

Assuming an isotropic distribution of starting angles, the transmission function T is given by the integration

$$T(E, qU) = \int_0^{\theta_{\max}} \mathrm{d}\theta \; \mathcal{T}(E, qU) \sin\theta \tag{3.8}$$

$$= \begin{cases} 0 & \text{if } E \leq qU \\ 1 - \sqrt{1 - \frac{E-qU}{E} \frac{B_{\text{source}}}{B_{\text{ana}}} \frac{2}{\gamma+1}} & \text{if } qU < E < qU + \Delta E \\ 1 & \text{else,} \end{cases} \tag{3.9}$$

using $\cos \arcsin x = \sqrt{1 - x^2}$.

In the main spectrometer however this function is modified by the magnetic mirror effect. Since the global maximum magnetic field B_{pinch} at the end of the spectrometer is larger than the source field, electrons with too high pitch angles are reflected magnetically. This cut-off limits the maximum pitch angle to $\theta_{\max} \mapsto \theta_{\max} = \arcsin \sqrt{\frac{B_{\text{source}}}{B_{\text{pinch}}}}$. Likewise, the transmission width is decreased to $\Delta E \mapsto \Delta E = E \cdot \frac{B\text{ana}}{B\text{pinch}} \frac{\gamma+1}{2}$. This modifies the transmission function to

$$T(E, qU) = \begin{cases} 0 & \text{if } E \leq qU \\ 1 - \sqrt{1 - \frac{E-qU}{E} \frac{B_{\text{source}}}{B_{\text{ana}}} \frac{2}{\gamma+1}} & \text{if } qU < E < qU + \Delta E \\ 1 - \sqrt{1 - \frac{B_{\text{source}}}{B_{\text{pinch}}}} & \text{else.} \end{cases} \tag{3.10}$$

The energy resolution is improved to $\Delta E = 0.93\,\text{eV}$. The acceptance angle is now reduced to 50.8° at nominal conditions, but since electrons with high pitch angles are more likely to have scattered in the source, the magnetic mirror effect reduces systematic uncertainties. The transmission function is plotted in fig. 3.6.

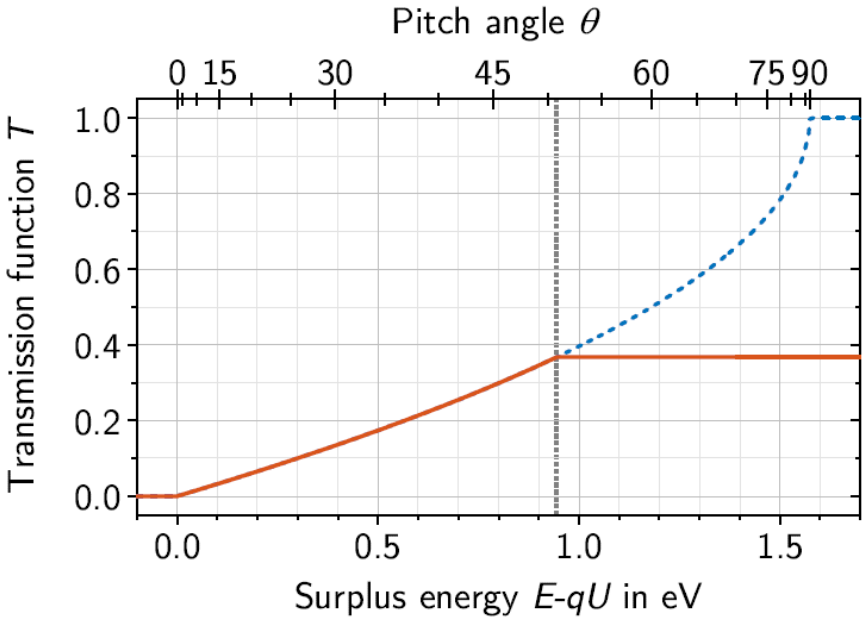

Figure 3.6: The transmission function of the main spectrometer in nominal conditions for electrons near the tritium endpoint energy. The upper abscicca shows the maximum pitch angle for which electrons at given surplus energy will be transmitted (without magnetic reflection, see eq. (3.6)). The blue line shows the transmission function without the magnetic mirror effect (eq. (3.8)). The magnetic reflection at the pinch magnet cuts off the transmission function at 50.8°, after which a higher surplus energy does not increase the transmission probability. Figure from [Kle+19].

The shape of the integrated electron energy spectrum as measured with the main spectrometer is given by the convolution of the differential spectrum (eq. (2.21)) with the transmission function. Fitting the integrated spectrum hence allows to determine the neutrino mass. This is illustrated in fig. 3.7.

There are corrections to the spectral shape, including energy broadenings, energy losses due to synchrotron radiation, and scattering of electrons in the source [Kle+19]. These effects are discussed in section 4.1.

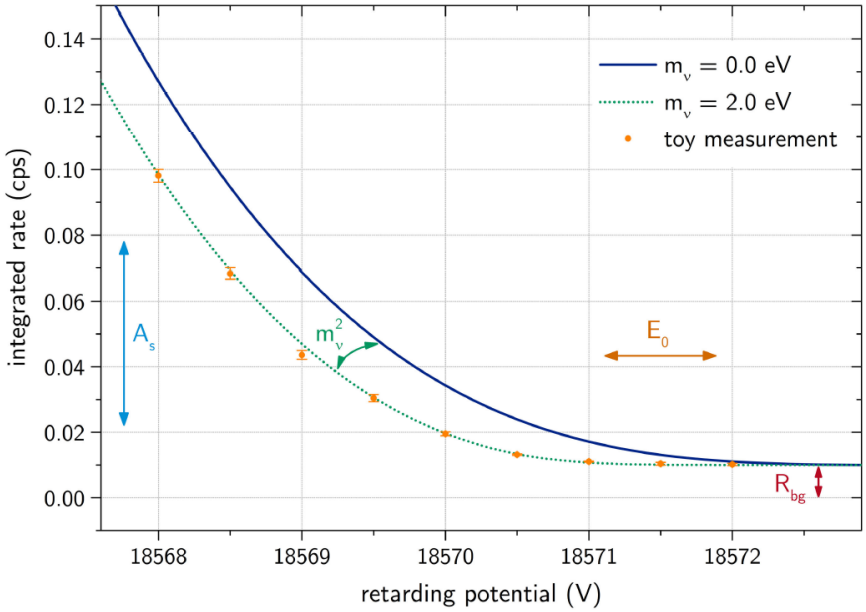

Figure 3.7: The integrated tritium β spectrum in the endpoint region. The blue line shows the expected shape for vanishing neutrino mass. The green line is a fit of toy datapoints (orange) for 2 eV neutrino mass. The fit uses four parameters: Squared neutrino mass m_ν^2, signal amplitude A_s, background R_bg, and endpoint energy E_0, which has to be fitted since it is not known with sufficient accuracy. Figure from [Kle14].

3.3 Plasma Effects in the WGTS

As introduced in section 3.1.2, the windowless gaseous tritium source contains a plasma of secondary electrons and tritium ions produced by the fast β decay electrons. It has an extremely low temperature of 30 K in tritium mode and a low number density of charged particles on the order of $10^{11}\,\mathrm{m}^{-3}$ to $10^{12}\,\mathrm{m}^{-3}$. A detailed description and simulation of the WGTS plasma properties can be found in [Kuc16]. This section shall give a brief overview of the influence of systematic plasma effects on the neutrino mass measurements and their mitigation.

Among other types of systematics measurements, which are not discussed here, the use of $^{83\mathrm{m}}$Kr in the source gives insight on plasma effects. However, since the use of krypton in the WGTS requires to change the temperature to around 80 K or more, as well as reducing the column density, the transformation of krypton results to β scan conditions is a source of additional uncertainty.

The measurement of the β electron decay spectrum relies on precise knowledge of the retarding voltage that the electrons have to surpass. It is defined by the potential in the main spectrometer analysing plane and the starting potential inside the source (both measured with respect to ground potential). This starting potential is influenced by the rear wall of the WGTS, which itself can be put on some potential w.r.t. ground. The plasma, containing free charges, will adopt this potential, in case it couples well to the rear wall. The coupling depends on surface properties of the rear wall, and is only possible within a range of a few volts. Still, not the entire plasma will adopt the same potential. Instead, there might be some spatial distribution, as well as temporal drifts and fluctuations. The properties of the plasma potential inhomogeneities and the physical processes producing it are matter of ongoing research.

However, it is clear that inhomogeneities in the plasma potential influence the shape of the β spectum. There are two main classes of spatial inhomogeneities:

- Radial inhomogeneities produce a radial[1] potential distribution within the plane transversal to the beam axis. This can be taken into account in the analysis, since the focal plane detector has spatial resolution. The radial dependence of the electrons' starting potential can be investigated by measuring an energy shift of ^{83m}Kr conversion electron lines, as is done in this thesis. A way of mitigating plasma inhomogeneities is to adjust the rear wall potential. It was found that the radial inhomogeneity depends on the RW potential, and that there is a setting of maximal homogeneity. This result is being reproduced in this thesis (section 4.2.1). While radial effects can be taken into account in the analysis, it is still preferable to perform neutrino mass measurements at this optimal rear wall setting, since it is assumed that radial and longitudinal inhomogeneities are correlated [Kuc16].

- Longitudinal inhomogeneities are harder to mitigate since they cannot be resolved with the focal plane detector. The count rate of an FPD pixel consists of electrons starting within one longitudinal column of the WGTS. Different starting potentials along this column hence produce a broadening σ of the spectrum. Such a broadening, if not accounted for in the analysis, leads to a shift of the fitted neutrino mass by $\Delta m = -2\sigma^2$. It can be investi-

[1] An azimuthal inhomogeneity is unlikely because of the cylindric symmetry of the WGTS beam tube.

gated by measuring the broadening of ^{83m}Kr conversion electron lines, which is a main subject of this thesis. Another factor influencing the β spectrum are energy losses. The β electrons can scatter on tritium molecules. By inelastic scattering due to excitation and ionisation processes, an electron loses on average 30 eV per scattering. This effect can be included in the fit model of the spectrum by convolving with an energy loss function [Kle+19] (see section 4.1.2). Yet, the scattering probability for an electron starting further back in the source is higher than for an electron starting closer to the transport section end. If there is a longitudinal inhomogeneity of the plasma potential, then scattered electrons will on average have an energy shift according to this inhomogeneity. So if for instance the potential close to the rear wall is relatively negative, then scattered electrons will on average be shifted towards higher energies than expected from the energy loss function. This so-called eloss shift introduces an additional shift of the fitted neutrino mass and can be investigated by scattering of ^{83m}Kr electrons, as is done in [Mac].

Furthermore, temporal dependency of the plasma potential can produce additional smearing and shifts of the spectrum. There are long-term drifts over the course of weeks. In addition, there are investigations of possible short-term fluctuations associated with plasma instabilities, which, for instance, could produce time dependent electric fields in the source.

3.4 Krypton-83m Conversion Electrons

As stated in earlier sections, ^{83m}Kr is used in various sections of KATRIN as a calibration and characterisation tool, in the CPS, the monitor spectrometer, and the WGTS. It is a nuclear standard with sharp conversion electron lines. A systematic shift or broadening of the lines indicates effects that also influence the neutrino mass measurements. This chapter describes the properties of the ^{83m}Kr conversion electron spectrum.

The internal conversion (IC) process is a deexcitation of an excited nucleus, similar to the γ decay. The deexcitation energy ΔE is given by the energy difference of the initial and final state. While in the γ decay ΔE is emitted via a photon, in case of IC the decay energy is transferred directly onto a shell electron, which is subsequently emitted. The kinetic energy of the conversion electron is then defined by ΔE and the binding energy E_{bind} of the orbital the electron was emitted from, as well as nuclear and electronic recoil energy E_{rec}:

$$E_{\mathrm{kin}} = \Delta E - E_{\mathrm{bind}} - E_{\mathrm{rec}}. \tag{3.11}$$

The energy spectrum of the conversion electrons from a single nuclear transition therefore consists of multiple lines representing different atomic orbitals.
The shape of each line is not exactly monoenergetic but has a Lorentzian form

$$L(E) = A \cdot \frac{\Gamma/2}{\pi((E - E_0)^2 + (\Gamma/2)^2)}, \tag{3.12}$$

where A is some amplitude factor and E_0 is the mean line position (not to be confused with the tritium endpoint). The natural line width Γ is connected with the life time τ of the process via the Heisenberg uncertainty principle $\Gamma = \hbar/\tau$.

Typically, a nucleus that undergoes internal conversion can also have γ decay. The branching ratio of the two processes is expressed by the internal conversion coefficent $\alpha_{\mathrm{IC}} = N_{\mathrm{e}}/N_\gamma$ and depends on electromagnetic transition rules.

^{83m}Kr is a metastable decay product of a ^{83}Rb electron capture process (cf. fig. 3.8). The ^{83}Rb nucleus decays with 77.6 % and a half-life of 86.2 d by EC into the metastable ^{83m}Kr state, which deexcites mainly via IC in two cascaded steps. The first deexcitation has a transition energy of roughly $\Delta E = 32.15\,\mathrm{keV}$, a half-life of $T_{1/2} = 1.83\,\mathrm{h}$ and $\alpha_{\mathrm{IC}} = 2035$. The second process has around $\Delta E = 9.4\,\mathrm{keV}$, $T_{1/2} = 150\,\mathrm{ns}$ and $\alpha_{\mathrm{IC}} = 20$ [Bau13].

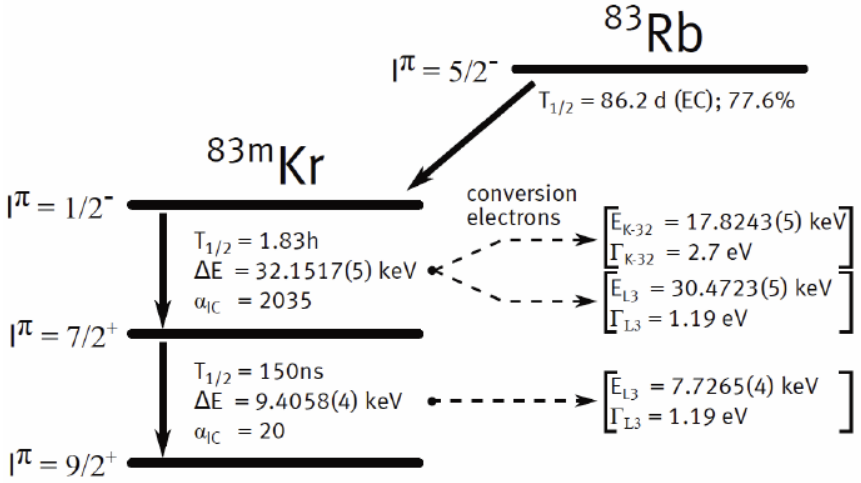

Figure 3.8: The decay scheme of ^{83}Rb into ^{83m}Kr. ^{83}Rb undergoes electron capture, producing the metastable ^{83m}Kr state, which decays in a cascade of two internal conversion processes. The released nuclear deexcitation energy is transferred onto atomic shell electrons. The result is a spectrum of conversion electron lines with energies depending on the binding energy of the respective electron niveau. I is the nuclear spin and π is the parity quantum number of the nuclear state. Figure from [Bau13].

The first transition is of special interest, since the energies of its conversion electron lines reach from around 17 keV to about 32 keV, close as well as far above the tritium endpoint. This and the half-life on the order of hours make this transition very suitable for systematics investigations. When mentioning certain Kr conversion electron lines (L_3, N_2 etc.) throughout this thesis, it is always referred to the ones from the first nuclear transition.

Table 3.1 gives an overview of the conversion lines of the 32 keV nuclear transition. The precise values of line width, position and relative amplitude vary throughout the literature.

In addition to the main conversion lines, there are various satellite lines, which arise from shake processes. The conversion electron can excite (shake-up) or remove (shake-off) a secondary electron from the atom, thus losing energy. The result is the appearance of additional lines in the spectrum below the corresponding main line, with some small fraction of its intensity. These lines have not exactly Lorentzian shape, but a low-energy tail, since the shake-off electron can be emitted with some kinetic energy into the continuum [Vén+18].

Table 3.2 shows the positions and intensities of the shake lines that are taken into account in the data analysis for this thesis.

Table 3.1: Conversion electron lines of the first nuclear deexcitation of ^{83m}Kr. The terms in brackets are the shell the electron was emitted from in nl_J notation, where n is the principal quantum number, and l and J are the orbital and total angular momentum quantum numbers. E_0 and Γ denote the line position and Lorentzian width, respectively. I is the intensity per nuclear deexcitation. Values taken from [Vén+18].

	E_0(eV)	I(%)	Γ(eV)
K ($1s_{1/2}$)	$17\,824.2 \pm 0.5$	24.8 ± 0.5	2.71 ± 0.20
L_1 ($2s_{1/2}$)	$30\,226.8 \pm 0.9$	1.56 ± 0.02	3.75 ± 0.93
L_2 ($2p_{1/2}$)	$30\,419.5 \pm 0.5$	24.3 ± 0.3	1.25 ± 0.25
L_3 ($2p_{3/2}$)	$30\,472.2 \pm 0.5$	37.8 ± 0.5	1.19 ± 0.24
M_1 ($3s_{1/2}$)	$31\,858.7 \pm 0.6$	0.249 ± 0.004	3.5 ± 0.4
M_2 ($3p_{1/2}$)	$31\,929.3 \pm 0.5$	4.02 ± 0.06	1.6 ± 0.2
M_3 ($3p_{3/2}$)	$31\,936.9 \pm 0.5$	6.24 ± 0.09	1.1 ± 0.1
M_4 ($3d_{3/2}$)	$32\,056.4 \pm 0.5$	0.0628 ± 0.0009	0.07 ± 0.02
M_5 ($3d_{5/2}$)	$32\,057.6 \pm 0.5$	0.0884 ± 0.0012	0.07 ± 0.02
N_1 ($4s_{1/2}$)	$32\,123.9 \pm 0.5$	0.0255 ± 0.0004	0.40 ± 0.04
N_2 ($4p_{1/2}$)	$32\,136.7 \pm 0.5$	0.300 ± 0.004	0.03
N_3 ($4p_{3/2}$)	$32\,137.4 \pm 0.5$	0.457 ± 0.006	0.03

Table 3.2: Shake lines of the L_2 and L_3 conversion electrons of the 32 keV nuclear transition of ^{83m}Kr. I_{rel} is the intensity relative to the main line. The phenomenological denotation S1, S2, S3 enumerates the lines according to their position E_0. Some of the lines actually consist of two seperate transitions that cannot be distinguished with a KATRIN krypton mode measurement. In this case, they are treated as a single line with the sum of the intensities. Values taken from [Vén+18] and [Mac16].

	E_0(eV)	I_{rel}(%)
L_2^{S1}	30 262.58	1.7+2.6
L_2^{S2}	30 379.40	1.9
L_2^{S2}	30 403.52	4.7+9.9
L_3^{S1}	30 314.88	1.7+2.6
L_3^{S2}	30 431.70	1.8
L_3^{S3}	30 455.82	4.7+9.8

4 Krypton Analysis

For this thesis, measurements of three conversion electron lines of the 32 keV nuclear transition of ^{83m}Kr were analysed, which have various advantages and disadvantages for different investigations.

The $\mathbf{L_3}$ line has high intensity, thus providing relatively good statistics. The well-defined line position serves as a tool to probe systematic energy shifts. In section 4.2.1, this is used to investigate radial potential homogeneity of the WGTS depending on the rear wall potential setting.

However, the L_3 line is not so well suited to measure energy broadenings σ, since its shape is dominated by the relatively large natural line width of $\Gamma \approx 1.1$ eV. The line width is not known with sufficent precision from an independent measurement to leave it fixed in the analysis. When fitting the L_3 line with the model presented in section 4.1, free Γ and σ parameters would be highly anticorrelated. Therefore, σ is fixed to zero and a free Γ is used as a proxy to any broadening. Yet, as will be shown in section 4.2.2, a Gaussian broadening of reasonable magnitude would only have little influence on the fitted Γ.

Hence any systematic effect influencing the L_3 line width will severely reduce the sensitivity on the broadening. The width parameter is highly dependent on the non constant background that was observed in the region above the L_3 line. The origin of this in general nonlinear slope is not yet fully understood. It depends strongly on the magnetic field setting in the analysing plane of the main spectrometer. For small B_{ana} the background slope is positive and likely to be produced by non-adiabatic transport of electrons from higher krypton lines. For higher B_{ana}, the non-adiabatic effects become miniscule. Yet, there remains a negative nonlinear background slope of much smaller magnitude, which is largely produced by the tail of other krypton lines that lie below L_3. Still, there seems to be another component coming from other effects, which is not understood well so far. In section 4.2.3, the analysis of the background slope is presented.

The $\mathbf{N_2}$ and $\mathbf{N_3}$ lines are more suited to investigate broadenings. These electrons originate from the outermost orbitals of the krypton atom. Since there are no electrons from higher levels to fill the vacancy, the life time is very long and therefore the natural line width is extremely small. Hence, N_2 and N_3 are very sensitive to small broadenings. Additionally, background slope is less of an issue,

since there are no higher lines that could be subject to non-adiabatic transport, and the lines below the N lines are comparatively far away or rather weak, which reduces the background slope comming from those lines. On the other hand, the intensity of N_2 and N_3 is two orders of magnitude smaller than L_3, which reduces statistical significance and makes the measurement and analysis more challenging. N_2 and N_3 are so close to each other that they cannot be measured independently. Therefore, they are referred to as the N_{23} doublet in the following. The analysis of N_{23} is described in section 4.3.

In general, performing krypton measurements with and without tritium in the WGTS allows to investigate the influence of plasma related effects. In addition, different analysing plane magnetic fields B_{ana} are suited for different purposes. The aforementioned L_3 background slope can largely be mitigated by going to a stronger field like $B_{\mathrm{ana}} = 6.3\,\mathrm{G}$. Yet, a lower field like $B_{\mathrm{ana}} = 2.7\,\mathrm{G}$ produces a more narrow transmission function and therefore a better energy resolution. The systematic uncertainty on the magnetic field is smaller for lower B_{ana} as well. In the 1.0 G setting this is again improved, but part of the electrons from the outer part of the flux tube are guided towards the spectrometer walls, allowing to use signal only from the inner detector rings.

The data analysed for L_3 and N_{23} were taken during the systematics measurement phases of the KNM3 campaign (KATRIN Neutrino Mass 3) throughout 2020. The datataking is proceeded in form of runs. For each run, the main spectrometer scans once through the integrated spectrum around the line. The scanning direction is alternating. Combining up and down scans allows to cancel out linear drifts of source activity, or energy shifts that depend on scan direction. The measurement data are saved in run summary files that are used as input for this analysis. Usually, the spectrum is measured in terms of discrete retarding potential points that are set according to some measurement time distribution (MTD). For the N_{23} scans, a different technique was used, which ramps through the retarding potential continuosly, hereby saving dead time that is needed to set the voltage stepwise.

The following section 4.1 presents the integrated spectrum model used for the analysis. It incorporates the experiment's response function as well as the differential shape of the krypton lines. The modelling of the latter is described in the analysis chapter of the respective line.

4.1 Modelling the Integrated Spectrum

The integrated spectrum $I(qU)$, measured with the main spectrometer, is in a simplified way described by

$$I(qU) = \int_{qU}^{\infty} \mathrm{d}E \; T(E, qU) D(E), \tag{4.1}$$

where $D(E)$ is the differential electron energy spectrum and $T(E, qU)$ is the transmission function (see eq. (3.10)). For the analysis of this thesis, some extensions to this model are considered, which will be described in the following.

4.1.1 Energy Broadenings

As in any spectroscopic experiment, there are energy smearings that lead to a broadening of the observed line. Assuming that this broadening is of Gaussian shape,

$$G(E, \sigma) = \frac{1}{\sqrt{2\pi\sigma^2}} \exp\left(-\frac{E^2}{2\sigma^2}\right), \tag{4.2}$$

then the differential line $D(E)$ is given by the convolution of G with the Lorentzian natural line shape $L(E, \Gamma)$ (cf. eq. (3.12)):

$$D(E) = (L * G)(E). \tag{4.3}$$

The result is a Voigt profile $V(E)$, for which there is no analytical expression. Yet, it can be written in terms of the Faddeeva function $w(z)$ [FT54]:

$$V(E, \sigma, \Gamma) = \frac{\mathrm{Re}[w(z)]}{\sigma\sqrt{2\pi}}, \quad z = \frac{E + i\Gamma/2}{\sigma\sqrt{2}}. \tag{4.4}$$

$w(z)$ is a scaled complex error function, for which numeric approximations exist and are used in this analysis.

One source of broadening is the Doppler effect, which smears out the energy spectrum depending on the temperature T of the source gas. The Doppler broadening is given by [Kle+19]

$$\sigma_\mathrm{D} = \sqrt{(E + 2m_\mathrm{e}) E k_\mathrm{B} T / M}, \tag{4.5}$$

where k_B is the Boltzmann constant and M the mass of ^{83}Kr. The Doppler

broadening amounts to 53.1 meV for L_3 electrons and 54.6 meV for N_{23} at the $T = 78.8\,\mathrm{K}$ used in krypton mode.

4.1.2 Scattering on Tritium in the Source

The signal electrons can scatter on tritium, hereby losing energy. The scattering can be elastic or inelastic. The elastic energy loss is on the order of a few meV and is neglected [Kle+19]. The inelastic part consists of various excitation and ionization processes of the tritium molecules. It is expressed by an energy loss function $f(\epsilon)$, which has been measured, and parametrised as three Gaussians describing excitation states, plus an ionisation tail [Ake+19; Sac20; Gro20]. It is plotted in fig. 4.1. It is noteworthy that it was measured for electrons with β spectrum endpoint energies around 18.6 keV, while the krypton lines analysed in this thesis are on the order of 30-32 keV. How the energy loss differs between these conditions is unknown and planned to be measured in the future.

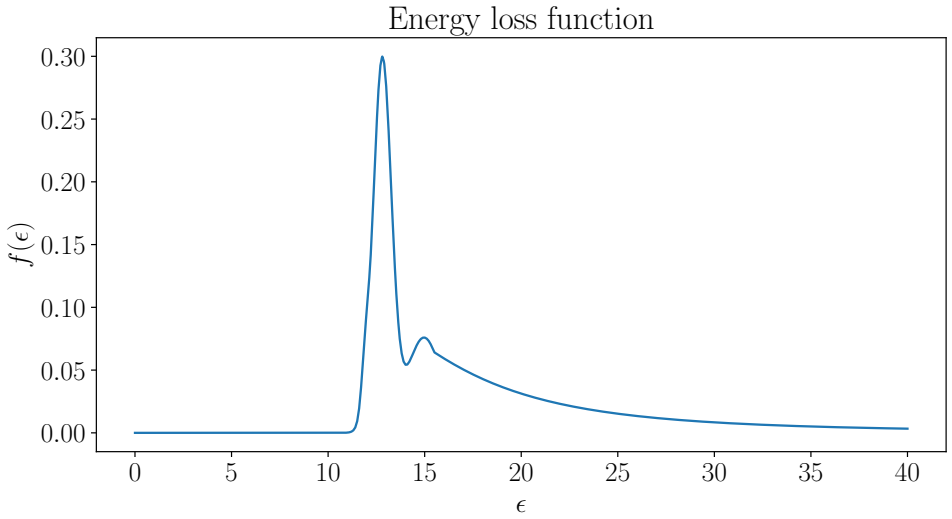

Figure 4.1: The energy loss function $f(\epsilon)$, describing the probability for an electron to lose the energy ϵ by inelastic scattering on tritium T_2 molecules. The distribution is normalized to 1: $\int_0^\infty \mathrm{d}\epsilon f(\epsilon) = 1$.

$f(\epsilon)$ describes the probability of a scattered electron to lose the energy ϵ. Since electrons can scatter multiple times, the energy loss function for s scatterings is given by the s-fold convolution of $f(\epsilon)$ with itself,

$$f_s(\epsilon) = (\underbrace{f * f * ... * f}_{s \text{ times}})(\epsilon), \tag{4.6}$$

which is calculated numerically.

Scattering becomes increasingly unlikely with higher s. The probability arises from a Poisson distribution:

$$P_s(z,\theta) = \frac{(\mathcal{N}_{\text{eff}}(z,\theta)\cdot\sigma_{\text{Tr}})^s}{s!}\cdot\exp(-\mathcal{N}_{\text{eff}}(z,\theta)\cdot\sigma_{\text{Tr}}). \tag{4.7}$$

σ_{Tr} is the inelastic scattering cross section, which is slightly energy dependent. For electrons from the krypton L_3 line it is $\sigma_{\text{Tr}} = 2.41\cdot10^{-22}\,\text{m}^2$, and for the N_2 and N_3 lines it is $\sigma_{\text{Tr}} = 2.31\cdot10^{-22}\,\text{m}^2$ [Glü]. P depends on the electron pitch angle θ, since electrons with higher angle have to traverse a larger amount of tritium to leave the WGTS. θ enters the effective column density $\mathcal{N}_{\text{eff}}$ the electron has to cross, depending on its longitudinal starting position z:

$$\mathcal{N}_{\text{eff}} = \frac{1}{\cos\theta}\cdot\int_z^{z_{\text{end}}}\text{d}z'\ \rho_{\text{Tr}}(z'). \tag{4.8}$$

Here, the gas inlet is at $z = 0$, and $z_{\text{end}} = 5.0075\,\text{m}$ is the distance to the end of the WGTS beam tube towards the transport section. $\rho_{\text{Tr}}(z)$ is the volume density of tritium, assumed to be only depending on the longitudinal position, and homogenous in the transversal plane [Kle+19].

The probability to measure a krypton electron that scattered s times also depends on the density profile of the krypton gas ρ_{Kr}, since it determines the number of krypton electrons that start at some point z. Therefore, it follows

$$P_s(\theta) = \int_{z_{\text{start}}}^{z_{\text{end}}}\text{d}z\ P_s(z,\theta)\rho_{\text{Kr}}(z), \tag{4.9}$$

with $z_{\text{start}} = -5.0745\,\text{m}$ as the position of the WGTS beam tube end towards the rear section.

The gas profiles, which depend on temperature, column density and pressure conditions, have been simulated by M. Machatschek [Mac]. They are plotted in fig. 4.2. The assumed column density ρd_{Tr} of tritium is 40 % of the nominal value $\rho d_0 = 5\cdot10^{17}\,\text{cm}^{-2}$, and the temperature is 80 K, which are the settings used for the krypton measurements analysed in this thesis. The plotted profiles are in arbitrary units. When including them in the analysis, the z-integration over the tritium profile has to be normalized to the given tritium column density.

With higher tritium column density, the scattering probability will increase (cf. eq. (4.7)). The krypton column density is just an arbitrary normalization factor scaling the overall krypton intensity, assuming that the krypton profile shape remains unchanged.

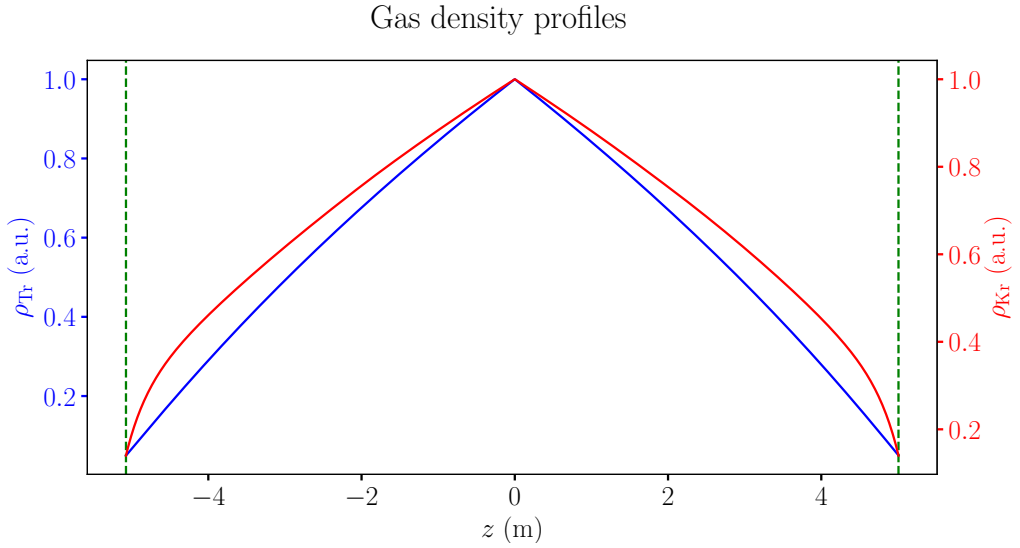

Figure 4.2: The tritium (blue) and krypton (red) volume density as function of beam tube position, for $T = 80\,\mathrm{K}$ and 40 % tritium column density. The WGTS inlet is at $z = 0$. The green vertical lines mark the end of the beam tube, beyond which the gas density is assumed to be zero.

Since the scattering is angular dependent, the transmission condition (eq. (3.6)) cannot be simply integrated over an isotropic angular distribution to obtain the transmission function, as it was done in section 3.2. Instead, the so-called detailed transmission for an s times scattered electron is given by

$$T_s(E, qU) = \int_0^{\theta_{\max}} \mathrm{d}\theta \; \mathcal{T}(E, qU, \theta) \sin\theta P_s(\theta). \tag{4.10}$$

This integration has to be done numerically, which increases computation time considerably. Yet, it can influence the fitted line widths and broadenings to significant extent. The full detailed transmission function is then the sum over all s:

$$T_{\mathrm{det}}(E, qU) = \sum_s T_s(E, qU). \tag{4.11}$$

Overall, the energy loss is incorporated in the integrated spectrum model by replacing the transmission function with a response function R, which involves a

convolution of transmission and energy loss function:

$$R_{\mathrm{det}}(E, qU) = \sum_s \int_0^{E-qU} \mathrm{d}\epsilon \; T_s(E - \epsilon, qU) f_s(\epsilon). \tag{4.12}$$

The upper integration limit arises from the fact that an electron losing more than the surplus energy $E - qU$ cannot pass the analysing plane.

When neglecting detailed transmission, the scattering probabilty $P(\theta)$ can be integrated over the isotropic distribution and normalized [Kle+19]:

$$P_s = \frac{1}{1 - \cos\theta_{\mathrm{max}}} \int_0^{\theta_{\mathrm{max}}} \mathrm{d}\theta \; P_s(\theta) \sin\theta. \tag{4.13}$$

In this case the analytic transmission function (eq. (3.10)) can be used, and it follows

$$R(E, qU) = \sum_s P_s \int_0^{E-qU} \mathrm{d}\epsilon \; T(E - \epsilon, qU) f_s(\epsilon). \tag{4.14}$$

The scattered electrons form additional steps in the integrated spectrum. Most pronounced is the $s = 1$ scattering step. However, when not fitting the spectrum close to it, the scattering can be neglected.

4.1.3 Synchrotron Losses

An electric charge that is deflected from a straight trajectory loses energy in form of electromagnetic radiation, called synchrotron radiation.

In KATRIN the signal electrons are also subject to this effect, mainly inside the transport section, and to lesser extent in the source section, when they are deflected by the present magnetic fields. These synchrotron losses influence the transmission properties of the beamline, and if not taken into account will significantly influence the result of a krypton line fit. An effective model to incorporate them in the transmission function was developed by J. Behrens and A. Lokhov [BL19]. The scheme is presented in the following.

The energy loss due to synchrotron radiation for an electron of charge e and mass m_{e} propagating through a region of length l with uniform magnetic field B

is given by [Gro15]

$$\Delta E(\cos\theta, B, l) = -\frac{\mu_0}{3\pi c}\frac{e^4}{m_\mathrm{e}^3} B^2 E \sin^2\theta\gamma \frac{l}{v\cos\theta}, \tag{4.15}$$

where μ_0 is the permeability of the vacuum, θ is the pitch angle, E the kinetic energy, γ the relativistic Lorentz factor and v the velocity of the electron. The contributions of source and transport sections are

$$\Delta E_\mathrm{tot}(\cos\theta, B_\mathrm{S}, B_\mathrm{T}, l_\mathrm{S}, l_\mathrm{T}) = \Delta E(\cos\theta, B_\mathrm{S}, l_\mathrm{S}) + \Delta E(\cos\theta, B_\mathrm{T}, l_\mathrm{T}), \tag{4.16}$$

with $l_\mathrm{S} = 5\,\mathrm{m}$ as the mean path length for an electron in the source, and $l_\mathrm{T} = 14\,\mathrm{m}$ the length of the transport section. The effective magnetic field in the transport section is $B_\mathrm{T} = 3.6\,\mathrm{T}$, and in the source typically $B_\mathrm{S} = 2.52\,\mathrm{T}$, as introduced earlier. The pitch angle in the transport section is different from the starting angle:

$$\sin\theta_\mathrm{Tr} = \sin\theta \cdot \sqrt{\frac{B_\mathrm{T}}{B_\mathrm{S}}}. \tag{4.17}$$

The electron motion is assumed adiabatic, and the change in angle due to synchrotron radiation is rather small [Kle+19].

Next, the transmission condition (eq. (3.6)) has to be modified by the synchrotron loss, $E \to E + \Delta E_\mathrm{tot}$, and becomes

$$\mathcal{T}(E, qU, \theta) = \begin{cases} 1 & \text{if } \; (E + \Delta E_\mathrm{tot}(\theta))\left(1 - \sin^2\theta \frac{B_\mathrm{ana}}{B_\mathrm{source}} \frac{\gamma+1}{2}\right) > qU \\ 0 & \text{else.} \end{cases} \tag{4.18}$$

To obtain the transmission function, an integration over the isotropic angular distribution and, when considered, angular dependent scattering probabilties would be the next step, as described in sections 3.2 and 4.1.2. On the other hand, using the model assumption that the synchrotron loss only depends on the starting pitch angle, ΔE_tot can be fixed to $\Delta E_\mathrm{tot}(\theta_\mathrm{t})$. Here, θ_t is the transmission angle, defined as the solution of the equation

$$(E + \Delta E_\mathrm{tot}(\theta_\mathrm{t}))\left(1 - \sin^2\theta_\mathrm{t} \frac{B_\mathrm{ana}}{B_\mathrm{source}} \frac{\gamma+1}{2}\right) = qU. \tag{4.19}$$

This equation is solved numerically for θ_t. Then, the transmission function with

synchrotron losses reads

$$T_{\text{synchro}}(E, qU) = T(E + \Delta E_{\text{tot}}(\theta_{\text{t}}), qU), \tag{4.20}$$

where $\Delta E_{\text{tot}} < 0$.

4.1.4 Full Integrated Spectrum Model

When considering scattering, detailed transmission and synchrotron losses, the integrated spectrum depending on the differential line $D(E)$ is given by

$$I(qU) = \int_0^\infty \mathrm{d}E \int_0^{E-qU} \mathrm{d}\epsilon \int_0^{\theta_{\max}} \mathrm{d}\theta \sum_s \mathcal{T}(E - \Delta E_{\text{tot}}(\theta_{\text{t}}) - \epsilon, qU, \theta) \sin\theta P_s(\theta) f_s(\epsilon) D(E) + bg(qU). \tag{4.21}$$

The background model bg is in the simplest case constant, but can also be set to some linear or any other function of qU.

In the analysis, this three-dimensional integration is calculated numerically for every point qU of the measured spectrum, to fit various model parameters of the line $D(E)$ and the background to the data. The fit model was implemented in `Python 3`, based on work by A. Fulst [Ful]. It uses the `iminuit` package for the minimizer. Synchrotron losses, scattering, and detailed transmission can be turned off when not needed, to decrease computation time. Further description follows in the chapter of the respective analysis.

As described in section 3.1.3, the focal plane detector is segmented into 12 rings of equal area, plus the bullseye with 1/3 of this area. Since the area is constant, the thickness of the rings decreases with the ringnumber. The ring radius r_i, here defined as the distance from the FPD center to the middle of ring i, is given in table 4.1. Due to geometrical cut-off, some pixels are not properly hit by the flux tube and are excluded in the analysis. These pixels are also listed in table 4.1.

Performing the fit of the integrated spectra ringwise allows to gain information about radial dependent effects. The electromagnetic fields that define the transmission function are not exactly homogenous throughout the transversal plane but vary on the 1 % level. Simulations with the `KASSIOPEIA` software [Fur+17] map the electromagnetic fields. The result is saved in so-called period summary files that are used as input for the analysis to correct for these effects. This allows

Table 4.1: The 13 FPD rings with radius r_i, defined as the distance from center to the middle of the ring. In rings 9 to 12, some pixels are not properly hit by the flux tube due to geometrical cut-off, and are therefore rejected in the analysis.

Ring	r (mm)	Pixels	Rejected pixels
0	3.74	0–3	–
1	11.23	4–15	–
2	17.39	16–27	–
3	21.74	28–39	–
4	25.33	40–51	–
5	28.46	52–63	–
6	31.28	64–75	–
7	33.87	76–87	–
8	36.27	88–99	–
9	38.52	100–111	99, 100
10	40.64	112–123	112, 113, 123
11	42.66	124–135	124–130, 135
12	44.59	136–147	136–142, 145–147

to define pixel dependent transmission functions. A ringwise analysis necessarily uses a common transmission function with electromagnetic fields averaged over the pixels of the considered ring. Hence, there is some smearing of the transmission shape. On the other hand, the statistics for each fit is much increased by combining multiple pixels to rings, improving numerical stability of the fit. Also the computation time is drastically reduced.

4.2 Analysis of the Krypton L_3 Line

The L_3 line is modelled as a Lorentzian shape

$$D(E) = A \cdot \frac{\sqrt{\Gamma^2}/2}{\pi((E - E_0)^2 + \Gamma^2/4)}, \tag{4.22}$$

as described in section 3.4. Fit parameters are the amplitude A, a squared line width Γ^2, and the mean line position E_0, as well as parameters of the background model. Figure 4.3 shows a simulated L_3 spectrum. The red line marks the position and shape of the differential Lorentzian spectrum, assuming a constant background $bg = bg_0$. The blue line is the integrated spectrum, taking into account synchrotron losses, as well as once scattered electrons and detailed transmission for 40 % tritium column density. The scattered electrons form a second step in the integrated spectrum, clearly pronounced around 15 eV below the line.

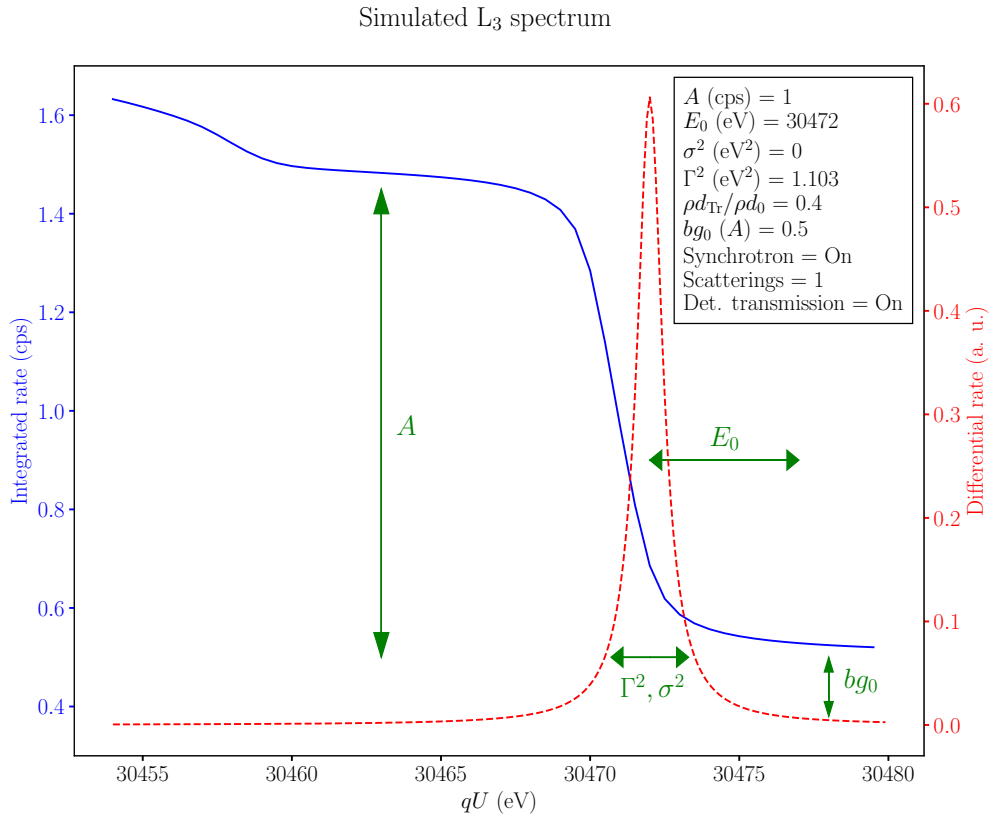

Figure 4.3: The integrated spectrum model (blue) of the Lorentzian shaped L_3 line (red). The right box shows the simulation settings. The integrated rate amplitude is set to 1. The differential rate is scaled arbitrarily. The green arrows indicate the effect of the model parameters on the spectral shape. The step in the integrated spectrum around 30 455 eV is produced by electrons that scattered once.

The figure also illustrates the influence of the model parameters on the spectral shape. The amplitude A is defined as the rate for $qU \to 0$ (full transmission), without scattered electrons, and minus the background. In the implementation, the background parameters are modelled as coefficients of the amplitude, since the background is mainly produced by Kr electrons and thus proportional to the overall rate. Stating bg in units of A simplifies the comparison of different spectra.

As stated earlier, adding a Gaussian broadening σ^2 does not influence the L_3 line shape significantly, since it is dominated by the natural line width. In section 4.2.2, a simulation of the relation of Γ^2 and σ^2 for L_3 is presented. In section 4.2.3, the model is extended by introducing non constant background

models, as well as additional krypton lines. The following section investigates the rear wall potential dependency of the radial line position homogeneity.

4.2.1 Radial Line Position Homogeneity Depending on Rear Wall Potential

The position of the L_3 line is well defined and rather independent of the used background model (see section 4.2.3.1). It can hence directly be used to investigate energy shifts, for instance caused by a radial dependent plasma potential. In this section, the ringwise line position depending on the rear wall potential is being investigated. The used datasets are listed in table 4.2.

Table 4.2: The used datasets and fit settings for the analysis of the rear wall potential dependent line position.

Name	L_3-a	L_3-b
Gas composition	Kr only	Kr+Tr, 40 % CD
B_{ana}	2.7 G	2.7 G
Run numbers	61304-61369	61529-61578 w/o every 3rd run
Campaign/time	KNM3/end of May	KNM3/end of May
RW potential (V)	-5 to 5	-5 to 5
Energy range (eV)	30464-30480	30460-30480
Add. Gaussian broad.	–	–
Synchrotron	On	On
Scattering	Off	On
Det. transmission	Off	On
Background model	constant	constant

4.2.1.1 Krypton only The first dataset L_3-a was measured during KNM3 at the end of May 2020. It was performed in Kr only mode, i.e. no tritium was in the source. B_{ana} was set to 2.7 G. A range of rear wall potentials from -5 V to 5 V was measured throughout 66 runs, each taking 20 min. Every run was fitted ringwise. The rear wall potential is measured with respect to ground potential, on which the WGTS beam tube is. Figure 4.4 shows an examplary fit of data from a single detector ring. The measurement time per voltage setpoint is $t = 39$ s. The uncertainty of the rate $\dot{N}$ is given by $u(\dot{N}) = \sqrt{\frac{\dot{N}}{t}}$. A constant background $bg(qU) = bg_0$ was assumed. Tritium scattering and detailed transmission are not included in the fit model since they can be neglected in Kr only mode. Synchtrotron losses are considered.

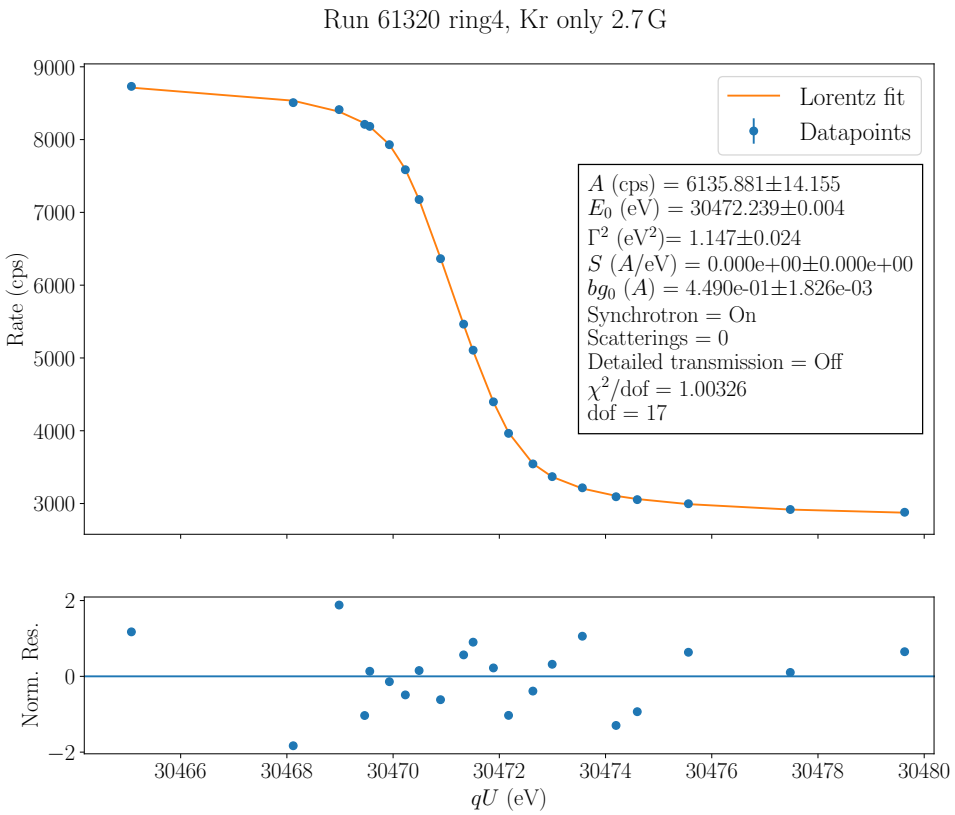

Figure 4.4: Fit of run 61320 ring4 (Kr only 2.7 G). The lower part of the diagram shows the normalized residuals $(\dot{N} - \dot{N}_{\text{model}})/u(\dot{N})$. The right box displays the fit result and settings.

The overall results for line position, width, and reduced χ^2 are plotted in fig. 4.5. The errorbars of the datapoints are from statistical uncertainties only. Some of the runs were measured at the same RW potential. In this case, the resulting fit parameters of the respective runs were averaged, using a fit with a constant line to account for the uncertainties of the parameters.

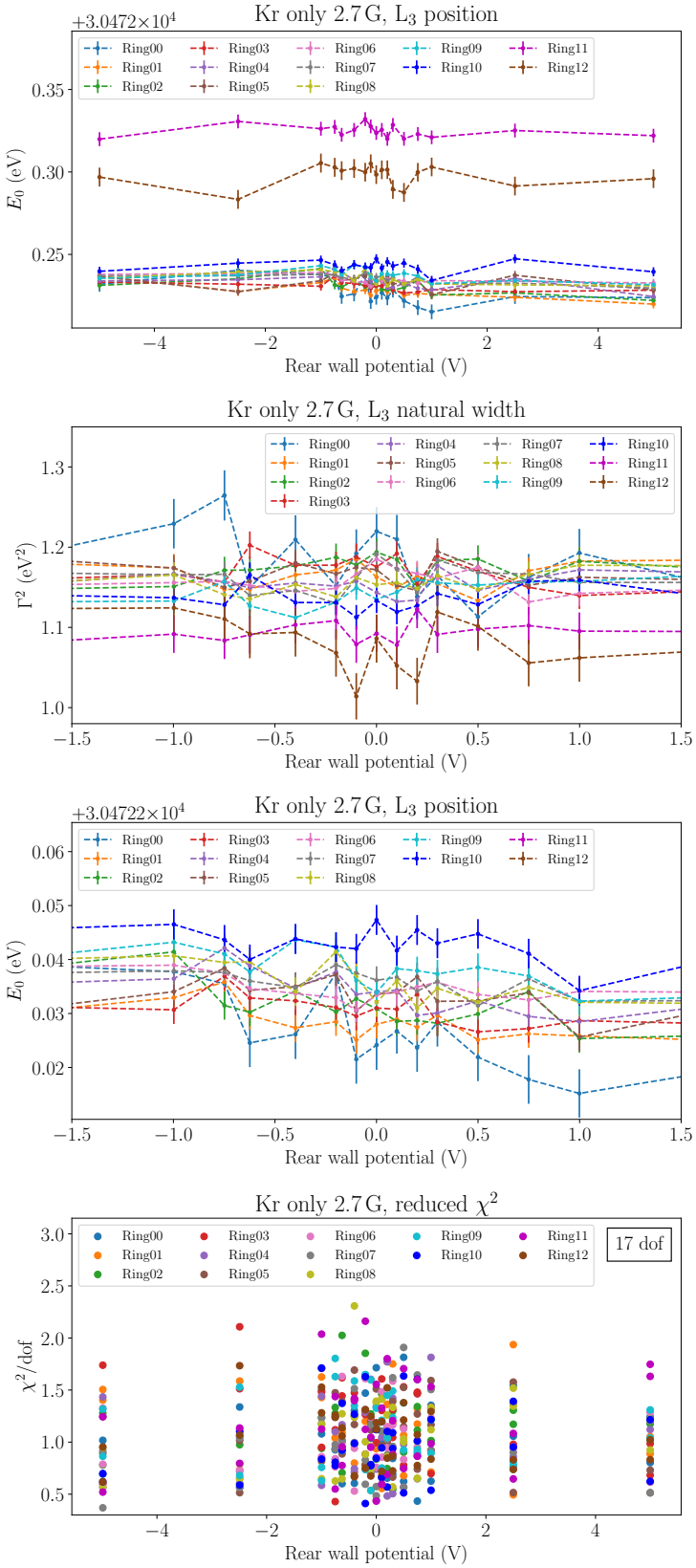

Figure 4.5: Krypton line parameters of L_3-a as function of rear wall potential for different detector rings. From top to bottom: a) line position, b) Lorentzian width zoomed into central region, c) line position zoomed into central region, d) reduced χ^2 for 17 degrees of freedom (dof) per fit. The fit parameters are averaged over runs with same RW potential. Only statistical uncertainties are plotted.

The line position is overall consistent with the literature value given in table 3.1. As can be seen, the line position is ring dependent on the order of 10-20 meV for ring0 to 10, while ring11 and 12 have much higher line position. This is probably due to a misalignment of the FPD. It is shifted by a few milimeters, so that its center does not align perfectly with the center of the analysing plane. The electric potential is not exactly constant across this plane, but has a parabolic shape with a minimum potential in the center. This inhomogeneity is being accounted for in the period summaries, as mentioned earlier. But if the FPD is shifted by a small amount that is not considered, the electric potential is mismatched and a dipole shaped structure of fitted line positions emerges across the FPD pixels. When performing ringwise fits over full rings, this effect mainly cancels out, though there is still some ring dependent line position left. Yet, rings 11 and 12 contain many rejected pixels (cf. table 4.1), and therefore keep a large shift in line position.

Overall, the line position is relatively constant with respect to the rear wall potential, compared with the Kr+Tr case that will be discussed later.

Also, the natural line width parameter appears overall constant with respect to the RW potential, while outer rings have a tendency to smaller widths. This can be a result of the not considered positive background slope that appears in the 2.7 G setting (see section 4.2.3.2).

4.2.1.2 Krypton plus tritium The second dataset L_3-b was measured shortly after L_3-a, also in 2.7 G, but additionally with tritium in the source. The column density (CD) was, as for all Kr+Tr data analysed for this thesis, at 40 % of the nominal value. The 32 runs span a RW potential range from -5 V to 5 V. Synchrotron losses, one scattering and detailed transmission are included in the fit model. As shown in fig. 4.6, the behaviour of the line parameters has changed drastically compared to the Kr only case. In a region of -5 V to about -0.4 V, the line position stays independent of the rear wall potential, while outer rings have smaller energy (this excludes rings 11 and 12, which are off due to the misalignment of the FPD mentioned earlier). The splitting of the energies is on a scale of 300 mV, much larger than for Kr only. Going to higher potentials, the line position drops, while the ordering of the rings inverts in some crossing region. In fig. 4.6, the radial homogeneity of the position is estimated via the standard deviation of the individual rings' line positions (leaving out rings 11 and 12). It shows a minimum around 100 mV. For very high RW potentials, the spread of the line positions increases drastically.

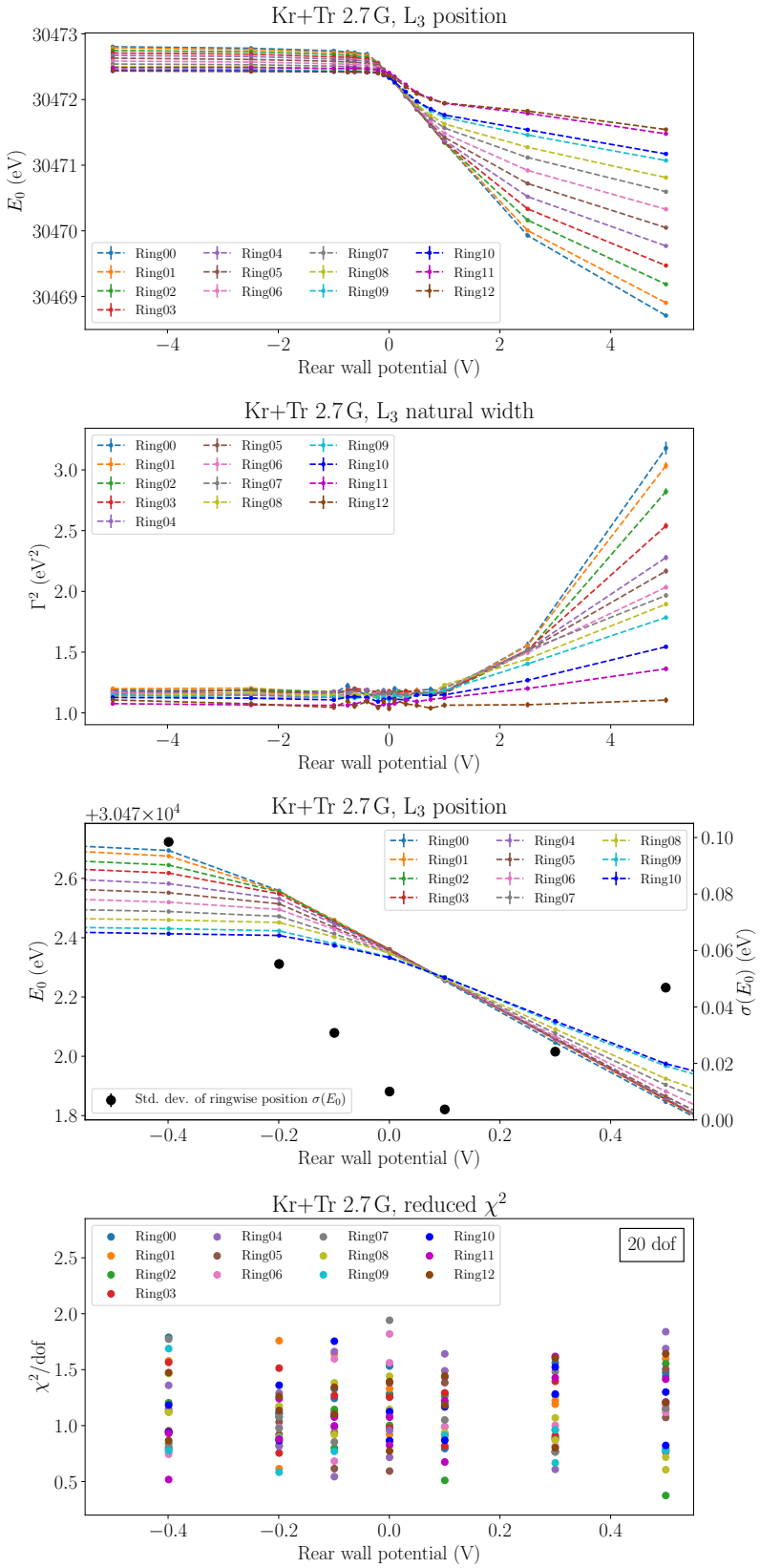

Figure 4.6: Krypton line parameters of L_3-b as function of rear wall potential for different detector rings. From top to bottom: a) line position, b) Lorentzian width, c) line position zoomed into central region, with the standard deviation of the ringwise positions in black, d) reduced χ^2 zoomed into the central region. The fit parameters are averaged over runs with the same RW potential. Only statistical uncertainties are plotted.

The line width remains rather constant with a ring spread comparable to the Kr only conditions. When going to 2.5 V and 5 V, the spread increases, as especially inner rings get very high width parameters.

The observed behaviour can be explained by a proposed model of the plasma interactions with the rear wall and beamtube of the WGTS, that will be briefly sketched in the following.

For very negative RW potential, the plasma does not couple to the rear wall. Free electrons are repelled from it, and therefore a negative space charge accumulates throughout the WGTS. Kr signal electrons starting closer to the grounded beam tube walls are on a more positive potential, shifting the line position of outer rings to smaller values. The electron repulsion effect is in saturation, wherefore a change in RW potential does not shift the Kr line position. This is until at around -0.4 V, when the saturation ends and the space charge deaccumulates. Now the plasma couples to the rear wall, which defines the potential of the plasma due to its longitudinal conductivity. Yet, it does not couple in the same way to the beam tube walls, since the radial conductivity is suppressed by the magnetic field lines. As the rear wall potential becomes larger, the Kr signal electrons lose energy and the line position drops. For the inner rings, the position change in the good coupling regime is directly given by the change in rear wall potential, while the outer rings are affected by the beam tube walls. As the RW potential increases, the difference to the beam tube wall potential gets smaller and the ringwise line positions converge. At some point the radial spread of line positions is minimal. This point is not at ground potential due to the different work functions of the rear wall and beam tube walls. When going to even higher RW potentials, the difference of RW and beam tube potential grows, but with opposite sign, and the ring ordering is inverted. The fact that the saturation behaviour is not mirrored for positive rear wall potentials originates from the lower mobility of positive tritium ions compared to electrons.

Eventually, large longitudinal plasma inhomogeneities emerge, strongly increasing the fitted Lorentzian width. At this point, the model does not fit the data well anymore. However, this setting is not of further interest. Instead, neutrino mass measurements are supposed to be taken at the point of best radial homogeneity, where radial and correlated longitudinal plasma effects are maximally mitigated [Kuc16; Ost20].

4.2.1.3 Conclusion There is a significant difference of the ringwise line positions between Kr only and Kr+Tr settings. This can be explained by the behaviour of the tritium plasma, which is influenced by the rear wall potential setting. With tritium in the source, the radial spread of the line position depends strongly on the RW potential. At about $-0.4\,\mathrm{V}$ the plasma starts to couple to the RW. The radial line position is now dependent on the difference of RW and beam tube potentials. Around 100 mV the radial homogeneity is maximal. This setting is thus preferable for neutrino mass measurements. However, as other measurements have shown, this point can drift over time, probably due to changing of work functions of RW or beam tube. Therefore, this investigation should be repeated regularly, in order to monitor such change of source conditions.

4.2.2 Relation of Lorentzian and Gaussian Width for L_3

In this section, the relation between the Lorentzian width Γ and a Gaussian broadening σ for the L_3 line is investigated. With Γ being a physical constant, what is expected from energy smearing effects is actually a probably Gaussian shaped broadening of the line. However, the reference value of Γ is not known with high precision. Therefore, using a Voigt profile with Γ fixed to this value and fitting σ, or even introducing a pullterm for Γ and fitting both parameters, would lead to a very high uncertainty for σ. The reason is that the spectrum is dominated by the Lorentzian shape, which is on the order of $\Gamma \approx 1\,\mathrm{eV}$. In contrast, from the N_{23}-doublet measurements (section 4.3) the broadening is expected to be at most $\sigma \approx 0.1\,\mathrm{eV}$. The widths approximately have to be added in squares, as will be shown below. Using the literature value from table 3.1, $\Gamma = (1.19 \pm 0.24)\,\mathrm{eV}$, and transforming to squared width, $\Gamma^2 = (1.42 \pm 0.57)\,\mathrm{eV}^2$, the uncertainty is an order of magnitude larger than the expected Gaussian broadening $\sigma^2 \lesssim 0.01\,\mathrm{eV}^2$. Therefore, finding a Gaussian line broadening using the L_3 line would require a much better known reference width. On the other hand, fixing a broadening obtained in the N_{23} measurements would be a rather small correction, on the order of the dependency of Γ on the background model (section 4.2.3), which is not fully worked out yet. Hence, for simplicity, the L_3 line is modelled as a pure Lorentzian in this thesis.

Table 4.3: Parameter settings for the Asimov simulation of the relation of Γ^2 and σ^2 in the L_3 integrated spectrum.

Parameter	Value
A (cps)	6000
E_0 (eV)	30472
Γ^2 (eV^2)	1.05^2
σ^2 (eV^2)	0 to 0.04
bg_0 (A)	0.5
t (s)	39
B_{ana} (G)	2.7
B_{source} (T)	2.52
B_{pinch} (T)	4.2
Energy range (eV)	30460-30480, 0.3 eV steps
Synchrotron	Off
Scattering	Off
Det. transmission	Off

To simulate the relation between Γ^2 and σ^2 in the relevant parameter range, Asimov integrated spectra were generated, for a Voigt L_3 with some reference $\Gamma_0^2 = 1.05^2$ eV^2 and various broadenings. Table 4.3 lists the simulation settings. The count rate and measurement time per retarding potential setpoint are scaled to typical ringwise values of L_3 measurements. A constant background was assumed. The Asimov spectra were then fitted with free Γ^2, and σ^2 fixed to 0. In this way, a relation $\Gamma^2(\sigma^2)$ was obtained, plotted in fig. 4.7. A linear fit yields the relation

$$\Gamma^2(\sigma^2) = 2.1 \cdot \sigma^2 + \Gamma_0^2. \tag{4.23}$$

Thus, if for example the physical Lorentzian width was 1.05 eV and there was an experimental Gaussian broadening of 0.1 eV, this would lead to an obtained fit value of $\Gamma = 1.06$ eV. This comparatively small deviation would require better than 1 % determination of the width in order to be sensitive to a 0.1 eV broadening. Systematic effects influencing Γ, like magnetic field uncertainty or the background slope, are expected to be larger than that.

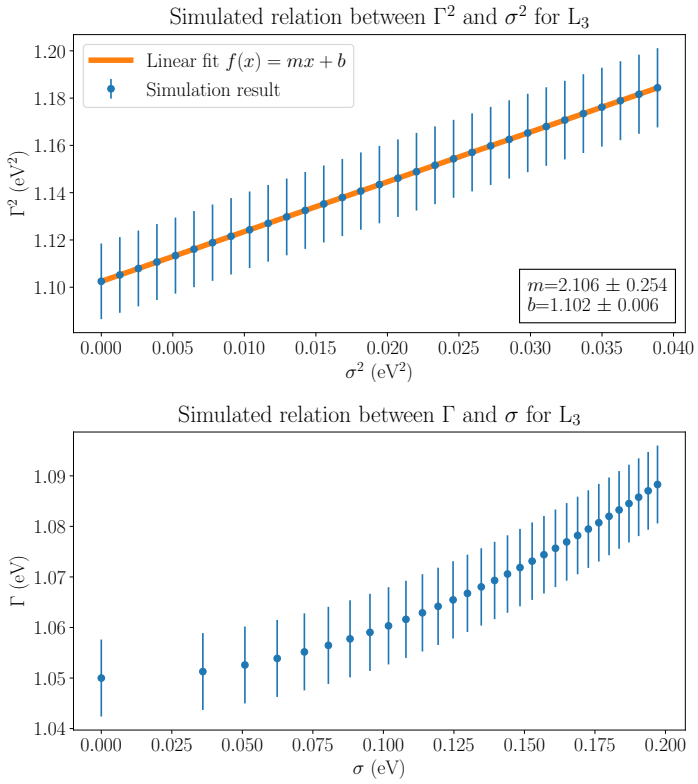

Figure 4.7: Top: Simulation result for the relation between Γ^2 and σ^2. The linear relationship was fitted with a slope of 2.1. Bottom: The resulting map when transforming to the unsquared values of Γ and σ.

The analysing plane magnetic field from the period summary input has a systematic uncertainty of 1 %. Using Asimov simulations, the influence of a 1 % deviating B_{ana} on the line position and width was estimated (for a reference width of 1.05 eV). The result is shown in table 4.4. In the larger field settings, the propagated uncertainties increase, since the 1 % deviation of B_{ana} becomes more severe. In 2.7 G, the uncertainty on Γ^2 was estimated to 1.5 %, which corresponds to a 90 meV broadening, using eq. (4.23). It is noteworthy that the systematic uncertainty on B_{ana} is expected to be a common shift for all pixels, which means that a difference in line position or width between pixels or rings should not arise from this.

Table 4.4: Estimated systematic uncertainty of L_3 line position and Lorentzian width resulting from 1 % deviation of B_{ana}, for different field settings.

	1.0 G	2.7 G	4.0 G	6.3 G
$u_{\text{sys}}(E_0)$ (meV)	4	11	16	25
$u_{\text{rel,sys}}(\Gamma^2)$ (%)	0.3	1.5	2.7	5.5

4.2.3 L_3 Background Slope

During the KNM3 measurement campaign, it was found that there is a background slope around the L_3 line, which, if not taken into account, influences the fitted line width significantly. This section investigates the influence and properties of the background slope.

4.2.3.1 Effect of not considered constant slope The simplest assumption of a non constant background is that it is a linear function of qU,

$$bg(qU) = S \cdot qU + bg_0, \tag{4.24}$$

where $S = \frac{\mathrm{d}bg}{\mathrm{d}qU} \neq 0$ is the constant slope parameter. When referring to the background slope being constant, it is meant that $\frac{\mathrm{d}^2bg}{\mathrm{d}qU^2} = 0$.

A simulation was performed, to determine the influence of a not considered constant background slope of different signs and magnitudes. The integrated spectrum model is extended by adding the background

$$bg(qU) = S \cdot (qU - 30\,472\,\mathrm{eV}) + bg_0. \tag{4.25}$$

The anchor point $bg(30\,472\,\mathrm{eV}) = bg_0$ was chosen close to the line position in order to reduce the correlation of S with bg_0.

A range of Asimov spectra of the integrated L_3 line with various S was drawn and fitted with a constant background in the model, to obtain the line width and position depending on the not considered constant slope. The chosen range of S is based on measurements presented in section 4.2.3.2. In table 4.5, the simulation settings are listed. Again, count rate and measurement time per voltage setting are scaled to typical (ringwise) values from measurements.

The top plot in fig. 4.8 shows the dependence of Γ^2 on the not considered constant slope. The relationship is linear. If $S < 0$ then Γ^2 becomes larger than the simulated input width $\Gamma_0^2 = 1.103\,\mathrm{eV}^2$ (red dashed line). If $S > 0$ then Γ^2 gets underestimated. The deviation will be significant if more statistics is assumed than in this simulation, so when combining the results of multiple measurements.

The line position shown in the bottom plot grows for positive slope and decreases for negative slope. However, the dependency is only on the sub-meV level, which is negligible considering other systematic effects like the FPD misalignment.

Table 4.5: Parameter settings for the Asimov simulation of the relation of Γ^2 and a constant background slope S in the L_3 integrated spectrum.

Parameter	Value
A (cps)	6000
E_0 (eV)	30472
Γ^2 (eV^2)	1.05^2
σ^2 (eV^2)	0
bg_0 (A)	0.5
S (A/eV)	$-1 \cdot 10^{-6}$ to $4 \cdot 10^{-4}$
t (s)	39
B_{ana} (G)	2.7
B_{source} (T)	2.52
B_{pinch} (T)	4.2
Energy range (eV)	30460-30480, 0.3 eV steps
Synchrotron	Off
Scattering	Off
Det. transmission	Off

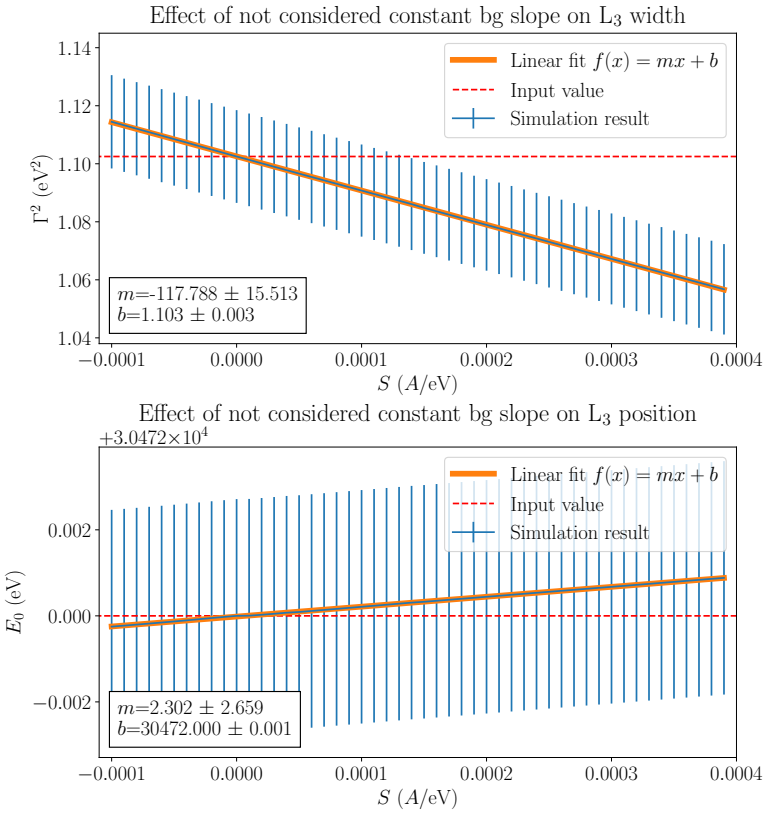

Figure 4.8: The simulated effect of a not considered constant background slope on the L_3 width (top) and position (bottom), fitted with linear functions (orange).

4.2.3.2 Background slope at different B_{ana} In the following, the analysis of three measurements with extended background region at three different analysing plane magnetic field settings is described. Table 4.6 lists the datasets and fit settings. A linear background model was used in the fit.

Table 4.6: The used datasets and fit settings for the analysis of the B_{ana} dependent background slope.

Name	L_3-c_1	L_3-c_2	L_3-c_3
Gas composition	Kr only	Kr only	Kr only
B_{ana}	6.3 G	4.0 G	2.7 G
Run numbers	63058-59	63060-61	63062-63
Campaign/time	KNM3/early July	KNM3/early July	KNM3/early July
RW potential (V)	0	0	0
Energy range (eV)	30460-30690	30460-30690	30460-30690
Add. Gauss. broad.	–	–	–
Synchrotron	On	On	On
Scatterings	1	1	1
Det. transmission	On	On	On
Background model	linear	linear	linear

Figure 4.9 shows the slope, background parameters and amplitude of the fits, averaged over runs with common B_{ana}. The parameters are plotted against the ring number, while the spacing of the points is according to the ring radius r in m (cf. table 4.1). As can be seen in the upper plot, the obtained background slope in 2.7 G is negative and similar to the other field settings for the inner two rings. Then it increases strongly with r, becoming positive at ring3.

In 6.3 G setting, the slope remains negative for all rings. A linear function was fitted to the datapoints (middle plot), giving

$$S(r) = r \cdot (1.8 \pm 0.8) \cdot 10^{-7} \, \frac{A/\text{eV}}{\text{mm}} - (6.9 \pm 0.2) \cdot 10^{-5} \; A/\text{eV}. \tag{4.26}$$

The 4.0 G setting is the intermediate case, though it is much closer to 6.3 G.

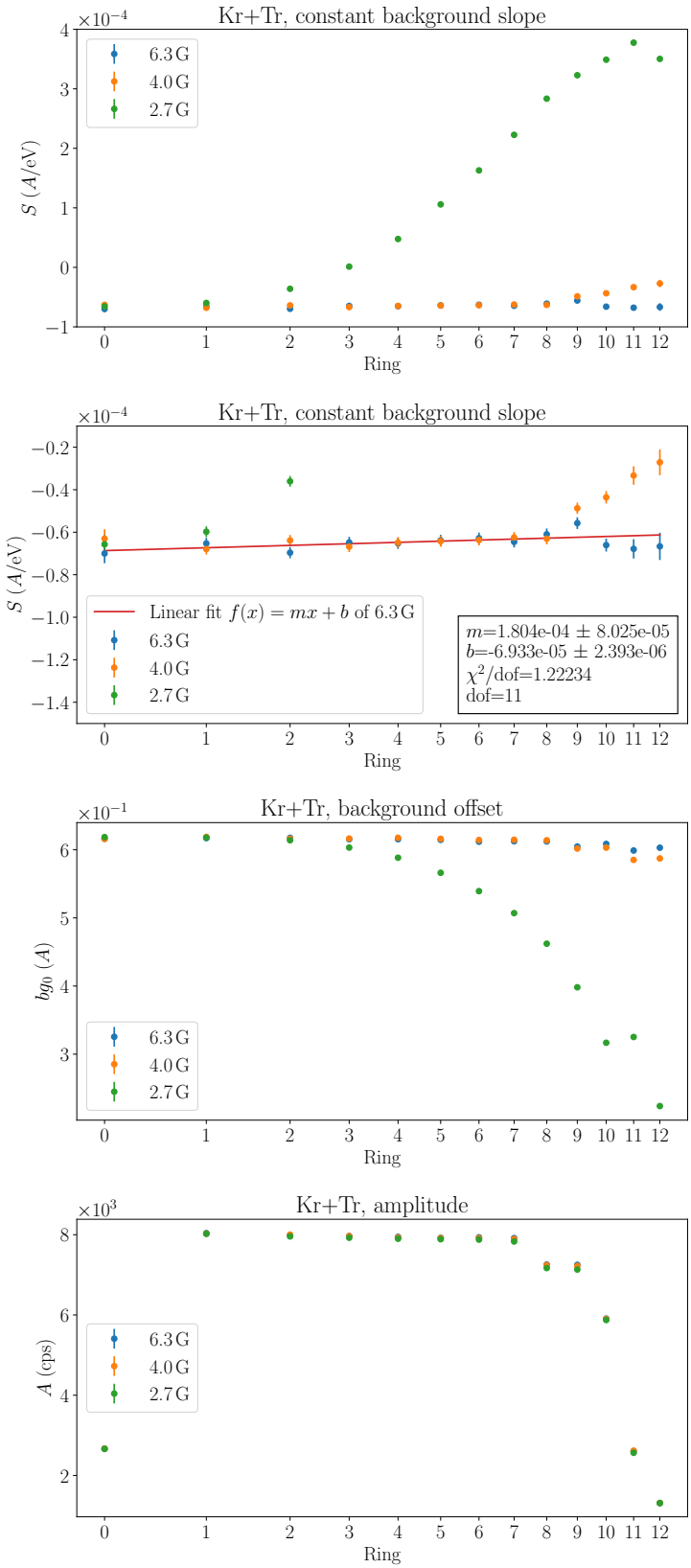

Figure 4.9: Fitted constant background slope of L_3 at three different B_{ana} settings. From top to bottom: a) Slope as function of the FPD ring. The abscissa ticks are spaced according to the ring radii. b) Zoomed in. A linear function was fitted to the 6.3 G datapoints. c) Background offset. bg_0 is heavily anticorrelated with A (correlation coefficient < -0.9). d) Line amplitude, mainly influenced by the number of pixels in the ring.

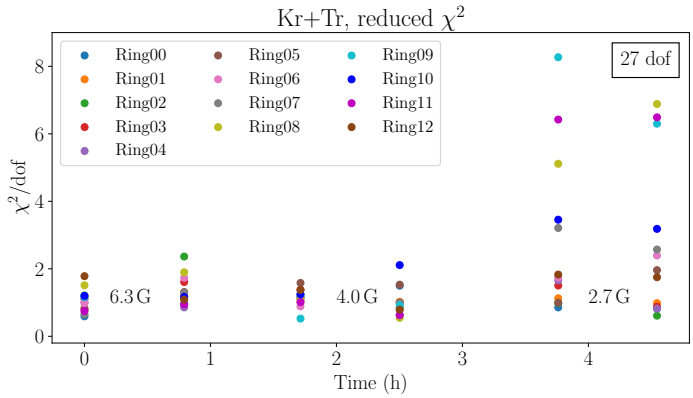

Figure 4.10: Reduced χ^2 of the Kr line fits as function of the time when the measurements were conducted.

The large positive slope for 2.7 G can be explained by non-adiabatic transport of electrons from higher Kr lines, like the M lines. Preliminary tracking simulations by F. Glück and E. Weiss [Glü20] show that the transmission probability of these electrons grows with the retarding potential, since the adiabaticity condition is violated for large surplus energies. This leads to a change of the spectrometer transmission properties, and a loss of electrons that are not guided to the detector. The effect is predicted to be much stronger for outer rings and smaller B_{ana}, and on a comparable order of magnitude as what is described in this chapter. A detailed comparison is pending. The background offset for 2.7 G decreases strongly with the radius, since the number of electrons at the anchor point is reduced by the increasingly stronger non-adiabaticity. Ring11 appears as an outlier.

For the inner rings and higher field settings however, the slope is largely produced by several other effects. Mainly the slope comes from the long Lorentzian tails of lower krypton lines, which is further discussed in section 4.2.3.3. Yet, there seems to be a small ring dependent component, visible both in the slope and the background offset. In 4 G, the non-adiabaticity might still be a factor, though probably a small one. Other considerable effects include energy and pixel dependent detector efficiency, i.e. that the detection efficiency might be lower for high energetic background electrons, depending on the FPD ring. This would also produce a negative background slope. Another effect is backscattering at the rear wall. Source electrons emitted towards the rear wall can be scattered back towards the spectrometer, losing some variable amount of energy. This would produce a negative slope as well.

By looking at the χ^2 distribution of the fits shown in fig. 4.10, it is apparent that

the model does not fit the outer rings in the 2.7 G setting. Figure 4.11 shows an examplary fit.

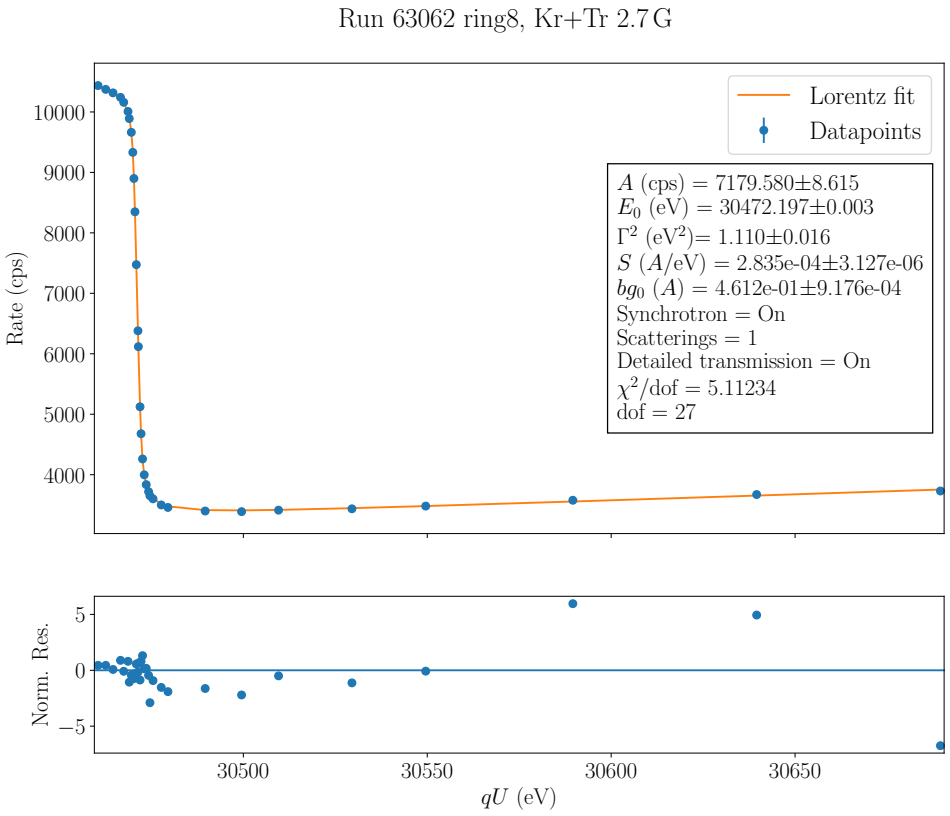

Figure 4.11: Fit result of run 63062 ring8 (Kr+Tr 2.7 G). The constant slope does not describe the background well, as shown by the residuals.

Clearly, the background points are not described well by the constant slope. So far, there is no clear prediction on how the non-adiabatic slope should look like. Therefore, it is also an open question what the systematic bias on the line width is, when assuming a constant background close to the line. One could fit some higher polynomial to the extended background region as a phenomenological approach, yet it is unclear whether this would give the correct background description around the L_3 position. To mitigate this issue, it is therefore preferable to measure the L_3 width in 6.3 G, where the slope is overall less significant and not strongly radial dependent. The downside of the 6.3 G setting however is the larger systematic uncertainty that comes from the 1 % uncertainty of B_{ana}. The resulting uncertainty on Γ^2 is estimated to be 5.5 % (cf. table 4.4) and makes

the determination of an absolute Gaussian broadening very hard. Yet, the magnetic field deviation should not produce a radial dependency of the width (apart from perhaps a small effect due to the FPD misalignment, similar to the line position shift shown in section 4.2.1), while the background slope in 2.7 G does, if not accounted for. Therefore, the 6.3 G setting should be usable for determining relative changes of the fitted line width between different measurements.

Still, for 6.3 G the full background description is not yet available. However, the next section considers additional effects that influence the background shape.

4.2.3.3 Background slope from other krypton lines While the large positive background slope observed in the 2.7 G setting is likely a result of non-adiabatic transport of high-energetic electrons, the origin of the negative background slope in 6.3 G is still not completely understood. The major contribution however comes from lower krypton lines, which produce a negative slope around L_3 due to their long Lorentzian tails. In the following, the slope produced by this is simulated and compared to measurements.

Using literature values, the rate contribution of various Kr main and shake lines to the energy region around L_3 was calculated (6.3 G, without scattering or detailed transmission, with synchrotron losses). The aim of the simulation is more of qualitative nature, since the precise Kr line parameters vary throughout literature. The parameters for the main lines are from table 3.1. All amplitudes are normalized to the L_3 amplitude. The shake lines are modelled as Lorentzians, despite actually having low-energy tails (see section 3.4). However, this should not heavily influence the qualitative simulation result. For the positions and amplitudes of the shake lines, the values in table 3.2 are used, with the exception of the L_3^{S3}. This line was measured in KNM3 and is fitted in section 4.2.3.4. Its simulation parameters are set to typical values from these fits, see table 4.7. The other L_3 shake lines are modelled with the same width as L_3^{S3}. The width of the L_2 shake lines is scaled down by the width ratio of the L_2 and L_3 main lines.

The K, L_1, M and N lines also have some shake probability [Vén+18]. However, since these shake lines are very far away from L_3 and have low intensity, they are neglected.

The simulation result is shown in fig. 4.12.

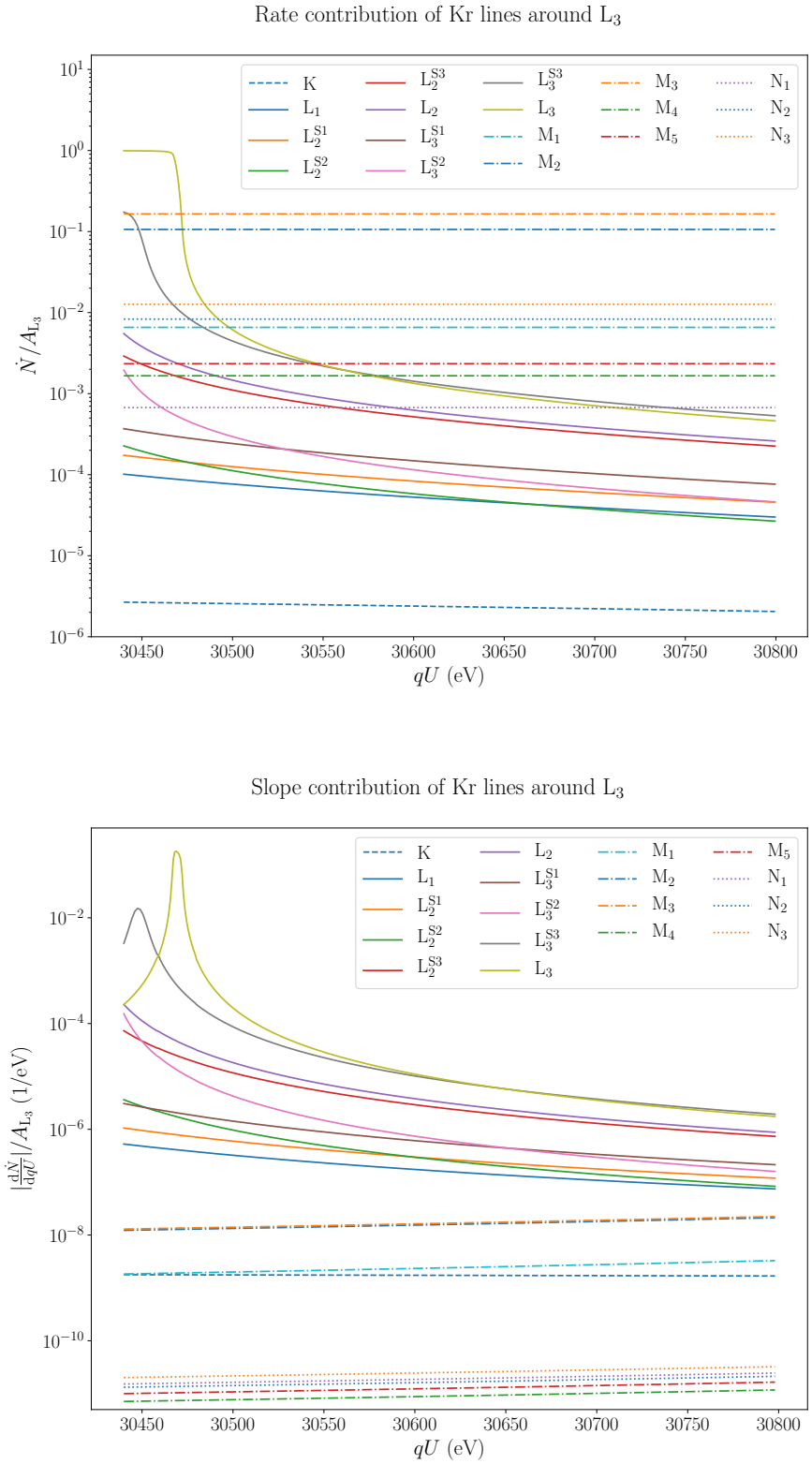

Figure 4.12: Top: The rate around L_3 generated by various Kr lines in logarithmic scale. The rate is normalized to the L_3 amplitude. Bottom: Absolute of the qU-derivative of the rate. The K, M, and N lines produce almost constant background, while L main and shake lines generate significant nonlinear background.

The higher M and N lines, as well as the lower K produce an almost constant background, since they are hundreds or thousands of eV away. The other L lines instead are rather close to L_3, and produce a significant slope. This is shown in the lower part of fig. 4.12, in which the absolute of the numeric derivative of the rate is plotted (the slope produced by the Kr line shape is always negative in an integrated spectrum). The L lines produce a slope on the order of -10^{-6} to -10^{-4} A_{L_3}/eV, but it is not constant. This means the background is a nonlinear function of qU. The main contribution comes from the L_3^{S3} shake line. The slope of the lines below L_3 approaches 0 with growing qU. It is vice versa with the higher M and N lines. Their contribution however is only 10^{-11} to 10^{-8} A_{L_3}/eV, producing almost constant background.

To check whether the extra Kr lines can produce the background behaviour observed in the data, a simulated Asimov spectrum was calculated by adding the contributions of the individual lines. In this way, a total spectrum of all considered Kr lines was generated. The simulation settings are given in table 4.7.

Table 4.7: Parameter settings for the Asimov simulation of L_3 with additional Kr lines, fitted with L_3 plus linear background.

Parameter	Value
A_{L_3} (cps)	13000
Kr main lines	K, L_1, L_2, L_3, M_1, M_2, M_3, M_4, M_5, N_1, N_2, N_3, values from table 3.1
Kr shake lines	L_2^{S1}, L_2^{S2}, L_2^{S2}, L_3^{S1}, L_3^{S2}: Positions and amplitudes from table 3.2, $\Gamma^2_{L_3^S} = 55\,\text{eV}^2$, $\Gamma^2_{L_2^S} = 38.8\,\text{eV}^2$, L_3^{S3}: $E_{L_3^{S3}} = 30\,451.2\,\text{eV}$, $A_{L_3^{S3}}/A_{L_3}$=0.2
σ^2 (eV^2)	0
bg	0 (produced by Kr lines)
t (s)	39
B_{ana} (G)	6.3
B_{source} (T)	2.52
B_{pinch} (T)	4.2
Energy range (eV)	30460–{30490, 30500, 30510, 30520, 30530, 30540, 30550, 30570, 30590, 30630}, MTD of L_3-d (cf. section 4.2.3.4)
Synchrotron	On
Scattering	Off
Det. transmission	Off

The resulting spectrum has the same MTD and overall count rate as real measurements of L_3 with extended background region. It was fitted with the L_3 line

only, plus a constant slope background model. While the slope produced by L_3 is already governed by the line itself, the other Kr lines produce some background, which the linear background model has to adjust to. Multiple fits were done with different upper fit ranges, adding voltage setpoints one by one to the fit. In fig. 4.13, the obtained constant slope and line width are plotted as function of upper fit range.

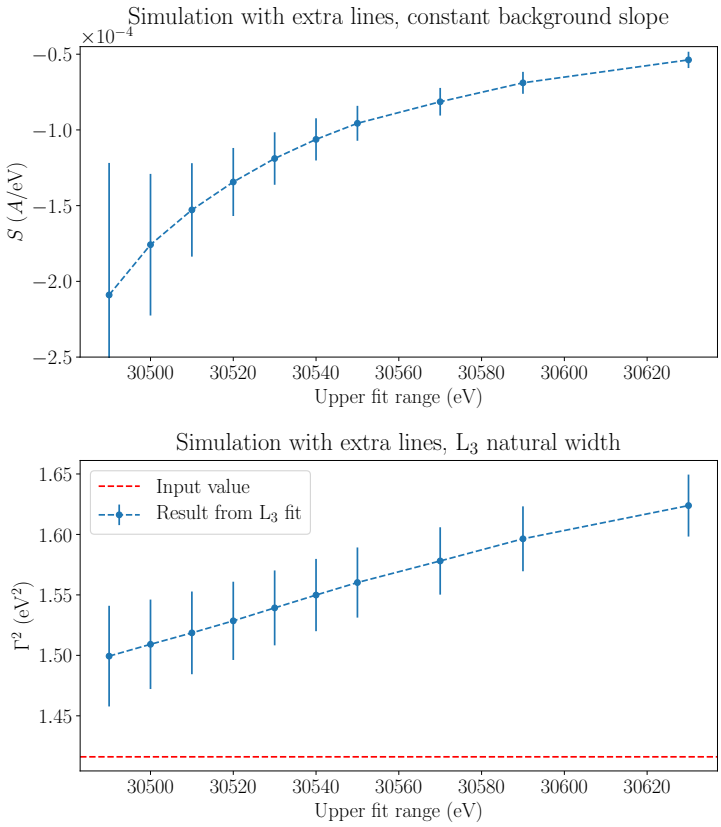

Figure 4.13: Fit result of the simulated L_3 spectrum with additional Kr lines, fitted with L_3 and a constant slope. Top: Linear slope as function of upper fit range. Bottom: Obtained L_3 width. The red line marks the simulation input width 1.19^2 eV^2.

S is negative and approaches 0 with larger fit range. This is because the slope of the nonlinear background produced by the Kr lines also approaches 0 with increasing qU, and the fitted constant slope is a secant through the nonlinear background of positive curvature (i.e. $c = \frac{\mathrm{d}^2 bg}{\mathrm{d}qU^2} > 0$). This can be seen in the residuals in fig. 4.14, which shows the fit at maximum upper fit range. The uncertainty of S decreases with the fit range, since the lever arm for the slope grows and the correlation with the line width gets reduced. For the highest upper

fit range 30 630 eV, the slope reaches $-5.4 \cdot 10^{-5} A/\text{eV}$. The lower plot in fig. 4.13 shows the behaviour of the obtained line width. It increases almost linearily with the fit range, while always being above the simulation input width (red line). This means that the background generated by the considered Kr lines will lead to an overestimation of the L_3 line width, if treated by a constant slope.

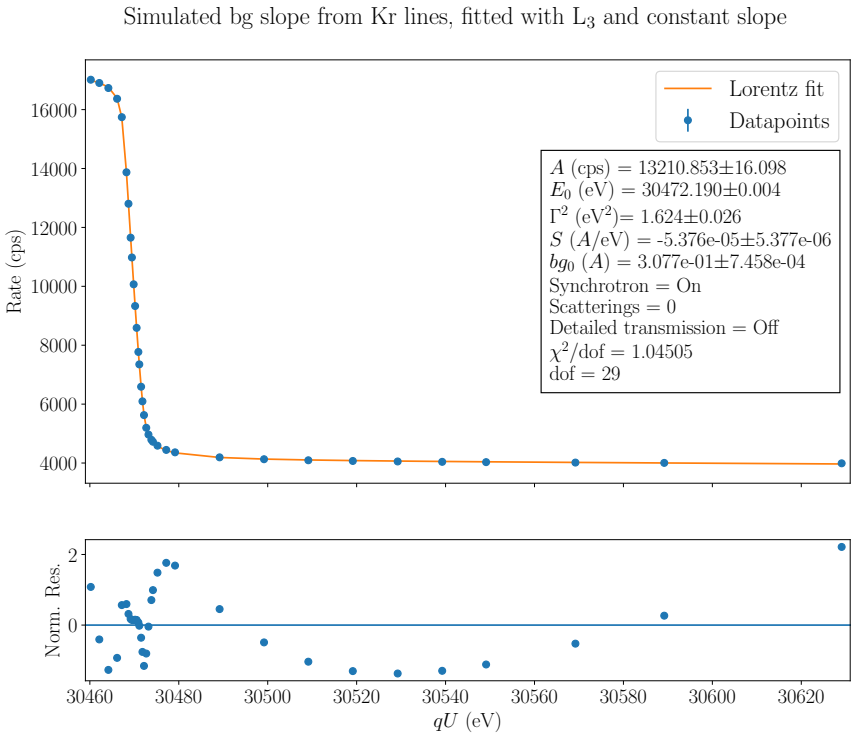

Figure 4.14: The simulated Asimov L_3 spectrum with additional Kr lines, fitted with L_3 and a constant slope. The residuals show that the background from the additional Kr lines is nonlinear.

As can be seen in fig. 4.14, the background offset bg_0 produced by the Kr lines in this simulation is 30 % of the amplitude. In section 4.2.3.4, measurements with the same settings show a larger bg_0, around 50 % of the amplitude. This is since the M and N shake lines are not simulated, and also due to the fact that electrons can backscatter at the rear wall. L_3 electrons that backscatter will not be counted due to the loss of energy, while M and N electrons have so much starting energy that they eventually can still pass the retarding potential. Therefore, the ratio of L_3 to higher energetic electrons is reduced and the background increases.

4.2.3.4 Applying different background models on measurement data

In the previous section, it was shown by a simulation that the various Kr conversion electron lines produce a negative background slope above the L_3 line. This slope is not constant, and if treated by a constant slope, the line width becomes overestimated, depending on the fit range. In this section, it is investigated whether the real measured slope can be described by these additional Kr lines, or whether there is some missing component. The analysed Kr only dataset, given in table 4.8, was taken in 6.3 G setting, so that the strong non-adiabaticity responsible for the positive background slope shown in section 4.2.3.2 is not of concern.

Table 4.8: Parameters and fit settings for the analysis of the L_3-d dataset for the negative background slope investigation.

Name	L_3-d
Gas composition	Kr only
B_{ana}	6.3 G
Run numbers	64870–64893
Campaign/time	KNM3/late August
RW potential (V)	0
Energy range (eV)	30445/30460–30630
Add. Gauss. broad.	–
Synchrotron	On
Scattering	Off
Det. transmission	Off

The data were fitted with four different background models.

a) Constant slope

b) Additional Kr lines

c) Additional Kr lines + constant slope

d) Additional Kr lines + quadratic background model

The quadratic background is given by

$$bg(qU) = Q(qU - 30\,472\,\text{eV})^2 + S(qU - 30\,472\,\text{eV}) + bg_0, \tag{4.27}$$

with some coefficient Q of the quadratic term. For models b)-d), the fit range is increased to include the L_3^{S3} line, which was also measured in this dataset. When fitting L_3 with additional Kr lines, these are modelled as Lorentzians L shifted by some ΔE_i and scaled by an amplitude ratio R_i to the L_3 line. ΔE_i and R_i

are fit parameters, besides some Lorentzian width Γ_{i}^2. The differential spectrum then reads

$$D(E) = A \cdot L_{\mathrm{L_3}}(E_0, \Gamma^2) + \sum_{\mathrm{i}} AR_{\mathrm{i}} \cdot L_{\mathrm{i}}(E_0 + \Delta E_{\mathrm{i}}, \Gamma_{\mathrm{i}}^2). \tag{4.28}$$

While the $\mathrm{L_3^{S3}}$ parameters are free, the parameters of the other additional Kr lines are fixed to the simulation parameters used in section 4.2.3.3. Only the L main and shake lines are included in the fit, since the others do not produce a significant slope. It should be noted again that the description of the additional lines is imperfect, as the line parameters are not known with high precision, especially for the shake lines.

First, the constant slope model is compared with the simulation (cf. section 4.2.3.3). To do so, the data were fitted with different fit ranges to see the dependency of S and Γ^2 on the fit range. The result is shown in fig. 4.15. The values are averaged over all runs and rings.

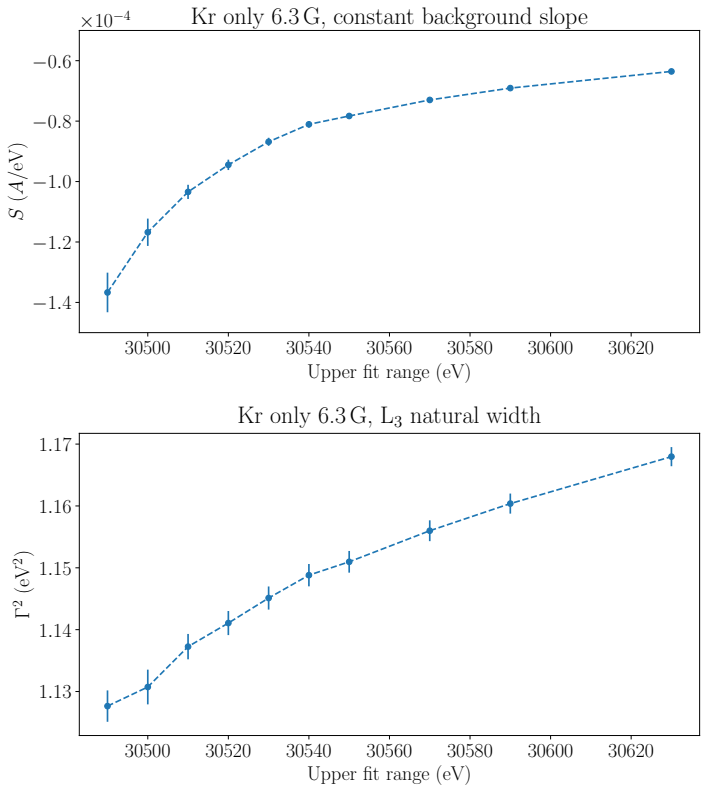

Figure 4.15: The $\mathrm{L_3}$-d dataset fitted with a constant slope and different upper fit ranges. The top plot shows the slope parameter S, and the bottom plot shows the squared line width, both averaged over all runs and rings.

The constant slope parameter as well as the line width show a similar behaviour as in the simulation (cf. section 4.13), yet their dependency on the upper fit range is less strong. This indicates that the actual slope is closer to a linear behaviour than the one produced by the additional Kr lines. Also, the magnitude of S for the largest fit range ($S = (-6.35 \pm 0.04) \cdot 10^{-5}\ A/\mathrm{eV}$) is larger than the simulated $S = -5.4 \cdot 10^{-5} A/\mathrm{eV}$.

To decide how well the different models a)-d) describe the background, it is checked whether prominent structures in the fit residuals are present. To cancel out fluctuations, the residuals of each background model are averaged ringwise over the 24 runs of the dataset. An alternative approach is to stack the runs before fitting, by averaging the respective voltage setpoints and rates. But since the voltage setpoints can vary by 100 meV from run to run, this would introduce some smearing of the spectrum. Yet, to check for noticable residual structures, stacking the residuals is a reasonable approach. The result for ring3 is shown in fig. 4.16. The other rings show similar behaviour.

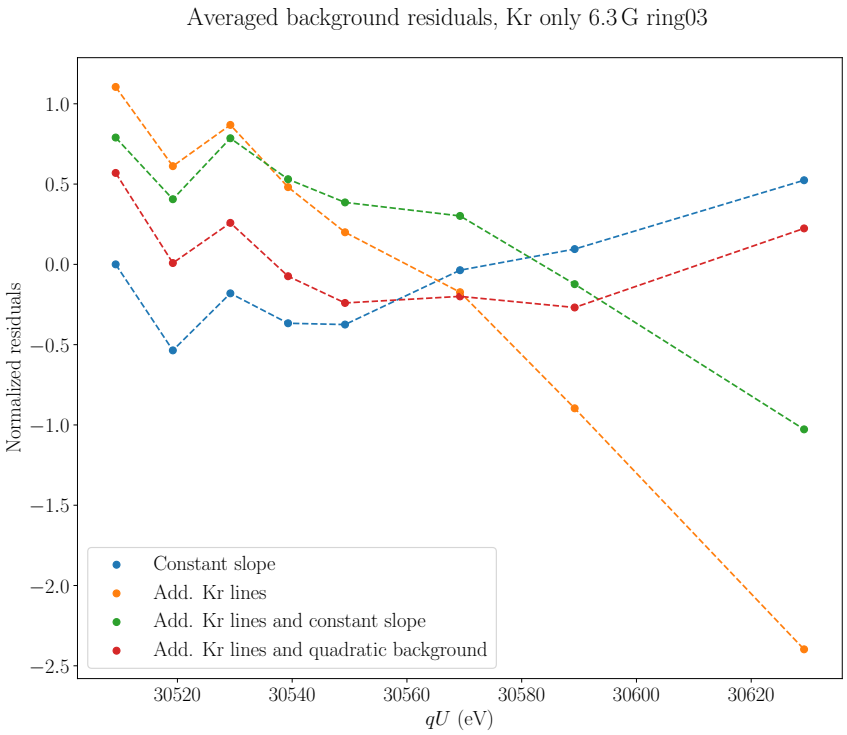

Figure 4.16: Background residuals for different background models of the L_3 line. The residuals are averaged over all runs of the dataset. Shown is the result for ring3.

The fit with linear background (blue) shows an increasing structure, overall resembling the shape of the Kr line simulation (fig. 4.14), while being much less pronounced. When having the additional Kr lines and no slope in the model (orange), the residuals drop strongly, revealing a missing slope component. When fitting additionally with a constant slope, this structure becomes less prominent, though still significant. Having additional Kr lines and a quadratic background (red) reduces the resiudals even more, while leaving some parabola-like structure. One could go to higher polynomials to define the missing slope increasingly well, yet without some physical expectation of the background shape, it cannot be motivated to extrapolate it into the region of L_3 itself.

However, it can be concluded that there is a negative component in the background slope in addition to the extra Kr lines. It has negative curvature that cancels some of the positive curvature of the slope produced by the extra Kr lines, making the background comparably well described by a linear function.

Since the background is overall proportional to the Kr line intensity, and the additional background in KATRIN is on the order of a few 100 mcps (all pixels combined), the missing slope has to be produced by Kr electrons. As already mentioned in section 4.2.3.2, possible origins include backscattering, energy dependent detection efficiency, and perhaps still some small non-adiabatic effects. Some modification of the slope will also come from corrected parameters of the additional Kr lines. Though if the influence of those lines is actually stronger than in the simulation (which would explain the overall larger magnitude of the measured slope), the background would get an even more negative curvature, while the measured background shape appears to have a less negative curvature than simulated.

The line width with background model d) is overall smaller than with model a), as shown in fig. 4.17 (model a)) and fig. 4.18 (model d)). In both cases, the width is less ring dependent than what was observed in 2.7 G (see fig. 4.5), which is consistent with the large positive slope in that setting.

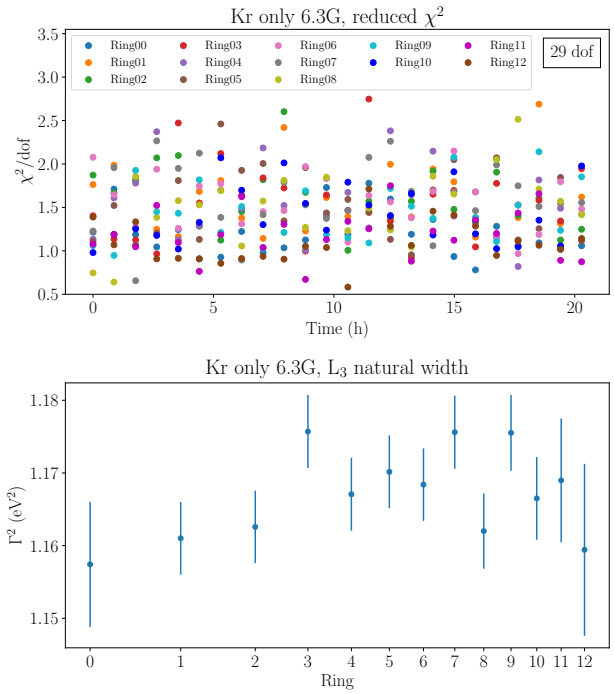

Figure 4.17: Fit result of L_3-d when fitted with a linear background. Top: Reduced χ^2 as function of measurement date of the respective run. Bottom: Ringwise line width averaged over all runs.

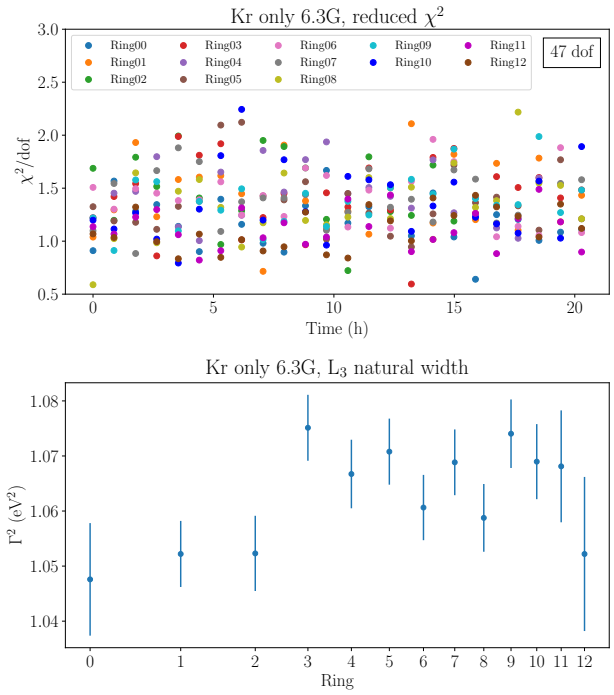

Figure 4.18: Fit result of L_3-d when fitted with additional Kr lines and a quadratic background model. Top: Reduced χ^2 as function of measurement date of the respective run. Bottom: Ringwise line width averaged over all runs.

The goodness of the fits of this dataset is rather poor. The reason for this however is less in the background than in the line region, which dominates the χ^2 due to the multitude of datapoints. The rate in these measurements is much higher than in previously shown datasets, due to the installation of a stronger Kr source in late August 2020. Therefore, some structures in the line residuals emerge, pointing to systematics (see fig. 4.19 and fig. 4.20). The residual structures do not originate from some Gaussian broadening that is treated as a Lorentzian width. When fixing a broadening of 50 or 100 meV, the residuals are almost unaltered while the line width behaves similar to the relation simulated in section 4.2.2. Also the background model, while changing Γ^2 significantly, does not alter some prominent residual structures.

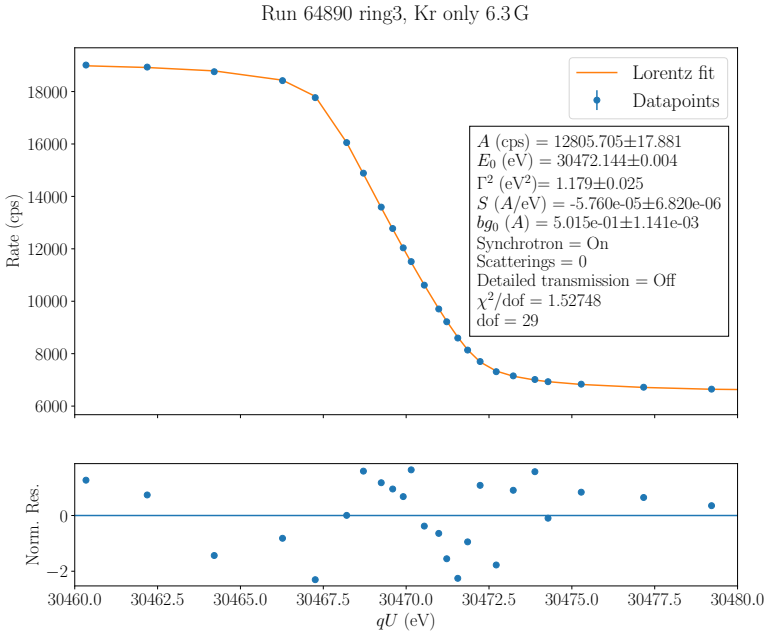

Figure 4.19: Fit of run 64890 ring3 with linear background. The upper fit range is 30 630 eV, yet only the line region is shown to display residual structures.

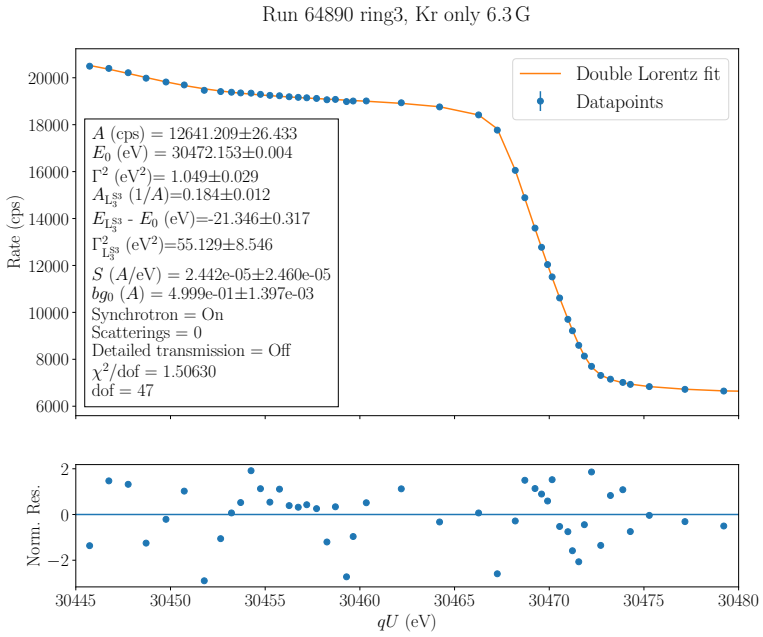

Figure 4.20: Fit of run 64890 ring3 with additional Kr lines and quadratic background. The upper fit range is 30 630 eV, yet only the line region is shown to display residual structures. The L_3^{S3} line is included in the fit as well.

Possible effects include errors in the magnetic fields, which are more poignant in 6.3 G, as well as scattering of electrons on gas impurities. While in Kr only mode the tritium is largely removed, some impurities from outgassing, containing for instance O_2 and N_2, are present in the beam tube due to the specific source operation mode. These impurities may produce peaks in the energy loss spectrum close to the L_3 line position [Rod20].

4.2.3.5 Conclusion on the background slope It was shown that there is a nonlinear background slope above the L_3 line, which, when not taken into account properly, distorts the fitted line width. For low analysing plane magnetic fields, like the 2.7 G setting, the slope is relatively large, positive and strongly radial dependent. It likely originates from non-adiabatic transport of electrons from higher Kr lines. In the 6.3 G setting, this effect is largely suppressed and a relatively small negative nonlinear slope remains, with comparably little radial dependence. It consists mainly from the slope generated by lower Kr lines, foremost the L_3^{S3} shake line. Still, there is some missing component whose origin and description should be investigated in the future.

4.3 Analysis of the Krypton N_{23} Lines

The measurement and analysis treatment of the N_{23} doublet differs in a few points from the L_3 line. The fit model, consisting of two pure Gaussians in the differential spectrum, is described in section 4.3.1. The measurements were mainly performed in a voltage ramping mode. This is discussed in section 4.3.2. In section 4.3.3, the influence of a possible non-vanishing natural line width is estimated. The measurement analysis results are presented in section 4.3.4.

4.3.1 Fit Model

Since the N lines are expected to have almost vanishing natural line width, they are treated as pure Gaussians with a common broadening. The differential spectrum is modelled as the sum of two Gaussians

$$D(E) = A_2 \cdot G(E_2, \sigma^2) + R_{32} A_2 \cdot G(E_2 + \Delta E_{32}, \sigma^2), \tag{4.29}$$

with fit parameters

- A_2 – amplitude of N_2
- E_2 – position of N_2
- σ^2 – common broadening of both lines
- R_{32} – amplitude ratio A_3/A_2
- ΔE_{32} – position difference $E_3 - E_2$.

The line position difference is constrained by a pullterm to $\Delta E_{32}^{\text{lit}} \pm u(\Delta E_{32}^{\text{lit}}) = (0.670 \pm 0.014)\,\text{eV}$, known from optical spectroscopy [Vén+18].

As for L_3, synchotron losses and, in case of Kr+Tr measurements, detailed transmission are taken into account. The contribution of tritium scattering to the spectrum however can be neglected, since the scan region reaches only down to 6 eV below N_{23}. The background model is a constant since there are no higher krypton lines whose electrons could be subject to non-adiabatic transport, and the lower lines are either very weak or far away and should not produce a significant background slope.

For measurements in the ramping mode, all runs within a given dataset are stacked, as described in section 4.3.2. The fits are then performed on individual rings of these stacked data. The amplitude ratio and line position difference are

physical constants, which should be the same for all fits. They are thus taken as common parameters for all rings in a combined fit.

The intensity of the N_{23} doublet is two orders of magnitude smaller than the L_3 line, and the background is on the order of a few hundred mcps, due to the absent of higher lines. To account for the low count rate, a Poisson likelihood

$$\mathcal{L} = \prod_{\mathrm{i}} \frac{e^{-\mu_\mathrm{i}} \mu_\mathrm{i}^{n_\mathrm{i}}}{n_\mathrm{i}!} \tag{4.30}$$

is used for the fit minimization. Here n_i is the measurement counts of datapoint i, and μ_i is the model counts (which can be non-integer). Following the maximum likelihood method, the quantity to be minimized is then

$$-\ln \mathcal{L} + \frac{1}{2} \left(\frac{\Delta E_{32} - \Delta E_{32}^{\mathrm{lit}}}{u(\Delta E_{32}^{\mathrm{lit}})} \right)^2, \tag{4.31}$$

where

$$-\ln \mathcal{L} = \sum_{\mathrm{i}} (\mu_\mathrm{i} - n_\mathrm{i} \ln \mu_\mathrm{i} + \ln n_\mathrm{i}!) \tag{4.32}$$

is the negative log likelihood. In a combined fit the total negative log likelihood function is given by the sum of individual functions for each ring k, sharing R_{32} and ΔE_{32}, while having all other parameters individually:

$$(-\ln \mathcal{L})_{\mathrm{tot}} = \sum_{\mathrm{k}} (-\ln \mathcal{L})_\mathrm{k} (R_{32}, \Delta E_{32}, E_{2,\mathrm{k}}, A_{2,\mathrm{k}}, \sigma_\mathrm{k}^2, bg_{0,\mathrm{k}}). \tag{4.33}$$

To estimate the goodness of fit, the sum D of squared deviance residuals d_i is used,

$$D = \sum_{\mathrm{i}} d_\mathrm{i}^2 = \sum_{\mathrm{i}} \left(\sqrt{2(n_\mathrm{i} \ln \frac{n_\mathrm{i}}{\mu_\mathrm{i}} - n_\mathrm{i} + \mu_\mathrm{i})} \cdot \mathrm{sgn}(\mu_\mathrm{i} - n_\mathrm{i}) \right)^2, \tag{4.34}$$

which is approximately equal to $-2 \ln \mathcal{L}$ when using the Stirling formula $\ln n_\mathrm{i}! \approx n_\mathrm{i} \ln n_\mathrm{i} - n_\mathrm{i}$.

When the overall counts are large, the Poisson distribution becomes Gaussian and the total deviance should become equivalent to a χ^2. In the following, it is shown by a Monte Carlo study that for the N_{23} analysis the total deviance D can be used analogously to a χ^2 to estimate the goodness of fit.

A spectrum with typical count rate and measurement time of a stacked ramping dataset (single ring) is simulated. The simulation settings are displayed in table 4.9. Then, 1000 Monte Carlo samples are drawn by feeding the simulated

Table 4.9: Parameter settings for the Monte Carlo simulation of the distribtion of total deviance D for N_{23}.

Parameter	Value
A_2 (cps)	120
E_2 (eV)	32136.5
σ^2 (eV^2)	$6 \cdot 10^{-3}$
R_{32}	1.6 (fixed in fit)
ΔE_{32}	0.67 (fixed in fit)
bg_0 (cps)	0.07
t (s)	72
B_{ana} (G)	2.7
B_{source} (T)	2.52
B_{pinch} (T)	4.2
Energy range (eV)	32132-32140, 0.03 eV steps
Synchrotron	Off
Scattering	Off
Det. transmission	Off
No. of MC samples	1000

counts into a Poisson random number generator. Each MC spectrum is then fitted. The distribution of D/dof of the fits is compared to a χ^2/dof distribution for the given number of 263 degrees of freedom. The distributions shown in fig. 4.21 are in good agreement, while the D/dof distribution of the 1000 samples has a mean of 1.011 and a width of 0.086, which deviates by 1 % from the χ^2/dof width $\sqrt{2/\text{dof}} = 0.087$. Thus, D/dof can be used as an estimate of goodness of fit similar to a χ^2/dof.

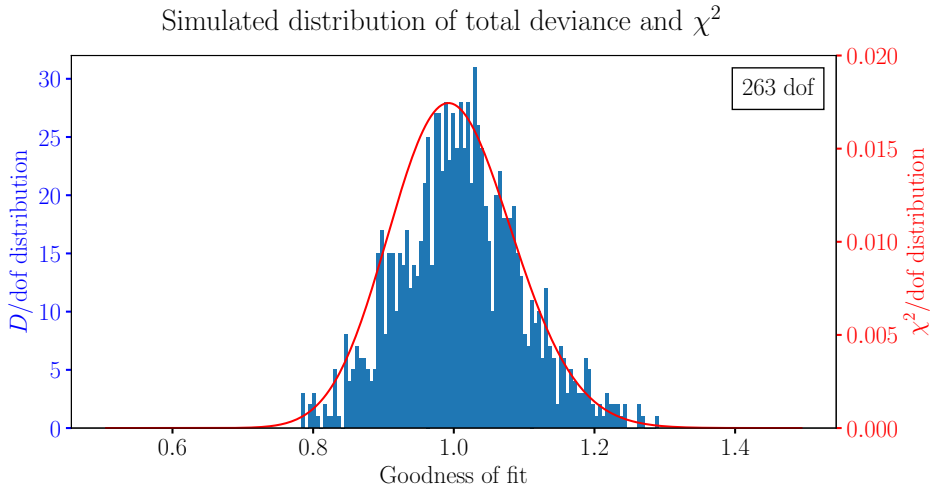

Figure 4.21: The distribution of total deviance per dof from fitting 1000 Monte Carlo samples of N_{23} with 263 dof (blue), compared with the reduced χ^2 distribution for 263 dof.

4.3.2 Ramping Mode

Because of the low intensity of the N lines, by far most measurements in KNM3 were done in a voltage ramping mode. Hereby, the retarding potential is changed continuosly by ramping the voltage on the IE system in the main spectrometer.

In general, the retarding potential in the analysing plane is controlled by the spectrometer vessel potential plus the IE common potential, which is usually set to a fixed $-200\,\mathrm{V}$ with respect to the vessel potential. In the usual MTD mode, the vessel potential is changed in discrete steps, while IE common follows with a constant $-200\,\mathrm{V}$ offset. This goes along with some deadtime on the order of 15 s between steps, which is required to set the vessel potential. In the ramping mode, this time is saved, which allows to fully use the mearument time and gather as much statistics as possible. On the downside, systematic effects from the potential depression of the IE-common potential might occur. The retarding potential is inhomogenous throughout the analysing plane, which is simulated and taken into account in the period summaries. The depression of the potential however depends on the difference between vessel and IE common potential. When changing IE common while keeping the vessel potential fixed, the actual potential distribution throughout the plane may differ from the period summary simulation (probably on the order of 1 %), in effect leading to a smearing of the spectrum. This is yet to be investigated in detail and is not taken into account in the analysis.

The retarding potential is changed with a ramping speed of $0.03\,\mathrm{V/s}$. The result of the measurement is a time series of counts vs qU, which is then binned into 1 s or 0.03 eV bins during run summary generation. The bias from the binning is estimated to be on the order of a few meV on line position and $< 1\,\%$ on σ^2, which is within statistical uncertainties for the measurements analysed in the following.

A ramping run has a length of only 3-5 min and does only collect few counts. To increase statistics and hereby numeric stability in a fit with the full model, many runs are stacked. This is done by summing up the data of the runs and rebin them again to 0.03 eV bins, centered around the mean voltage within the bin and containing the sum of the counts. Due to small variations in the ramping speed, the number of runs that contribute in some particular bin can also vary to small extend. This is taken into account by scaling the model counts with the total measurement time that went into the bin. The stacking introduces additional smearing to the spectrum. Using the variance of a uniform distribution, the ad-

ditional broadening can be estimated to $\sigma^2_{\text{stacking}} = (0.03\,\text{eV})^2/12 = 7.5 \cdot 10^{-5}\,\text{eV}^2$, which is an 1 % effect.

Before stacking the runs of a dataset, it is checked whether there is some systematic drift in the line positions of the individual runs, which could smear out the stacked spectrum significantly. This is done by fitting every run individually, yet due to low statistics the model is then simplified by fixing the amplitude ratio to literature values and omitting detailed tranmission. The simplified model should however still allow to check for line position drifts.

4.3.3 Influence of Natural Line Width of N_{23}

The upper limit on the natural line width of N_2 and N_3 in the literature is $\Gamma \leq 0.03\,\text{eV}$ (cf. table 3.1). The width is given by the inverse life time of the shell vacancy and thus depends on the recombination rate of the ionised Kr atom [Alt+20]. In the analysis for this thesis however, N_{23} are treated as pure Gaussians, because even a non-vanishing Lorentzian width can expected to be small compared to the experimental broadening, and has therefore only little influence on the fit result. There is a lower bound for the broadening coming from the Doppler effect, which produces $\sigma_{\text{D}} = 54.6\,\text{meV}$ (see section 4.1.1).

To estimate the upper correction bound from a non-vanishing Lorentzian width, an Asimov simulation was performed, using the upper limit for the natural width $\Gamma_{\text{max}} = 30\,\text{meV}$ and the minimal expected broadening $\sigma_{\text{Dop}} = 54.6\,\text{meV}$. In this configuration the influence of the Lorentzian is maximal. An integrated double-Voigt spectrum with common Γ_{max} for both N_2 and N_3 and a common Gaussian broadening of σ_{Dop} was generated. This spectrum was then fitted with the integrated spectrum of two pure Gaussians. The simulation settings are listed in table 4.10. The fit result is plotted in fig. 4.22. The residuals show characteristic structures like the long Lorentzian tail, yet the deviation from 0 is small compared to expected statistical fluctuations. The result for the squared broadening $\sigma^2_{\text{Fit}} = 3.8 \cdot 10^{-3}\,\text{eV}^2$ agrees with squared addition of σ_{D} and Γ_{max}. The increase in linear broadening is only $\sigma_{\text{Fit}} - \sigma_{\text{D}} = 7\,\text{meV}$. This can be taken as an upper limit for the overestimation of the Gaussian broadening due to non-vanishing natural width, when modelling N_{23} as pure Gaussians.

Table 4.10: Parameter settings for the Asimov simulation of the influence of non-vanishing natural line width of N_{23}.

Parameter	Value
A_2 (cps)	120
E_2 (eV)	32136.5
σ^2 (eV^2)	0.0546^2
Γ_2^2 (eV^2)	0.03^2
Γ_3^2 (eV^2)	0.03^2
R_{32}	1.6
ΔE_{32}	0.67
bg_0 (cps)	0.07
t (s)	72
B_{ana} (G)	2.7
B_{source} (T)	2.52
B_{pinch} (T)	4.2
Energy range (eV)	32132-32140, 0.03 eV steps
Synchrotron	On
Scattering	Off
Det. transmission	Off

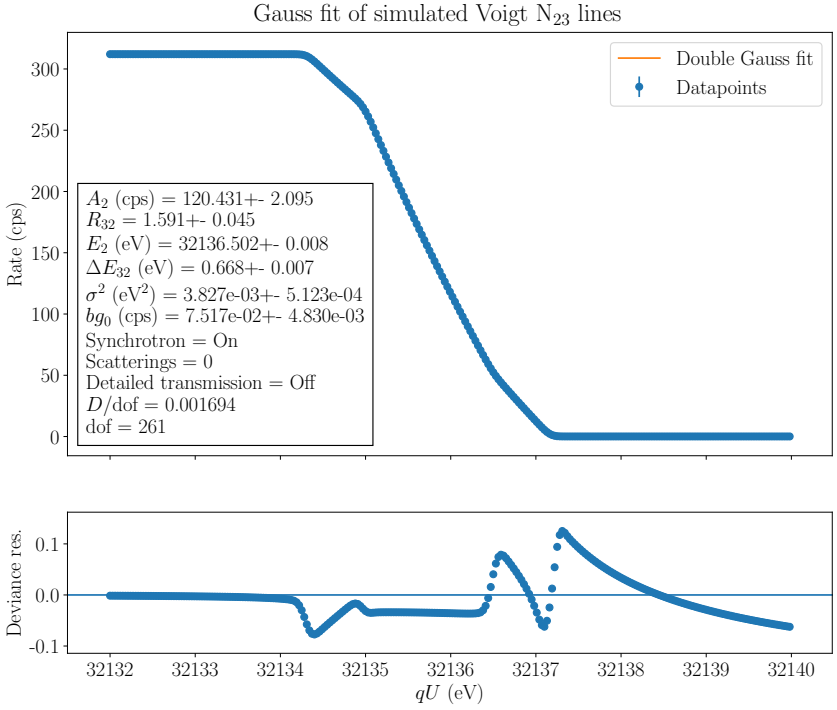

Figure 4.22: The Asimov data of N_{23} with common natural line width of 30 meV and Doppler broadening 54.6 meV, fitted with pure Gaussians.

4.3.4 N_{23} Analysis Results

In the following, the analysis of five datasets is presented, in order to compare the N_{23} parameters for different gas compositions and analysing plane magnetic fields. Also a comparison of an MTD mode and ramping mode result is given. The datasets are listed in table 4.11. As stated earlier, the ramping runs are stacked within the dataset. Before stacking, in order to check for line position stability, each run is fitted individually with a simplified model, having the amplitude ratio fixed to the literature value 1.523 (cf. table 3.1), and without detailed transmission. As an example, the line positions for N_{23}-d are plotted in fig. 4.23.

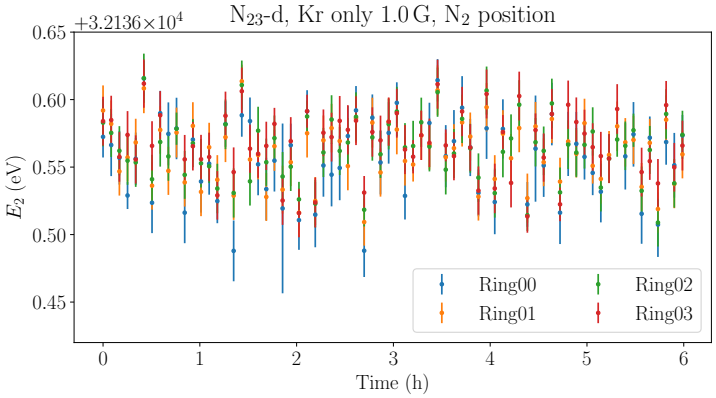

Figure 4.23: The line position distribution of N_{23}-d. For every run, rings 0 to 3 were fitted individually with a simplified model.

Overall, there is no systematic behaviour visible, the positions fluctuate within their uncertainty. Thus, they are assumed to not introduce a significant smearing when stacked. The stacked spectrum is then fitted with R_{32} and ΔE_{32} as common parameters for all rings. This procedure is followed for all ramping datasets. For the 1 G measurement N_{23}-e, only ring0 to ring3 are fitted. In the 1 G setting, the magnetic field lines are guiding the electrons towards the vessel walls, so that the outer FPD rings are not hit by the flux tube and cannot be used. For the MTD mode dataset N_{23}-b, the effective measurement time per run is 35 min (38 s per point), so that every run has sufficient statistics to be fitted on its own with the full model. Later on, the results of each MTD run are averaged out. In figures 4.24, 4.25, and 4.26, examplary fits for all datasets are shown. While the fits use a Poisson likelihood acting on the stacked counts N_{tot}, for illustration purposes the rate $N_{\mathrm{i}}^{\mathrm{tot}}/t_{\mathrm{i}}^{\mathrm{tot}}$ is plotted, with errorbars given by $\sqrt{N_{\mathrm{i}}^{\mathrm{tot}}}/t_{\mathrm{i}}^{\mathrm{tot}}$ and total measurement time $t_{\mathrm{i}}^{\mathrm{tot}}$ that went into bin i.

Table 4.11: Used datasets and fit settings for the N_{23} analysis.

	N_{23}-a	N_{23}-b	N_{23}-c	N_{23}-d	N_{23}-e
Gas comp.	Kr only	Kr only	Kr+Tr	Kr+Tr	Kr only
Mode	Ramp	MTD	Ramp	Ramp	Ramp
B_{ana}	2.7 G	2.7 G	2.7 G	4 G	1 G
Run numbers	61370-401, 407-438	61439-40	62519-550, 555-560, 588-617, 620-621	63094-101, 105-132	64798-869
Campaign/ time	KNM3/late May	KNM3/late May	KNM3/mid-June	KNM3/early July	KNM3/late August
RW pot. (V)	0	0	0	0	0
Energy range (eV)	32133-9	32130-40	32133-9	32131-40	32132-41
Synchrotron	On	On	On	On	On
Scatterings	0	0	0	0	0
Det. trans.	Off	Off	On	On	Off

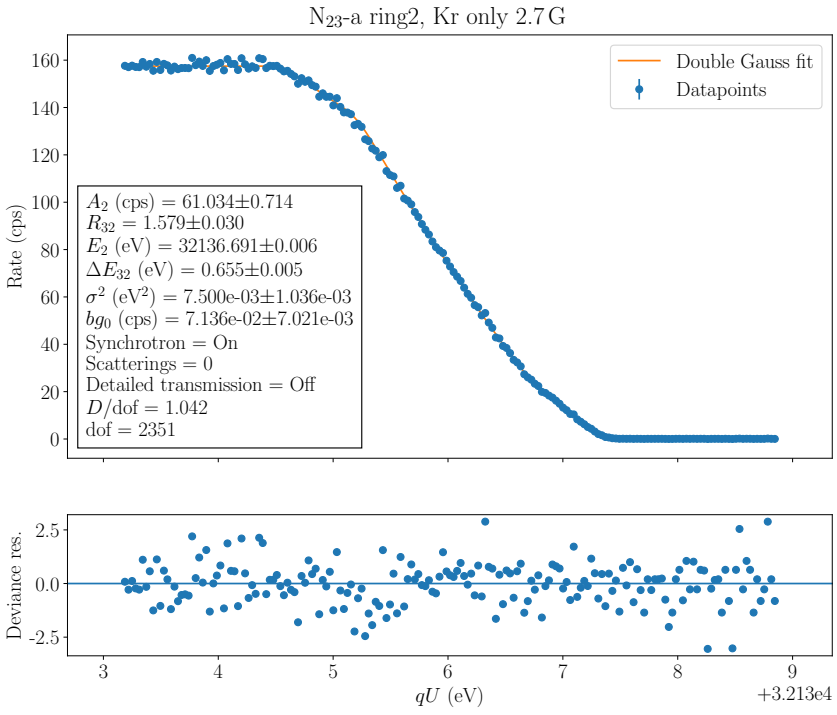

Figure 4.24: Example ring of the ring-combined fit of the stacked runs of N_{23}-a. Amplitude ratio and line position difference are common parameters for all rings. The total deviance D and degrees of freedom refer to the total fit of all rings combined.

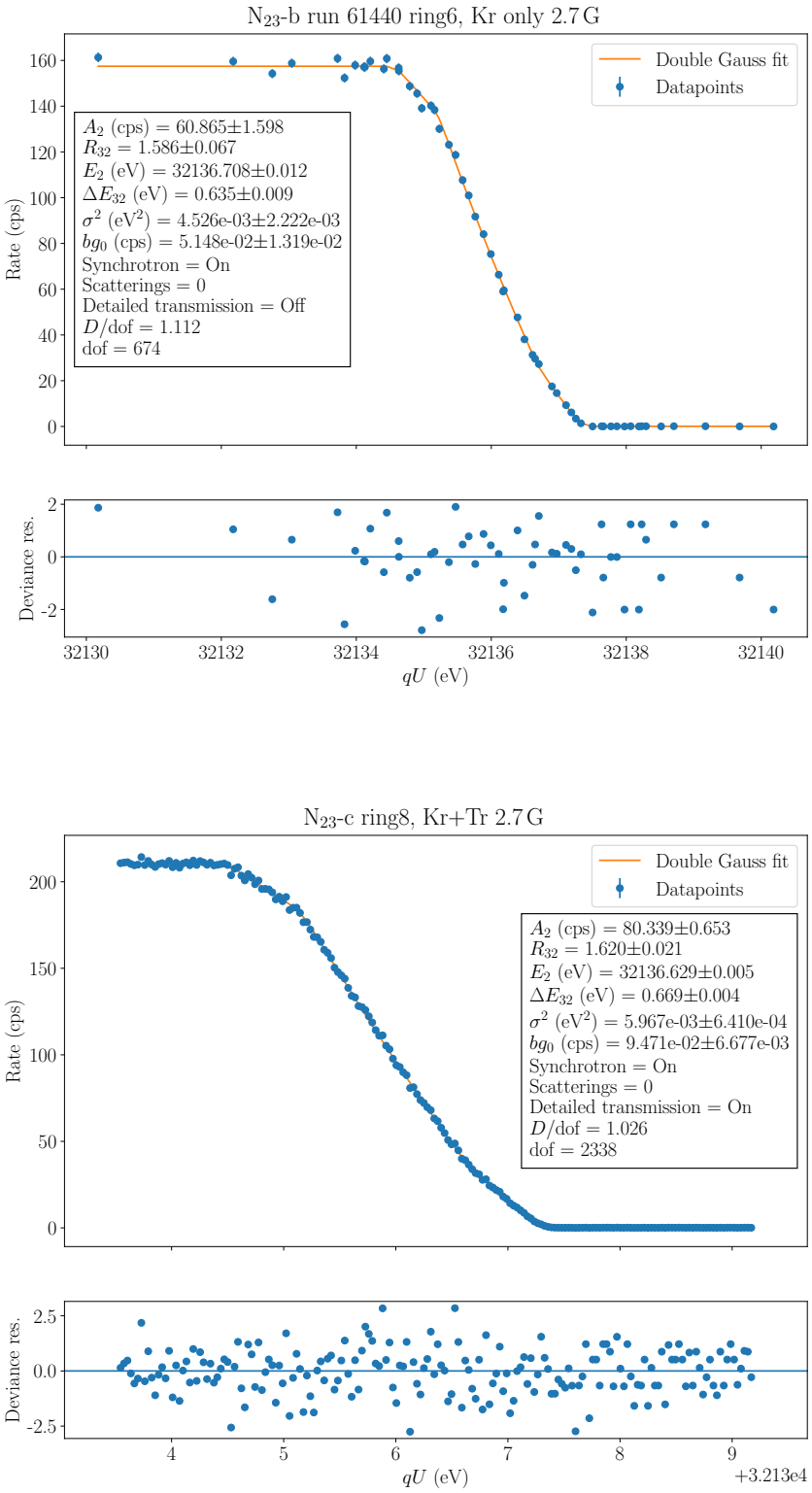

Figure 4.25: Example rings of the ring-combined fits of and N_{23}-b and N_{23}-c. Within each dataset, amplitude ratio and line position difference are common parameters for all rings. The total deviance D and degrees of freedom refer to the total fit of all rings combined.

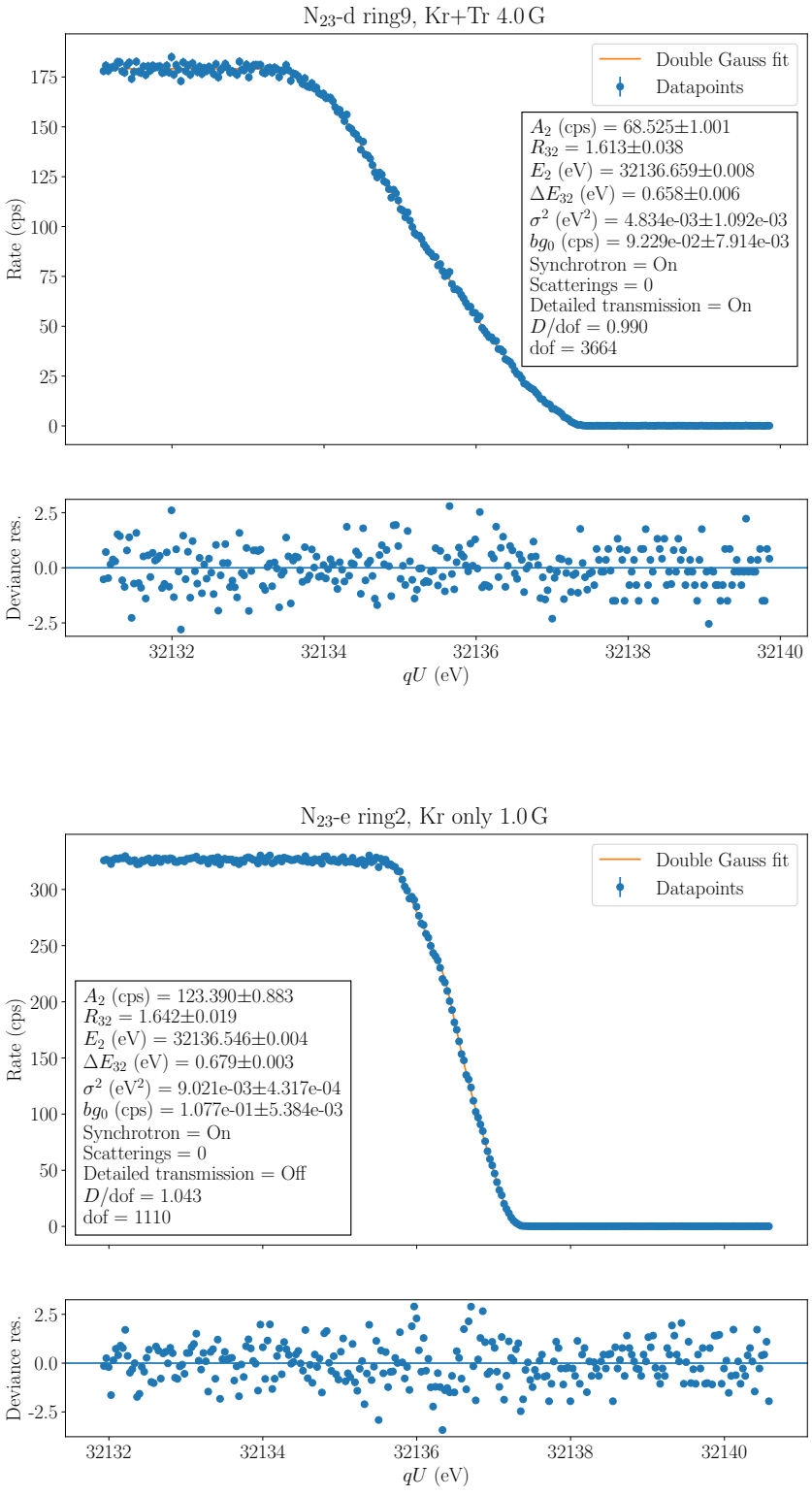

Figure 4.26: Example rings of the ring-combined fits of N_{23}-d and N_{23}-e. Within each dataset, amplitude ratio and line position difference are common parameters for all rings. The total deviance D and degrees of freedom refer to the total fit of all rings combined.

For the Kr+Tr datasets N_{23}-c and N_{23}-d, D/dof lies within the expected statistical distribution width $\sqrt{2/\mathrm{dof}}$ around 1. The residuals overall look natural. In the background region, the residuals look weirdly aligned, but this is just due to the quantisation of counts as integers, which is more significant in the low-count background region. The Kr only datasets N_{23}-a and N_{23}-e have too high deviance. There are also structures in the residuals, pointing to unaccounted systematic effects. A difference to the Kr+Tr condition might be the scattering on gas impurities, as mentioned in section 4.2.3.4. A further discussion of possible unaccounted systematics and future treatment is given in section 4.3.5.

In fig. 4.27 and fig. 4.28, an overview of the fit results of all datasets is given. First, the ramp measurements are discussed, and later the MTD result is compared.

The line position of the Kr only measurements (red) is not strongly ring dependent. There is an increase with radius on the order of 10 meV, consistent with what has been observed for the L_3 line and is probably a result of misalignment (cf. section 4.2.1). This also explains the spike at rings 11 and 12. The Kr+Tr measurements (blue) show a clear drop of line position with radius. This can be accounted to the plasma effects discussed for L_3 in section 4.2.1. The drop however is different for N_{23}-c and N_{23}-d. It is also stronger than what is observed in section 4.2.1 for the 0 V rear wall potential, which is used in this case. This is probably due to a shift of the point of maximum radial homogeneity, as a result of changing work functions of beam tube or rear wall. Such changes might also be responsible for the shifted line position of N_{23}-e. It is 150 meV below the other datasets, which is a quite severe gap, and needs to be cross-checked with other measurements from this time period. The line broadening shows an increase with radius, before dropping at rings 11 and 12. It is overall higher for Kr only than for Kr+Tr, possibly since the plasma might shield longitudinal work function inhomogeneities of the beam tube, which without tritium in the source lead to an increased energy smearing. The broadening values for the two Kr+Tr datasets are in very good agreement for the inner five rings and then start to deviate. For Kr only, the 1 G setting has higher broadening, probably since the flux tube hitting a particular ring maps a larger area in the spectrometer, and thus is more smeared out in energy due to the potential inhomogeneity throughout the analysing plane.

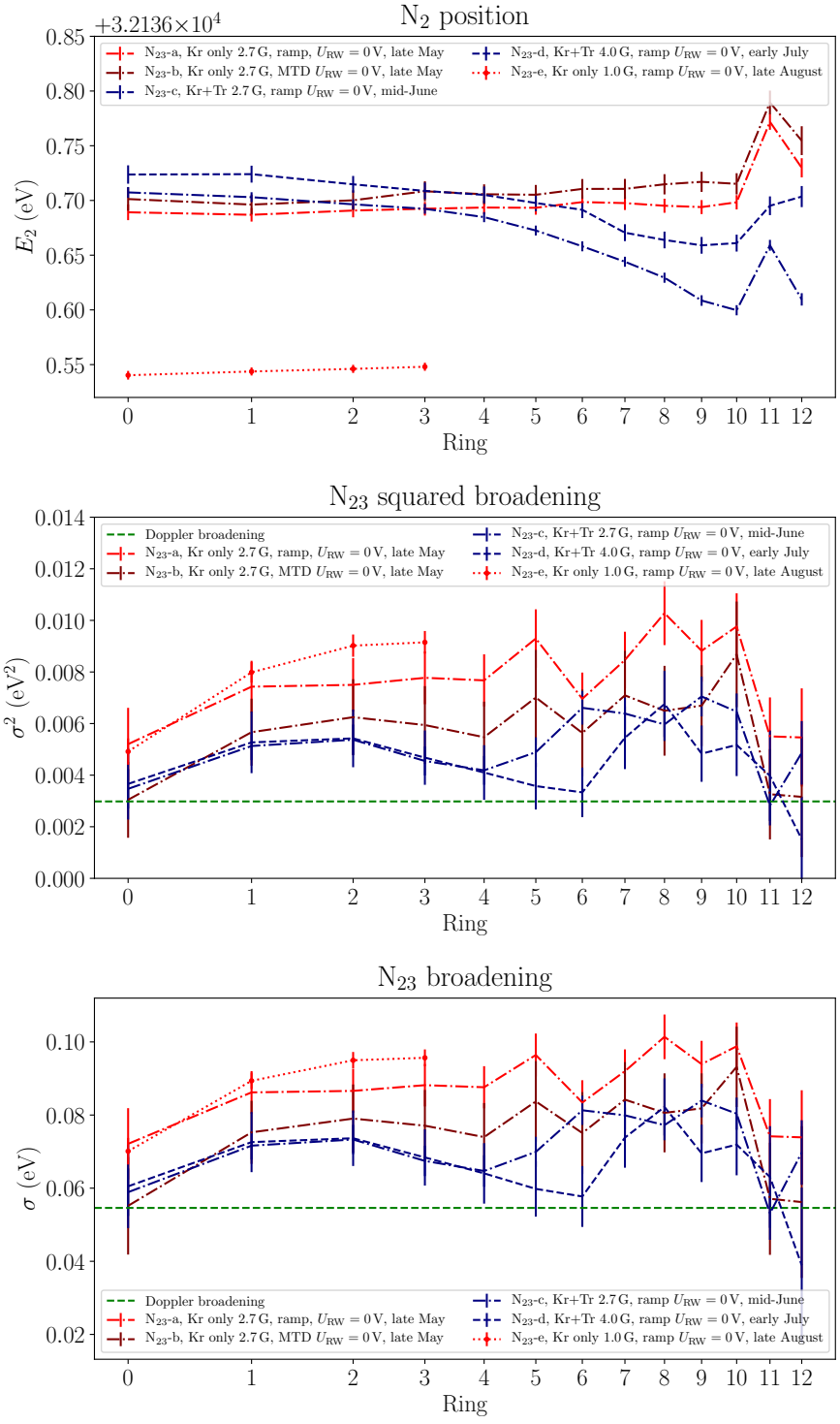

Figure 4.27: Fit result for the analysed N_{23} datasets. The ramping runs were stacked and then fitted. The MTD runs were fitted individually and the results afterwards averaged. In both cases, all rings were fitted with common amplitude ratio and line position difference. For the 1 G measurements, only rings 0 to 3 contain data. From top to bottom: a) N_2 line position, b) squared Gaussian broadening, c) transformed to linear broadening. The green dashed lines mark the expected Doppler broadening.

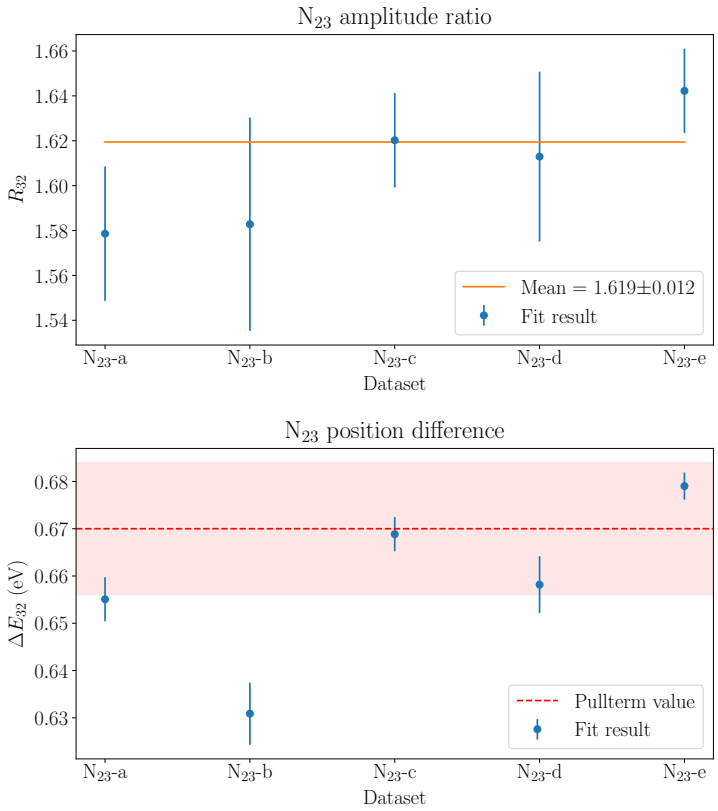

Figure 4.28: Fit result for the analysed N_{23} datasets. The ramping runs were stacked and then fitted. The MTD runs were fitted individually and the results afterwards averaged. In both cases, all rings were fitted with common amplitude ratio and line position difference. From top to bottom: a) Amplitude ratio, fitted with a constant to get mean value, b) line position difference. The red shaded area marks the error band of the pullterm.

The squared broadenings of all datasets have been fitted with constant lines to derive a mean value over all rings. The statistical uncertainties have been increased by $\sqrt{\chi^2/\mathrm{dof}}$ of the constant line fits, to account for the non-constant ring dependence. From the resulting mean values $\langle\sigma^2\rangle$ the Doppler broadening σ_D^2 was subtracted, and the result transformed to a linear broadening

$$\langle\sigma\rangle_{\mathrm{red}} := \sqrt{\langle\sigma^2\rangle - \sigma_D^2} \tag{4.35}$$

that represents the broadening additional to the Doppler smearing. Since the Doppler contribution is different for tritium β electrons, this reduced broadening is the quantity of interest. The resulting values are listed in table 4.12.

Table 4.12: Reduced mean broadenings of the analysed N_{23} datasets. The uncertainties are statistical only and have been increased to account for the ring dependence of the broadening.

	N_{23}-a	N_{23}-b	N_{23}-c	N_{23}-d	N_{23}-e
$\langle\sigma\rangle_{\mathrm{red}}$ (meV)	69.9 ± 2.8	52 ± 4	47.3 ± 3.4	39 ± 4	71 ± 6

The amplitude ratios of all datasets plotted in fig. 4.28 overall agree within uncertainties. The mean value obtained with a constant line fit is (1.619 ± 0.012), which is significantly larger than the literature ratio (1.523 ± 0.029) (table 3.1). The ΔE_{32} of all ramp measurements lie within the pullterm uncertainty, yet do not agree with each other. This indicates that the line position is not well defined by the fits themselves, probably due to unaccounted systematics.

The two runs of the MTD dataset N_{23}-b have D/dof=1.022 and 1.112 for 674 degrees of freedom each. On average, they show 10 meV higher line position than the ramp measurement N_{23}-a with identical settings. Both measurements were done on the same day, which means that temporal drifts are not responsible for the different line positions. Also the broadening is systematically around $0.002\,\mathrm{eV}^2$ smaller. This might be an effect of the changing potential depression in the ramping mode, which could smear the ramping spectrum. The line position difference of the MTD measurement however does not agree at all with the pullterm value. This could indicate numeric instability of the fit that may also distort the other parameters. It is conceivable that the given setpoint distribution might not catch some important features of the spectral shape, while the equidistant binning of the ramping measurement does.

4.3.5 Conclusion and Outlook on N_{23}

Due to their vanishing natural line width, the N_{23} doublet is a preferable tool to investigate energy broadenings. It was shown that the broadening additional to Doppler broadening is on the order of 40-70 meV, while it is overall larger in Kr+Tr mode than in Kr only mode. Yet, there are indications of unaccounted systematics in the N_{23} analysis. The influence of a possibly erroneous analysing plane magnetic field should be taken into account, for instance by fitting it. The line doublet should be measured in a larger scan interval to check for background slopes. The influence of the potential depression in the IE common ramping mode has to be quantified and taken into account. For the MTD mode, a dedicated Monte Carlo study should be undertaken to investigate the effectiveness and possible optimisations of the chosen measurement time distribution.

5 Conclusion and Outlook

While in the Standard Model of particle physics neutrinos are massless, the discovery of neutrino oscillations proves that neutrinos do have mass. Yet, the absolute mass scale remains unknown, while being more than five orders of magnitude below the electron mass. The KATRIN experiment aspires to measure the effective electron antineutrino mass with an unprecedented sensitivity of $0.2\,\mathrm{eV/c^2}$, using a model-independent kinematic approach of measuring the tritium β^- decay spectrum. The KATRIN spectrometer is a MAC-E filter, whose retarding voltage is defined by the spectrometer and source potential. To achieve the sensitivity goal, detailed understanding of systematic effects influencing the potential distribution is mandatory. $^{83\mathrm{m}}$Kr conversion electrons are a nuclear standard, used as a tool to investigate energy shifts and broadenings, for instance related to plasma effects in the windowless gaseous tritium source. For this task, $^{83\mathrm{m}}$Kr can be injected into the source.

In this thesis, measurements of $^{83\mathrm{m}}$Kr conversion electron lines were analysed. It was shown that the radial potential homogeneity in the tritium source, measured by L_3 line position shifts, depends on the difference of rear wall and beam tube potential. Further, it was shown that the sensitivity on energy broadenings using the L_3 line is diminished by its comparably large natural line width. Systematic effects influencing the width have to be understood with high precision to use L_3 for broadening investigations. An important systematic is the energy dependent background slope around L_3. Depending on the analysing plane magnetic field setting, different effects are contributing to the slope. In the 2.7 G setting, non-adiabatic transport of high-energetic electrons produces a positive nonlinear slope. In regards to this, the analysis for this thesis did provide important input in understanding radial dependent line widths observed in earlier measurement campaigns. In higher magnetic field settings, there is a negative slope of smaller magnitude. It is mainly produced by lower krypton lines, while there are indications of additional contributions from other effects. The shape of the slope needs to be understood well, in order to correct the fitted L_3 line width parameter.

The analysis performed for this thesis motivated more study of the N_{23} doublet. Due to their vanishing natural line width, the N_2 and N_3 lines are more sensitive to energy broadenings. Yet, the line intensity is two orders of magnitude lower than for L_3, which makes the measurement and analysis more challenging. A voltage

ramping mode was introduced to reduce dead time during measurement. This may however produce additional systematics that have yet to be investigated. The line broadening in addition to the Doppler broadening was found to be on the order of 40-70 meV, depending on the gas composition and measuring mode. For the future, it is planned to perform more detailed studies and measurements of the N_{23} doublet in various measurement modes, to understand the various systematic effects and establish the N_{23} doublet as the main krypton tool for energy smearing investigations in KATRIN.

References

[Abd+02] J. Abdurashitov et al. "Solar Neutrino Flux Measurements by the Soviet–American Gallium Experiment (SAGE) for Half the 22–year Solar Cycle". In: *Journal of Experimental and Theoretical Physics* 95 (2 2002). DOI: doi:10.1134/1.1506424 (cit. on p. 6).

[Ada+19] D. Adams et al. "Improved Limit on Neutrinoless Double-Beta Decay in ^{1}30Te with CUORE". In: *Physical Review Letters* 124 (2019). DOI: 10.1103/PhysRevLett.124.122501 (cit. on p. 11).

[Ago+18] M. Agostini et al. "Improved Limit on Neutrinoless Double Beta Decay of 76Ge from GERDA Phase II". In: *Physical Review Letters* 120 (2018). DOI: 10.1103/PhysRevLett.120.132503 (cit. on p. 11).

[Ahm+02] Q. Ahmad et al. "Direct Evidence for Neutrino Flavor Transformation from Neutral-current Interactions in the Sudbury Neutrino Observatory". In: *Physical Review Letters* 89.1 (2002). DOI: 10.1103/Phys-RevLett.89.011301 (cit. on p. 7).

[Ake+19] M. Aker et al. "An Improved Upper Limit on the Neutrino Mass from a Direct Kinematic Method by KATRIN". In: *Physical Review Letters* 123 (2019). DOI: 10.1103/PhysRevLett.123.221802 (cit. on pp. 1, 14, 18, 34).

[Alt+05] M. Altmann et al. "Complete Results for Five Years of GNO Solar Neutrino Observations". In: *Physics Letter B* 616 (3 2005). DOI: https://doi.org/10.1016/j.physletb.2005.04.068 (cit. on p. 6).

[Alt+20] K. Altenmüller et al. "High-resolution Spectroscopy of Gaseous ^{83m}Kr Conversion Electrons with the KATRIN Experiment". In: *Journal of Physics G: Nuclear and Particle Physics* 47 (2020). DOI: https://doi.org/10.1088/1361-6471/ab8480 (cit. on pp. 17, 73).

[Ant+19] G. Anton et al. "Search for Neutrinoless Double-Beta Decay with the Complete EXO-200 Dataset". In: *Physical Review Letters* 123 (2019). DOI: 10.1103/PhysRevLett.123.161802 (cit. on p. 11).

[Are+18] M. Arenz et al. “Calibration of High Voltages at the ppm Level by the Difference of ^{83m}Kr Conversion Electron Lines at the KATRIN Experiment”. In: *European Physical Journal C* 78 (2018). DOI: 10.1140/epjc/s10052-018-5832-y (cit. on p. 18).

[Bau13] S. Bauer. “Energy Calibration and Stability Monitoring of the KATRIN Experiment”. PhD thesis. Universität Münster, 2013 (cit. on pp. 28, 29).

[Beh16] J. Behrens. “Design and Commissioning of a Monoenergetic Photoelectron Source and Active Background Reduction by Magnetic Pulse at the KATRIN Experiment”. PhD thesis. Universität Münster, 2016 (cit. on p. 20).

[BL19] J. Behrens and A. Lokhov. *Including Effective Synchrotron Losses into the Transmission Function of KATRIN for the KNM1*. 30 Apr. 2019. URL: https://ikp-katrin-wiki.ikp.kit.edu/katrin/images/0/05/Synchrotron_description.pdf (visited on 15/12/2020) (cit. on p. 37).

[Bok14] K. Bokeloh. “Calibration of Hot and Cold Dark Matter Experiments”. PhD thesis. Universität Münster, 2014 (cit. on p. 21).

[Cha14] J. Chadwick. “Intensitätsverteilung im magnetischen Spektrum der β-Strahlen von Radium B + C”. In: *Verhandlungen der Deutschen Physikalischen Gesellschaft* 16 (1914), pp. 383–391 (cit. on p. 3).

[Cle+98] B. Cleveland et al. “Measurement of the Solar Electron Neutrino Flux with the Homestake Chlorine Detector”. In: *The Astrophysical Journal* 496.1 (1998). DOI: 10.1086/305343 (cit. on p. 6).

[Cow+56] C. Cowan et al. “Detection of the Free Neutrino: A Confirmation”. In: *Science* 124 (3212 1956), pp. 103–104. DOI: 10.1126/science.124.3212.103 (cit. on p. 3).

[Dec+90] D. Decamp et al. “A Precise Determination of the Number of Families With Light Neutrinos and of the Z Boson Partial Widths”. In: *Phys. Lett. B* 235 (1990), pp. 399–411. DOI: 10.1016/0370-2693(90)91984-J (cit. on p. 3).

[Dre+13] G. Drexlin et al. “Current Direct Neutrino Mass Experiments”. In: *Advanced High Energy Physics* 2013 (2013). DOI: https://doi.org/10.1155/2013/293986 (cit. on p. 13).

[Fer34] E. Fermi. “Versuch einer Theorie der β-Strahlen”. In: *Zeitschrift für Physik* 88 (3–4 1934), pp. 161–177. DOI: 10.1007/BF01351864 (cit. on p. 3).

[FS03] Y. Farzan and A. Smirnov. “On the Effective Mass of the Electron Neutrino in Beta Decay”. In: *Physics Letters B* 557 (3–4 2003), pp. 224–232. DOI: https://doi.org/10.1016/S0370-2693(03)00207-7 (cit. on p. 13).

[FT54] V. Faddeeva and N. Terent’ev. “Tables of Values of the Function $w(z) = \exp(-z^2)(1 + 2i/\sqrt{\pi}\int_0^z \exp(t^2)\mathrm{d}t)$ for Complex Argument”. In: *Gosud. Izdat. Teh.-Teor. Lit.* (1954) (cit. on p. 33).

[Fuk+98] Y. Fukuda et al. “Evidence for Oscillation of Atmospheric Neutrinos”. In: *Physical Review Letters* 81.8 (1998). DOI: https://doi.org/10.1103/PhysRevLett.81.1562 (cit. on p. 7).

[Ful] A. Fulst. “A Novel Quasi-Differential Method for MAC-E Filters and Determination and Control of the Electric Potentials of the KATRIN Experiment with a Stabilized Condensed Krypton Source and a UV Illumination System”. PhD thesis. Universität Münster. Unpublished (cit. on pp. 18, 39).

[Fur+17] D. Furse et al. “Kassiopeia: A Modern, Extensible C++ Particle Tracking Package”. In: *New Journal of Physics* 19 (2017). DOI: https://iopscience.iop.org/article/10.1088/1367-2630/aa6950 (cit. on p. 39).

[Gan+16] A. Gando et al. “Search for Majorana Neutrinos near the Inverted Mass Hierarchy Region with KamLAND-Zen”. In: *Physical Review Letters* 117 (8 2016). DOI: 10.1103/PhysRevLett.117.082503 (cit. on p. 11).

[GG61] S. Glashow and M. Gell-Mann. “Gauge Theories of Vector Particles”. In: *Annals of Physics* 15 (3 1961), pp. 437–460. DOI: 10.1016/0003-4916(61)90193-2 (cit. on p. 5).

[GGS58] M. Goldhaber, L. Grodzins and A. Sunyar. "Helicity of Neutrinos". In: *Physical Review* 109 (3 1958), p. 1015. DOI: https://doi.org/10.1103/PhysRev.109.1015 (cit. on p. 6).

[Glü] F. Glück. *Theoretical Inelastic Total Cross Section*. URL: https://ikp-katrin-wiki.ikp.kit.edu/katrin/images/b/b1/CrossSection.pdf (visited on 06/12/2020) (cit. on p. 35).

[Glü20] F. Glück. *Simulation of Krypton M2/M3 Background. Dependence on Pixelrings, Retarding Voltage and AP Magnetic Field*. 7 July 2020. URL: https://ikp-katrin-wiki.ikp.kit.edu/katrin/images/3/33/Kr_Background.pdf (visited on 08/12/2020) (cit. on p. 55).

[Gro15] S. Groh. "Modeling of the Response Function and Measurement of Transmission Properties of the KATRIN Experiment". PhD thesis. Karlsruher Institut für Technologie, 2015 (cit. on pp. 20, 38).

[Gro20] KATRIN Eloss Group. *KATRIN T_2 Eloss Model*. 17 Mar. 2020. URL: https://ikp-katrin-wiki.ikp.kit.edu/katrin/images/b/b8/Eloss_2020_03_17.pdf (visited on 10/12/2020) (cit. on p. 34).

[Ham+99] W. Hampel et al. "GALLEX Solar Neutrino Observations: Results for GALLEX IV". In: *Physics Letters B* 447 (1 1999). DOI: http://dx.doi.org/10.1016/S0370-2693(98)01579-2. (cit. on p. 6).

[Har15] F. Harms. "Characterization and Minimization of Background Processes in the KATRIN Main Spectrometer". PhD thesis. Karlsruher Institut für Technologie, 2015 (cit. on p. 17).

[Hig64] P. Higgs. "Broken Symmetries and the Masses of Gauge Bosons". In: *Physical Review Letters* 13 (16 1964). DOI: https://doi.org/10.1103/PhysRevLett.13.508 (cit. on p. 10).

[Hir+91] K. Hirata et al. "Real-time, Directional Measurement of ^{8}B Solar Neutrinos in the Kamiokande II Detector". In: *Physical Review D* 44 (8 1991), pp. 2241–2260. DOI: https://doi.org/10.1103/PhysRevD.44.2241 (cit. on p. 6).

[Hol17] J. Holdsworth. *Wikipedia - Beta Decay*. 2017. URL: https://commons.wikimedia.org/wiki/File:Beta_Negative_Decay.svg (visited on 08/11/2020) (cit. on p. 12).

[Jac99] J. Jackson. *Classical Electrodynamics*. 1999 (cit. on p. 22).

[KATa] KATRIN-Collaboration. "KATRIN design report". In: (). DOI: 10.5445/IR/270060419 (cit. on pp. 9, 10, 13, 15, 18, 20).

[KATb] KATRIN-Collaboration. *KATRIN Official Website*. URL: http://www.katrin.kit.edu/ (visited on 07/05/2020) (cit. on p. 19).

[Kle+19] M. Kleesiek et al. "β-decay Spectrum, Response Function and Statistical Model for Neutrino Mass Measurements with the KATRIN Experiment". In: *European Physical Journal C* 79.3 (2019). DOI: 10.1140/epjc/s10052-019-6686-7 (cit. on pp. 24, 27, 33–35, 37, 38).

[Kle14] M. Kleesiek. "A Data-Analysis and Sensitivity-Optimization Framework for the KATRIN Experiment". PhD thesis. Karlsruher Institut für Technologie, 2014 (cit. on pp. 14, 25).

[Kra+05] C. Kraus et al. "Final Results from Phase II of the Mainz Neutrino Mass Search in Tritium β Decay". In: *European Physics Journal C* 40 (2005). DOI: https://doi.org/10.1140/epjc/s2005-02139-7 (cit. on p. 1).

[Kra+12] C. Kraus et al. "Measurement of the Electron Antineutrino Nass in Tritium Beta Decay in the Troitsk Nu-mass Experiment". In: *Physics of Atomic Nuclei* 75 (2012). DOI: https://doi.org/10.1134/S1063778812030027 (cit. on p. 1).

[Kuc16] L. Kuckert. "The Windowless Gaseous Tritium Source of the KATRIN Experiment. Characterisation of Gas Dynamical and Plasma Properties". PhD thesis. Karlsruher Institut für Technologie, 2016 (cit. on pp. 8, 14, 15, 25, 26, 47).

[LL02] T. Loredo and D. Lamb. "Bayesian Analysis of Neutrinos Observed from Supernova SN 1987A". In: *Physical Review D* 65 (6 2002). DOI: https://doi.org/10.1103/PhysRevD.65.063002 (cit. on p. 11).

[Mac] M. Machatschek. "Evaluation and Systematic Analysis of the Neutrino Mass Measurements of the KATRIN Experiment". PhD thesis. Karlsruher Institut für Technologie. Unpublished (cit. on pp. 27, 35).

[Mac16] M. Machatschek. "Simulation of the ^{83m}Kr Mode of the Tritium Source of the KATRIN Experiment". Master thesis. Karlsruher Institut für Technologie, 2016 (cit. on p. 30).

[Mis20] MissMJ. *Wikipedia - Standard Model of Elementary Particles*. 2020. URL: https://en.wikipedia.org/wiki/File:Standard_Model_of_Elementary_Particles.svg (visited on 08/11/2020) (cit. on p. 4).

[MS86] S. Mikheyev and A. Smirnov. "Resonant Amplification of ν Oscillations in Matter and Solar-neutrino Spectroscopy". In: *Il Nuovo Cimento C* 9.1 (1986). DOI: doi:10.1007/BF02508049 (cit. on p. 9).

[Ost20] R. Ostertag. "Investigation of Plasma Effects in the KATRIN Source with ^{83m}Kr". Master thesis. Karlsruher Institut für Technologie, 2020 (cit. on p. 47).

[Pau30] W. Pauli. "Letter to Gauvereinstagung in Tübingen: Sehr geehrte radioaktive Damen und Herren". In: *R. Kronig and V. Weisskopf (Eds.) Wolfgang Pauli, Collected Scientivic Papers* 2 (1930) (cit. on p. 3).

[Pon68] B. Pontecorvo. "Neutrino Experiments and the Question of Leptonic–Charge Conservation". In: *Sov. Phys. JETP* 26 (1968), pp. 984–988 (cit. on p. 6).

[QV15] X. Qian and P. Vogel. "Neutrino Mass Hierarchy". In: *Progress in Particle and Nuclear Physics* 83.1–30 (2015). DOI: 10.1016/j.ppnp.2015.05.002 (cit. on p. 8).

[Res19] O. Rest. "Precision High Voltage at the KATRIN Experiment and New Methods for an Absolute Calibration at ppm-Level for High-Voltage Dividers". PhD thesis. Universität Münster, 2019 (cit. on pp. 18, 20).

[Rod20] C. Rodenbeck. *Energy Loss at Impurities in the Krypton mode*. 1 Sept. 2020. URL: https://ikp-katrin-wiki.ikp.kit.edu/katrin/images/0/03/2020-09-01_ElossAtImpurities.pdf (visited on 08/12/2020) (cit. on p. 68).

[Sac20] R. Sack. "Measurement of the Energy Loss of 18.6 keV Electrons on Deuterium Gas and Determination of the Tritium Q-value at the KATRIN Experiment". PhD thesis. Universität Münster, 2020 (cit. on p. 34).

[SW64] A. Salam and J. C. Ward. "Electromagnetic and Weak Interactions". In: *Physics Letters* 13 (2 1964), pp. 168–171. DOI: 10.1016/0031-9163(64)90711-5 (cit. on p. 5).

[Vén+18] D. Vénos et al. "Properties of ^{83m}Kr Conversion Electrons and their Use in the KATRIN Experiment". In: *Journal of Instrumentation* 13 (2018). DOI: https://doi.org/10.1088%2F1748-0221%2F13%2F02%2Ft02012 (cit. on pp. 29, 30, 57, 69).

[Wei67] S. Weinberg. "A Model of Leptons". In: *Physical Review Letters* 19 (21 1967), p. 1264. DOI: https://doi.org/10.1103/PhysRevLett.19.1264 (cit. on p. 5).

[Wol78] L. Wolfenstein. "Neutrino Oscillations in Matter". In: *Physical Review D* 17.9 (1978). DOI: https://doi.org/10.1103/PhysRevD.17.2369 (cit. on p. 9).

[Wu+57] C. Wu et al. "Experimental Test of Parity Conservation in Beta Decay". In: *Physical Review* 105 (4 1957), pp. 1413–1415. DOI: https://doi.org/10.1103/PhysRev.105.1413 (cit. on p. 6).

[Zub12] K. Zuber. *Neutrino Physics*. 2nd ed. CRC press, 2012 (cit. on p. 8).

[Zyl+20] P. Zyla et al. "Review of Particle Physics". In: *Progress of Theoretical and Experimental Physics* 2020 (8 2020). DOI: https://doi.org/10.1093/ptep/ptaa104 (cit. on pp. 8, 10).

Declaration of Academic Integrity

Hereby, I confirm that this thesis on *Analysis of Krypton Conversion Electron Lines of the Gaseous Krypton-Tritium Source of KATRIN* is solely my own work and that I have used no sources or aids other than the ones stated. All passages in my thesis for which other sources, including electronic media, have been used, be it direct quotes or content references, have been acknowledged as such and the sources cited.

Münster, December 16, 2020 _____

Matthias Böttcher

I agree to have my thesis checked in order to rule out potential similarities with other works and to have my thesis stored in a database for this purpose.

Münster, December 16, 2020 _____

Matthias Böttcher